Sonocytology: Dynamic acoustic manipulation of particles and cells

Georgios D. Skotis

A THESIS SUBMITTED TO

THE DEPARTMENT OF ELECTRONICS AND ELECTRICAL ENGINEERING

SCHOOL OF ENGINEERING

UNIVERSITY OF GLASGOW

IN FULFILMENT OF THE REQUIREMENTS

FOR THE DEGREE OF

DOCTOR OF PHILOSOPHY

February 2018

Abstract

Separating and sorting cells and micro-organisms from a heterogeneous mixture is a fundamental step in biological, chemical and clinical studies, enabling regenerative medicine, stem cell research, clinical sample preparation and improved food safety. Particle and cell manipulation by ultrasound acoustic waves provides the capability of separation of cells on the basis of their size and physical properties. Offering the advantages of relatively large microfluidic volumes in a label-free, contactless and biocompatible manner. Consequently, the discovery of alternative methods for precise manipulation of cells and particles is of highly demand.

This thesis describes a novel approach of ultrasound acoustic manipulation of particles and cells. The principle of operation of the dynamic acoustic field method is described accompanied with acoustic separation simulations. Furthermore, the complete fabrication and characterisation of two types of ultrasound devices is given. The first one is a bulk acoustic wave (BAW) device and the second is a surface acoustic wave (SAW) device.

Successful experiments using the BAW device for sorting different diameter particles with a range from 5 to 45 μm are demonstrated, also experiments for sorting particles depending on their density are presented. Moreover, experiments of the proposed method for sorting porcine dorcal root ganglion (DRG) cells from a heterogeneous mixture of myelin debris depending on their size are displayed. Experimental results of sorting cells depending on their stiffness are demonstrated. Experiments using the fabricated SAW device for sorting different diameter particles in a constant flow with a range from 1 μm to 10 μm are presented. Furthermore, experiments of the proposed method for sorting live from dead Htert cells depending on their mechanical properties, i.e. stiffness are displayed.

As a side project a new idea for dynamic acoustic manipulation by rotating the acoustic field is demonstrated. The basic principles of this method and the simulations for verifying this concept are displayed. Experiments for sorting 10 μm from 3 μm polystyrene particles are presented, with two different types of the dynamic acoustic rotating field being examined.

Acknowledgements

First of all, I would like to thank my wife Eliza and my newly born daughter Melina, for supporting me through all these years and never stopped believing in me. Without them nothing would have been possible.

I would like to heartily thank my supervisor Professor David Cumming for providing the necessary and so important guidance and support that every PhD student needs from his supervisor. He always inspired the confidence that was needed in order to overcome the various issues surfacing during this work.

I would also like to thank my second supervisor Dr. Mathis Riehle for welcoming me in the Centre for Cell Engineering, Institute for Molecular, Cell and Systems Biology. I Also thank him for providing training on cell culturing and the necessary equipment for handling cells. And also thank him for his mentoring in several occasions during this PhD.

I would like to express my gratitude to Professor Manuel Salmeron-Sanchez for letting me use the AFM microscope for the stiffness measurements and also Dr. Marco Cantini for the training and help on handling the equipment.

Special thanks to Dr. Julien Reboud who shared with me his tremendous knowledge in microfluidics. I would still have been bonding micro-channels without his help.

I would like to thank all the individuals that compose the MST group, and mostly I would like to thank James Grant, who became a good friend over the years for sharing his knowledge and providing his help in the nanofabrication centre of JWNC, also wire bonding the devices when needed and his willingness to proof read part of this thesis. Also, I would like to thank Boon Chong Cheah, Chunxiao Hu and Ivonne Escorcia Carranza for reviewing this thesis and also for being good friends.

I would like to thank Fiona Grant and Calum Sinclair from the Physics department for dicing the $LiNbO_3$ wafers.

I would like to thank my friend and colleague Christos Giagkoulovits for the breaks, the constructive conversations through all these years and for showing continuous genuine interest, who helped me with his unique way of doing things.

Special thanks to my good friend Charalampos Klitis who helped me in every aspect of my life all of these years, from cleanroom tips to coffee breaks, being there giving his support waiting nothing in return.

I would like to thank Chara Sartzi and all my friends in Glasgow, for their support and the provided courage to overcome any difficulties and also a beer or two when it was needed.

I would like to thank Vassilis Papageorgiou for sharing the know-how of Glasgow's whereabouts.

I would also like to thank Sankar Peralagu, Mohammed Al-Rawhani and Srinivas Velugota for helping me with the one or the other way.

I would also like to thank all my friend who are scattered all over the UK and also those left in Greece who are too many to name, for their moral support all these years.

Last but not least, a big thank you to my parents Isidoros and Lamprini who always have been there to help and support their child while growing.

Associated Publications

Journal Papers

G.D. Skotis, D.R.S. Cumming, J.N. Roberts, M.O. Riehle and A.L. Bernassau, “Dynamic acoustic field activated cell separation”, Lab on a Chip, vol. 15, pp. 802-810, 2015.

M.A.B. Andrade, G.D. Skotis, S. Ritchie, D.R.S. Cumming, J.N. Roberts, M.O. Riehle and A.L. Bernassau, “Contactless Acoustic Manipulation and Sorting of Particles by Dynamic Acoustic Fields”, IEEE T-UFFC, special issue, vol. 63, no. 10, pp. 1593-1600, 2016.

International Conference Publications

G.D. Skotis, D.R.S. Cumming, J.N. Roberts, M.O. Riehle and A.L. Bernassau, “Acoustic Tweezing for Patterning and Discriminating Particles”, IEEE PRIME, 29-June – 2July 2015, Glasgow, Scotland, UK.

G.D. Skotis, M.A.B. Andrade, S. Ritchie, D.R.S. Cumming, J.N. Roberts, M.O. Riehle and A.L. Bernassau, “Dynamic Acoustic Field for Tuneable and Scalable Particle Sorting”, IEEE International Ultrasonics Symposium, Taipei, Taiwan, 21-24 Oct 2015, pp.1-4.

Oral Presentations

G.D. Skotis, D.R.S. Cumming, J.N. Roberts, M.O. Riehle and A.L. Bernassau, “Dynamic acoustic field activated cell separation for Regenerative Medicine”, International Congress on Ultrasonics (ICU), 10-14 May 2015, Metz, France.

Other

D.R.S. Cumming, M. Al-Rawhani, A.L. Bernassau, I. Escorsia, F. Gesellchen, J.P. Grant, C. Martin, M.O. Riehle, P. Shields & G. D. Skotis, “Hybridising photonic and biotechnologies to CMOS”, 6th IEEE International Workshop on Advances in Sensors and Interfaces (IWASI), Gallipoli, Turkey, 18-19 June 2015, pp. 15-16.

Contents

List of Figures

List of tables

Abbreviations

1D	One dimensional
2D	Two dimensional
3D	Three dimensional
AFM	Atomic Force Microscopy
BSA	Bovine serum albumin
CAD	Computer aided design
CCE	Centre of Cell Engineering
NaCl	Sodium Chloride
DAF	Dynamic acoustic field
DARF	Dynamic Acoustic Rotating Field
DEP	Dielectrophoresis
DI	Deionised
FACS	Fluorescence activated cell sorting
FFA	Free flow acoustophoresis
fps	Frames per second
IDT	Intedigitated transducer
JWNC	James Watt Nanofabrication Centre
$LiNbO_3$	Lithium Niobate
PCB	Printed circuit board

PDMS	Polydimethylsiloxane
PMMA	polymethyl methacrylate
PVC	Polymerizing vinyl chloride
PVDF	Polyvinylidene fluoride
PZT	Lead zirconate titanate
Re	Reynolds number
RO	Reverse osmosis
SAW	Surface acoustic wave
SSAW	Standing surface acoustic wave
SMA	SubMiniature version A
SFIT	Slanted-finger interdigitated tranducer
TDX	Transducer
UV	Ultraviolet

1. Introduction

1.1 Motivation of technology

Particle manipulation has been a topic of interest among researchers for the past few decades because it can be beneficial to many applications that require a contactless handling technique. Precise control of particles, molecules and biological cells has become of major importance in life sciences and medicine, with applications in tissue engineering, biochemical analysis and cell separation and sorting.

New techniques have been developed for throughput cell manipulation that are capable of trapping and transporting biological cells in liquid using acoustic forces in an ultrasound field [1]. Researchers have developed a variety of patterning and sorting techniques for microparticles such as micro-contact printing [2], optical tweezing [3], optoelectronic tweezing [4], magnetic tweezing [5], dielectrophoresis [6], evanescent waves/plasmonics [7], hydrodynamic flows [8] and ultrasonic manipulation [9], including bulk acoustic wave-based acoustophoresis [10]. These significant advances of contactless means of manipulations of particles and cells, have driven the scientific society to explore further capabilities of the aforementioned techniques.

Furthermore, the ultrasound acoustic manipulation technique is advantageous in many aspects, such as the low cost, non-invasive technique allowing cell viability, easy integration of microfluidic systems and generation of appropriate forces to handle cells of size of less than 10 μm. These advantages are essential in numerous biological studies and clinical applications, such as molecular biology, pathology, immunology, genetics, and medical diagnostics and therapeutics [11]. Among the numerous biological applications a lot of interest has been shown in cell filtering [12] and concentration [13], cell separation and sorting [14], [15], [16], [17], [18], cell washing and mixing in a continuous manner [19], [20], cell patterning [21] and immobilisation [22], enhancement of the sensitivity of bioassays [23], [24], culturing and proliferation of cells in suspension [25] and increasing throughput in continuous flow acoustophoresis [26].

Due to the on-going growth of the technology in terms of applications, the miniaturization and automation of cell-based applications in biotechnology is of high importance and is dependent on the development of flexible tools for non-intrusive manipulation of bio-particles. Thus new

approaches and techniques are under investigation, in order to achieve high-throughput dynamic manipulation.

1.2 Aim and objectives

Ultrasound devices for particle manipulation that already exist have demonstrated valuable capabilities. However, drawbacks include the lack of repeatability, in some cases lack of dynamic control of the acoustic landscape, unstable generated forces that can lead to differences in the movement of particles of the same properties. Furthermore, some methods allow only small particle displacement and some other lack of flexibility due to the dimensional limitations of the transducers.

These disadvantages and limitations drove the aims and objectives of the work presented in this thesis, with the aims being recited as follows:

Firstly, the aim of this research is to achieve particle sorting using a BAW device in the preliminary work [27] by utilising a novel approach where two opposing transducers form standing waves. Continuously changing the phase of one of the opposing transducers with respect to the other results in the translation of the nodes and antinodes, thus allowing particles and cells to move with this translation of the nodes. The advantages of this technique is the high degree of separation selectivity, very stable generated forces allowing better spatial separation of particles and cells, with the objective of increasing the selectivity of the device, thus achieving separation of sub populations of high purity but also high efficiency.

Secondly, the objective to verify the repeatability of the method and to define the best region of operation of the technique and the limits of the device was completed by fabricating a device with the same properties and by repeating a vast number of experiments already taken with the device from the preliminary work.

One more aim was to prove the capability of particle separation of different populations depending on their size but also the capability of particle separation regarding their density, by the same device using the dynamic acoustic field method. Furthermore, the aim of proving the capability of the proposed method to translate to real life applications for sorting cells depending on their size or stiffness.

The last objective of this thesis was to fabricate a new SAW device aiming to achieve a high throughput sorter utilising the aforementioned proposed method.

1.3 Thesis outline

This thesis is divided into seven chapters and a brief description of each chapter is provided as follows.

Chapter 2 displays a review of the literature of particle and cell manipulation technologies, giving an overview of the working principles and applications. A more in depth analysis of acoustophoretic techniques is given, for bulk acoustic wave devices, surface acoustic wave devices and implementation of microfluidic channels for biological applications.

Chapter 3 demonstrates the fundamental theory of ultrasound, ultrasonic transducers, materials with piezoelectric properties and ultrasound standing waves. The ultrasound acoustic radiation forces are being exploited along with the effect of the acoustic streaming. Surface acoustic wave theory is displayed in conjunction with the wave propagation on the substrate and the liquid medium of the particle transmission for such a device.

Chapter 4 describes the principle of operation of the proposed method of this work for dynamic acoustic manipulation of particles and cells. Acoustic separation simulations are displayed along with control mechanisms including Labview. Furthermore, the complete fabrication and characterisation of two types of ultrasound device are given. The first one is a bulk acoustic wave device and the second a surface acoustic wave device.

Chapter 5 displays the experimental setup used in this work for using the BAW device. Experiments for sorting different diameter particles with a range from 5 to 45 μm are given, but also experiments for sorting particles depending on their density are presented. Moreover, experiments of the proposed method are displayed for sorting porcine DRG cells from a heterogeneous mixture of myelin debris depending on their size and also sorting cells by their mechanical properties, i.e. stiffness. A summary of this work is included.

Chapter 6 presents the experimental setup used in this work for using the SAW device. Experiments for sorting different diameter particles in a constant flow with a range from 1 to 10 μm are presented. Furthermore, experiments showing the translation to real life applications

of the proposed method are displayed for sorting live from dead cells depending on their mechanical properties, i.e. stiffness. A summary of this work is included.

Chapter 7 describes a new idea for dynamic acoustic manipulation by rotating the acoustic field, which was implemented in parallel as part of this thesis. The basic concept of this method is displayed, while the simulations for verifying this concept are demonstrated. Experiments for sorting different diameter polystyrene particles of 3 to 10 μm are presented. Two different types of the dynamic acoustic rotating field are being investigated. A summary of this work is included.

Chapter 8 summarises the conclusions of this research work and discusses potential future work.

2. Background - Literature review

2.1 Introduction

Over the years, advances have been made for manipulating particles by using different techniques either by contact (invasive) or contactless (non-invasive) means. Due to the preference over non-invasive methods, several contactless manipulation techniques have been developed. The more promising ones presented in the literature are the hydrodynamic methods, magnetic tweezers, optical tweezers, dielectrophoresis and acoustic tweezers or acoustophoresis.

In the hydrodynamic field a particle is subjected to hydrodynamic forces which are dependent on the velocity of the fluid with respect to the particle. Hydrodynamic methods have been widely used in the field of cell biology and analytical chemistry in order to focus particles in a fluid stream for applications such as cell counting, sorting in flow cytometers and fluorescence activated cell sorters. An example of the hydrodynamic method is shown in Figure 2.1. The main method used in flow cytometry is hydrodynamic focusing due to its ability to drive high volumes of particles and cells at high speed flow rates with high throughput [28]. One disadvantage of this method is that shear stress can be generated from the fluid flow and it may cause separation of the cell's membrane resulting in cytolysis. Thus, a control of the flow velocity is required in order to protect the cells from shearing apart.

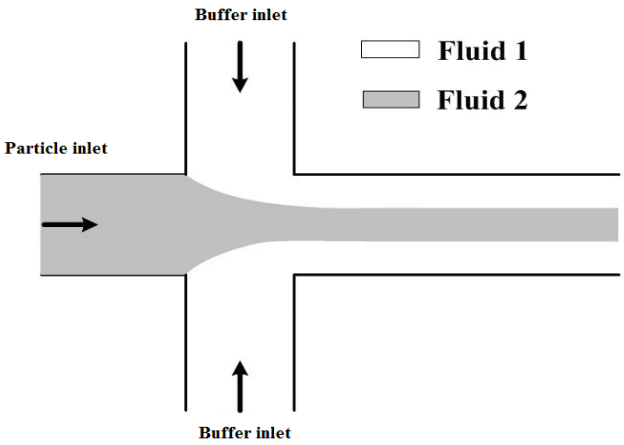

Figure 2.1 Hydrodynamic method for focusing particles in a channel. Image reproduced from [34].

Trapping particles and cells in the hydrodynamic field can be achieved by creating side channels in a main fluidic channel. Particles and cells are trapped by pressure forces following the fluid flow introduced by the side channels [29]. Furthermore, the trapped particles and cells can be easily released by reversing the flow direction of the side channels. Thus, different types of cells can be individually manipulated by the same trapping system [30].

Magnetic tweezing is described by the utilisation of the magnetic field to apply forces on magnetic particles, while the visible component of the particle allows the imaging of the travelled distance [31]. If there was only a homogeneous magnetic field, there would be no acting force on the particle, hence the particles would only be magnetised and would not move. Thus, in order to generate a magnetic force, a heterogeneous magnetic field is necessary to create an acting force in the order of pico-Newton (pN) on a micron sized particle. Due to the need of the particles to be magnetised, real life applications are limited to red blood cells and magnetotactic bacteria because of their readily available magnetic characteristics [32]. Consequently, the non-magnetic cells need to be labelled by using nano-particles [33] or using paramagnetic lanthanide ions. Therefore, magnetic tweezers are commonly used for cell positioning and patterning or for sorting non-biological micro-objects.

The phenomenon of dielectrophoresis (DEP) is described as the forces are exerted on a dielectric particle generated by a non-uniformed electric field, causing the particle to move away or towards the high electric region of the electric field [34], if the particle moves towards the direction of increasing electric field, the phenomenon is known as positive DEP (p-DEP), but if the particle moves away from high field regions, it is known as negative DEP (n-DEP), as shown in Figure 2.2. In DEP precharged particles are not required in order to generate forces. The direction of dielectrophoretic force depends on the Clausius–Mossotti factor, which is determined by the permittivity of the particle and the surrounding medium [35].

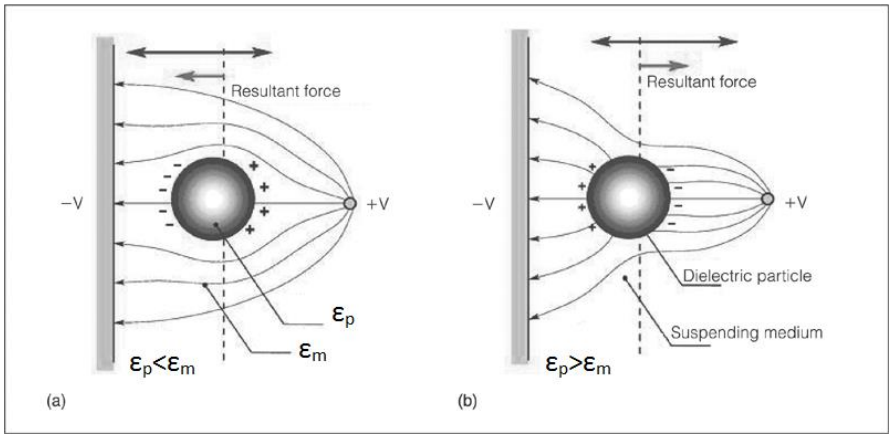

Figure 2.2 Particle under (a) p-DEP (b) n-DEP, image reproduced from [42].

This force amplitude depends on the frequency of the electric field, the mechanical properties of the particles such as shape and size [36] and the electrical properties of the medium and the particles. Manipulation of particles with great selectivity can be achieved by an electric field with a specific frequency, giving the opportunity for DEP to be used in a range of industrial, life sciences and biomedical applications. Some of these applications are micro polishing [37], mineral separation [38], dispensing of nano-droplets [39], cell sorting [40] and characterisation of biological particles [41].

Optical tweezing is a field that relies on a higher gradient of electric field, which is generated near the waist of a highly focused laser beam. This is done in order to create enough force to manipulate dielectric particles in the order of nanometres and micrometres. The transfer of momentum obtained from the scattering of incident photons applies forces on the dielectric particles. This force can be divided into two optical types of forces: the scattering force, which pushes particles along the direction of the light propagation, and the gradient force, which pulls particles towards the direction of the spatial light intensity gradient. In general, the scattering forces are dominant, but a steep intensity gradient force must be also be taken into account. When a particle is located away from the centre of the beam, a larger force is generated by the momentum transferred from the higher intensity rays closer to the centre, so that the net force points towards the beam centre as shown in Figure 2.3 (left side). If the particle has moved to the centre of the beam, even though the resultant lateral force is zero, the resultant axial force dominates the net force, still pointing away from the laser source as shown in Figure 2.3 (right side). Thus, a focused laser beam can be used to fix the axial position of the particle. That change of momentum of the focused laser beam creates a force towards the beam waist, which causes the particle to be trapped slightly behind the beam waist, where the net force

compensates for the scattering force. Normally, the range of the laser's power is in the order of milliwatts (mW) to 1 W, this translates to forces in the range of femtoNewtons (fN) up to hundreds of picoNewtons (pN).

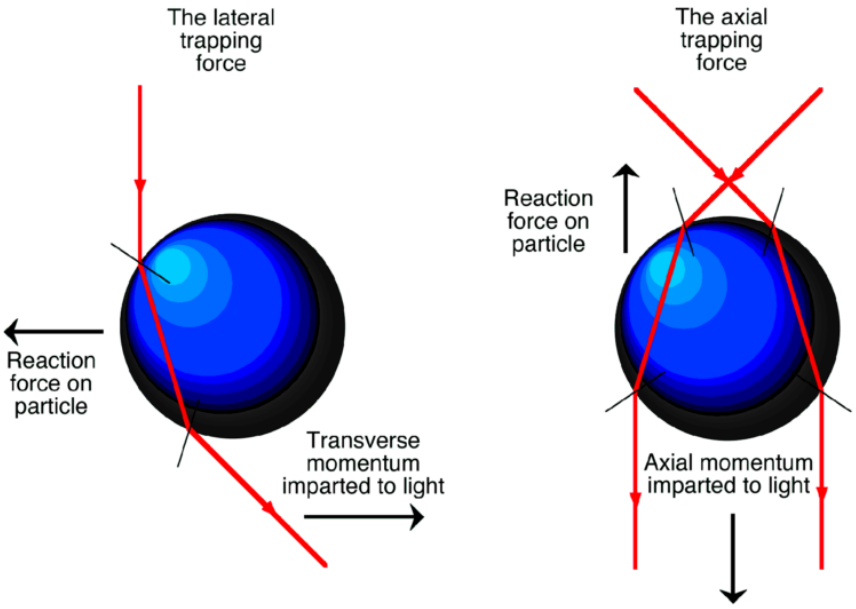

Figure 2.3 The optical ray origin of the lateral (left) and axial (right) trapping force within optical tweezers, image reproduced from [49].

The first demonstration of the acceleration and trapping of micron-sized dielectric spheres was done by Arthur Ashkin. It was demonstrated with both liquid and gas by forming optical potential wells using a continuous wave argon laser [42]. Later on he demonstrated a stable optical method for trapping micron-sized dielectric objects by utilising a single-beam gradient force optical trap [43], hence it has also been known as optical tweezers. Due to its capability for precise manipulation of nanometre- and micron-sized objects without labelling, optical tweezers became a major research field in biology, biochemistry, biophysics and physical chemistry. In the past two decades, attention has been attracted to develop three-dimensional optical field geometries for applications such as particle sorting [44] and nano-fabrication [45], measuring the mechanical properties of biological molecules [46] and to study physical mechanisms within molecules, such as DNA [47]. In most recent years scientists have combined the cell manipulation capabilities of optical tweezers with other biological techniques, such as cell lysis and electroporation [48] in order to achieve better manipulation results.

2.2 Acoustic tweezers

In acoustic tweezers, a force is obtained in a similar way to the optical radiation force as explained for optical tweezers. An acoustic radiation force acting on a particle is generated by a gradient in the energy density due to propagating acoustic waves that can either deflect or attract the particle of interest depending on its mechanical properties. Therefore, particles suspended in either travelling or standing acoustic wavefields experience non-zero time averaged radiation forces. When a reflected travelling wave encounters the transmitted travelling wave coming from the opposite direction or when two transmitted travelling waves coming from opposite directions, then standing waves are formed, causing particles to move to the pressure nodes or to the pressure antinodes, inside the acoustic field under the effect of the acoustic radiation forces, depending on the physical properties of the particles such as the density and the compressibility. Those properties determine the contrast factor (φ), if the contrast factor of the particles is positive then they agglomerate at the nodes and if the contrast factor is negative then the particles agglomerate at the antinodes. An example of particles with positive contrast factor agglomerating at the pressure nodes is given in Figure 2.4.

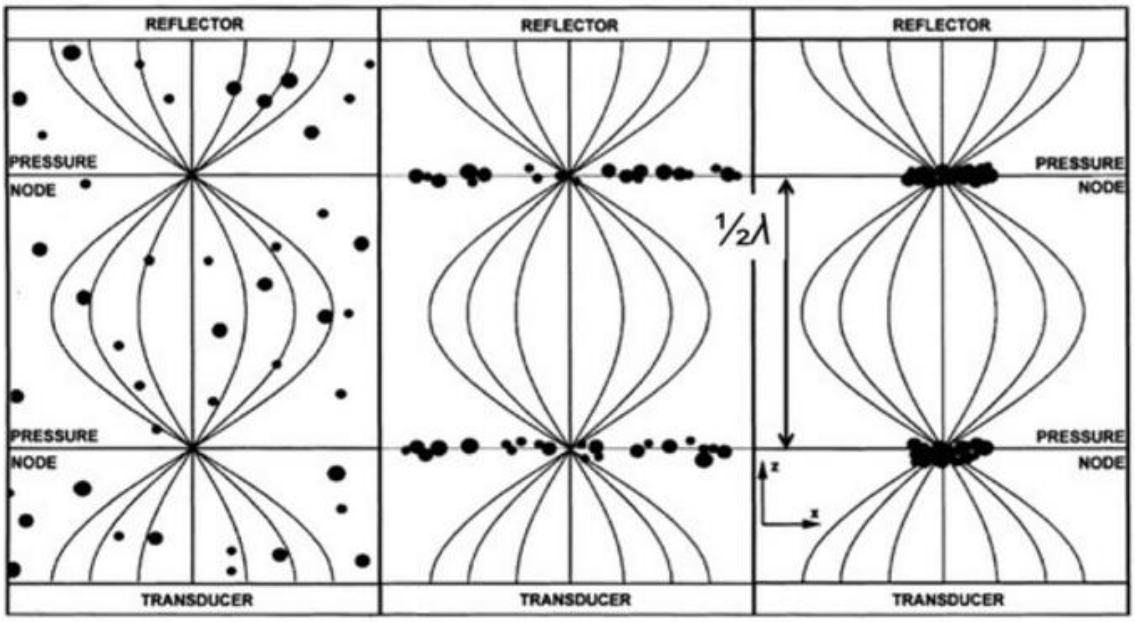

Figure 2.4 Particles agglomerate at the nodes of acoustic standing waves generated from a transducer and a reflector, image reproduced from [57].

Early observations of acoustic radiation forces were made by August Kundt. He presented a method for measuring the speed of sound in gases. The method consisted of using a standing

acoustic wave to move a small amount of fine powder to the pressure nodal planes of the acoustic field in a resonant structure inside a transparent horizontal tube. This equipment was called Kundt's tube and enabled measurement of the wavelength as twice the distance between two nodal planes, allowing the speed of sound in the gas in the tube to be calculated with a given frequency and wavelength [49]. Lord Rayleigh explored the theory behind acoustic radiation force and introduced the idea that a sound wave can exert a time-averaged directed pressure on an object, just like light waves [50]. He also made significant discoveries in acoustics, including surface acoustic waves named after him (Rayleigh waves). Based on Rayleigh's theory of acoustic pressure, Altberg first reported the measurement of the absolute intensity of the acoustic wave radiating from the end of a Kundt's tube [51].

In 1906, Vilhelm Bjerknes, studied the effect of radiation forces acting on bubbles in the acoustic field and found that the radiation forces were not only caused by the primary acoustic field; he determined that secondary acoustic forces are produced due to the mutual interaction between gas bubbles in the acoustic field [52]. The radiation forces acting on particles in an acoustic field were investigated in later publications by King [53], Yosioka and Kawasima [54], Gor'kov [55] and Doinikov [56] who have shown theoretically that the main contribution to the radiation pressure exerted by plane travelling waves on rigid and liquid spheres comes from the viscous and heat effects.

Acoustic radiation forces were extended over frequencies above 20 kHz, through the development of ultrasonic wave technology, where human ear cannot longer hear. Accompanied with the early development of ultrasonic sources was the discovery of the piezoelectric effect by the Curie brothers, which directly prepared for the emergence of ultrasonic technologies. In 1915 Paul Langevin, demonstrated the practicality of pulse echo detection with a high frequency of 150 kHz (hydrophone) for object detection. The first in depth study of the effects of ultrasound including radiation force was conducted by Robert Wood and Alfred Lee Loomis, who built the first radiation force balance in 1927 [57]. In their experiments, they successfully created a radiation pressure with sufficient magnitude to support 150 g. Based on these experiments, the first practical instrument using ultrasound radiation force was developed [58]. This instrument, described by W. T. Richards [59], became a prototype for the most common currently used device for measuring ultrasonic power in liquids and for calibration of therapeutic transducers. Ultrasound technology has been developing since then with the invention of new piezoelectric materials such as piezoelectric ceramics, e.g.

lead zirconate titanate and sonar transducers. Those developments resulted in the advancement of applications of ultrasound used in the medical sector. The following diagram in Figure 2.5 illustrates some of the various applications of ultrasound in a variety of fields.

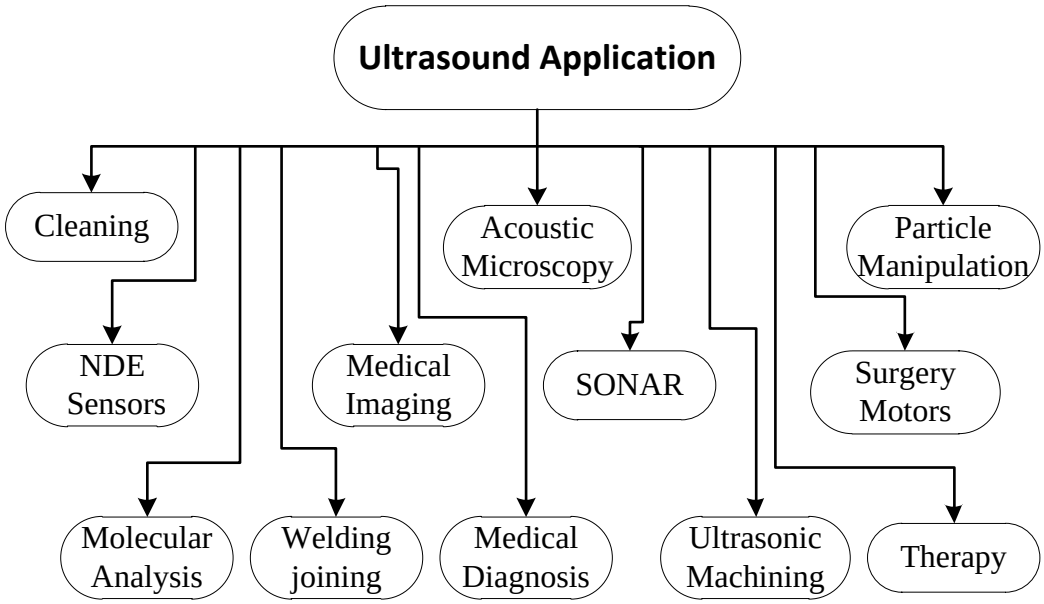

Figure 2.5 Diagram of examples of ultrasound applications in different fields.

Developments of ultrasonic technology in the past years have expanded rapidly in order to provide solutions for the increasing demands for miniaturised and integrated technologies to explore particles, cells and molecules in cell biology and analytical chemistry. Ultrasonic manipulation technology has become one of the most intensively studied methods for contactless manipulation. This technology offers the following advantages: easy integration into microfluidic systems, cell viability and generated forces for handling cells with micron scale dimensions and large-scale manipulation of cells (from hundreds to thousands). Coakley et al. reviewed the observations of ultrasonic radiation forces effect on cells and demonstrated applications in cell concentration, alignment and cell to cell interaction [9]. Generally, ultrasound at frequencies of the order of MHz were used in ultrasound devices for manipulation purposes in order to increase the acoustic pressure threshold of the ultrasonic cavitation on experiments using biological cells.

2.3 Manipulation of micro-objects using ultrasound

In 1990, Wu demonstrated stable trapping of particles and clusters of frog eggs in water with two aligned counter-propagating ultrasound waves of 3.5 MHz [60]. Moroney et al.

demonstrated that the standing Lamb waves can trap particles and bacteria located in a water droplet that is in contact with the membrane [61]. Lamb waves are complex vibrational waves that propagate parallel to the surface that is under test through the thickness of the material. The propagation of Lamb waves depends on the elastic properties of the material and the density of a component. Saito et al. demonstrated 2D cell trapping by using two ultrasound sources to create lattice energy gradients [62], where simply a lattice of nodes was formed in an area of 10 x 10 mm when two transducers were excited.

Since the beginning of this century, the use of ultrasound manipulation techniques has been widely studied for a broad range of biological and medical applications including: cell filtering [63], concentration [64], separation [65] and sorting [1] as shown in the example in Figure 2.6, cell patterning and immobilisation [66], [67], cell washing and mixing [68], [69], [70], culturing of cells in 3-D [71], capture and accumulation of microbubbles [72] and enhancement of sensitivity of biosensors and bioassays [23], [73].

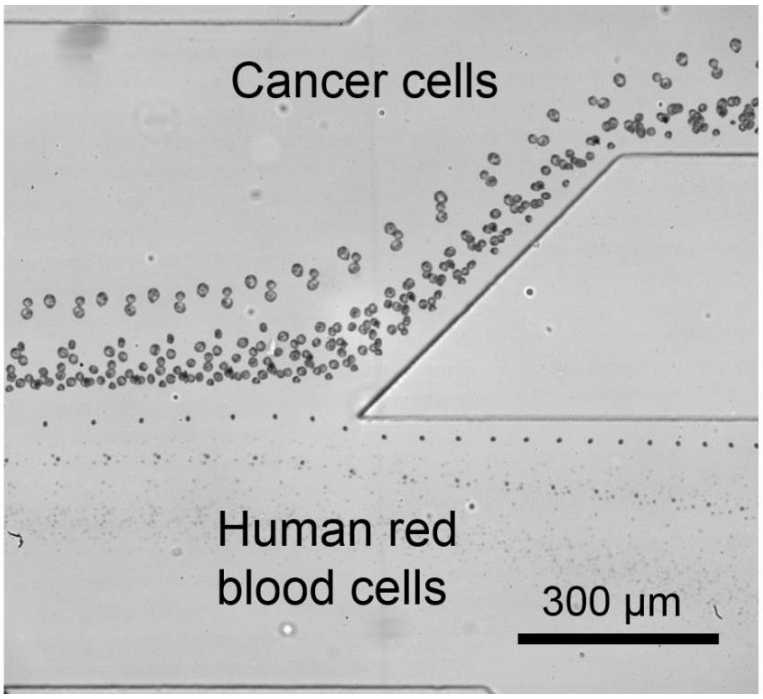

Figure 2.6 Separation of cancer cells from red blood cells in a tilted-angle standing surface acoustic wave device [83].

Ultrasonic standing waves were implemented in order to guide particles suspended in a fluidic laminar flow in devices with split inlets and outlets. In order to achieve stable forces, ultrasonic manipulation devices usually utilise either standing waves, such as standing surface acoustic

waves [74] [75], bulk acoustic waves [76], [77] or quasi-standing waves [78] which are formed when the incident wave meets with the reflected wave, the composite waves are called quasi standing waves. Researchers have achieved a null pressure acoustic field by emitting two ultrasound beams with opposite phase to create a similar effect to a standing wave [79].

2.3.1 Patterning of particles using ultrasound

Many articles in the literature have investigated the fabrication of lead zirconate titanate (PZT) transducers to manipulate particles and cells. A novel device demonstrated in [80] shows a 1D array of PZT transducers was integrated into a multilayer ultrasonic resonator to concentrate particles laterally in the centreline of a microfluidic channel and to move them back and forth along the length of the channel by switching the active elements of the array. Additionally, a piezoelectric cell sorting instrument was introduced in [81] where a PZT actuator was integrated on the fluidic chamber enabling low voltage and low power operation for sorting particles and cells. The technique used is called fluorescence activated cell sorting (FACS). PZT transducers with a matching layer and a backing layer have been used in [82] where two opposing transducers, four in a form of a cross, or eight in a form of an octagon were formed inside a cavity for the manipulation of particles. The mentioned devices with opposing transducers were used in order to form standing waves for trapping and patterning microparticles as shown in Figure 2.7.

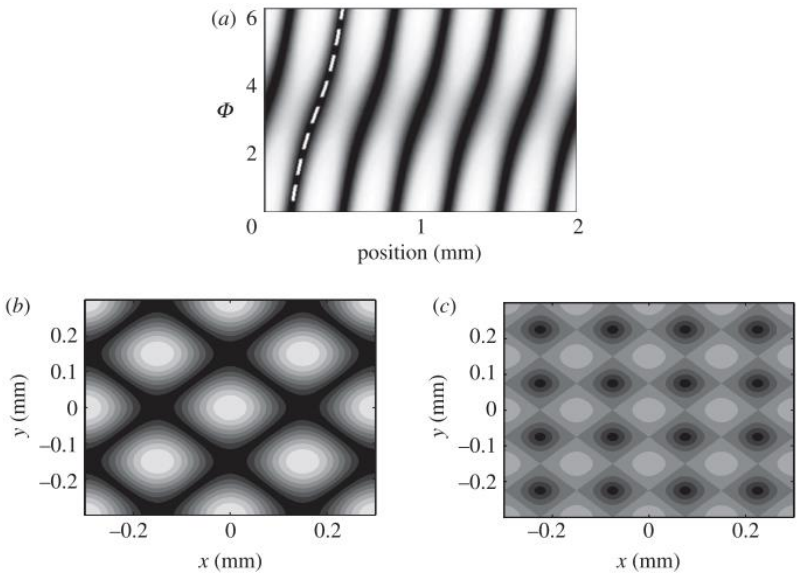

Figure 2.7 Pressure amplitude of (a) counter propagating plane waves from two opposing transducers with reflection coefficient as a function of relative phase (b) of four transducers forming two orthogonal pairs with 0 phase difference between them and (c) of two orthogonal pairs of transducers but one pair at phase $\varphi=\pi/4$ [82].

Other research that achieved advancement in the acoustic tweezers technique realised tuneable particle/cell-patterning. The technique consisted of varying the standing surface acoustic wavefield by using slanted-finger interdigitated transducers (SFITs) [83]. By implementing two opposing slanted-finger transducers a 1D dynamic pattern could be achieved and by using four transducers in a cross formation a 2D dynamic pattern was able to form as shown in Figure 2.8. Furthermore by implementing micro-PZT transducer structures, acoustic trapping of cells and particles can be achieved that enables cell or particle based bioassays performed in a continuous flow format [84]. Other techniques utilise a cylinder tube using a transducer – reflector system for concentrating particles under the effect of the produced standing wave [85].

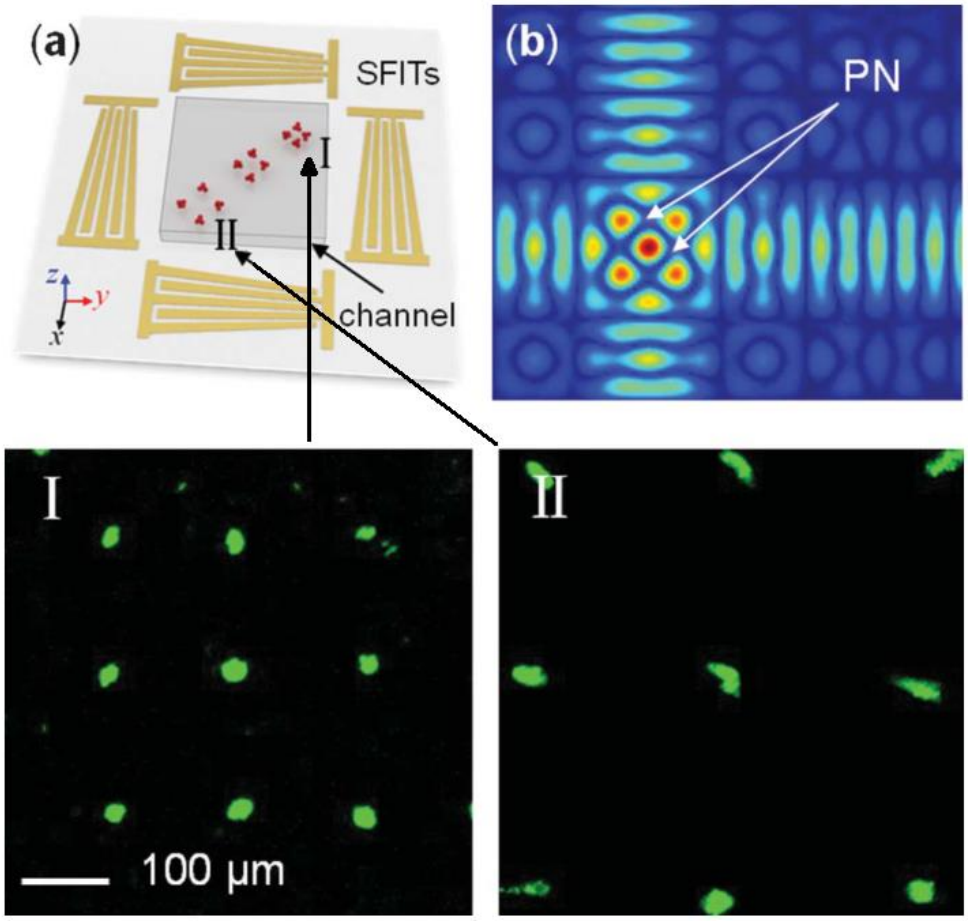

Figure 2.8 2D dynamic patterning of particles using SFITs. (a) Schematic of the 2D dynamic patterning device: the particle pattern in the region corresponding to a smaller finger pitch (higher frequency) has a smaller period, while the pattern in the region corresponding to a larger finger pitch (lower frequency) has a larger period. (b) The simulated distribution of pressure nodes (PN) in a standing surface acoustic wave (SSAW) field with the SAW excited from the low frequency region of the SFITs. Bottom figures I and II show the patterned arrays with periods of 150 mm and 240 mm at the frequencies of 18.0 MHz and 10.9 MHz, respectively. [83].

2.3.2 Discrimination of particles using ultrasound

In the field of acoustophoresis, which means migration by sound, the applications and advances of technology have been continuously growing in the field of particle or cell manipulation and sorting. In both categories, numerous techniques that have successfully achieved manipulation for patterning and sorting can be found [63], [86]. Studies performed on acoustic resonators, have exposed the capability to focus cells in nodal planes in a standing wave configuration, where plasma separation from whole blood was achieved at a flow rate of 2 mL/min [87]. Enhanced cell sedimentation can be identified as the most common application [88] of ultrasound sorting. Sedimentation can be achieved by aggregating particles and cells into the pressure nodes of a standing wave with the condition that the nodal planes are parallel to the gravity direction.

Microchip-based devices for acoustic cell manipulation were developed by the group of T. Laurell where the design of half wavelength, $\lambda/2$, resonators were placed in parallel with a silicon chip [89]. By exciting the transducer at its resonance frequency the standing wave was formed at half the wavelength with respect to the width of the channel, this way the transversal mode of operation can be established [90]. The separation of particles with negative acoustic contrast factor and cells with positive contrast factor was exploited by developing a system for separating lipid particles from raw milk product [91]. By changing the acoustic properties of the carrier medium, appropriate conditions can be established where cells or particles that normally have acoustic contrast factor of the same sign, could have either opposite signs or their acoustic contrast factors would alternate enough for the target cells to be separated. This was accomplished by adding caesium chloride to the carrier solution [92], which created a condition where two polymer particle types that were inseparable in water could be separated in the modified medium as shown in Figure 2.9. In the same experimental set-up it was demonstrated that the acoustophoretic separation of a mixture of red blood cells and platelets in saline solution was improved by adding caesium chloride to the central buffer flow, therefore changing the relative acoustophoretic mobility of the platelets in comparison with the red blood cells.

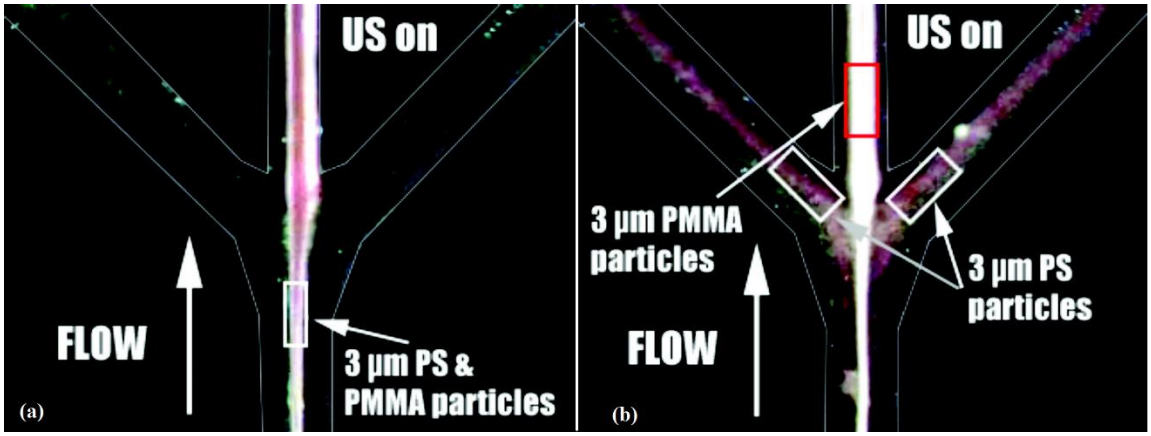

Figure 2.9 Microscope image showing the end of the separation channel. (a) No separation of 3µm red polystyrene (PS) and white polymethyl(methacrylate) (PMMA) particles was observed when suspended in distilled water (b) 3 µm red PS and white PMMA particles could be separated after caesium chloride (CsCl) (0.22 g/mL) was added to distilled water, in order to change the density [92].

An improved sorting device was presented by Jakobsson et al. [93], where they introduced a 2D acoustic pre-focusing step, reassuring that all the particles introduced in the flow were positioned in the same flow vector. For high-performance cell sorters prefocusing in the same flow vector is required and in the case of acoustophoretic sorters the optimal way is done by positioning the particle to be sorted where the acoustic radiation force is at its maximum as shown in Figure 2.10. Other techniques of prefocusing have used an inertial flow based alignment of the particles followed by a standing surface acoustic wave based system for sorting the targeted cells [94].

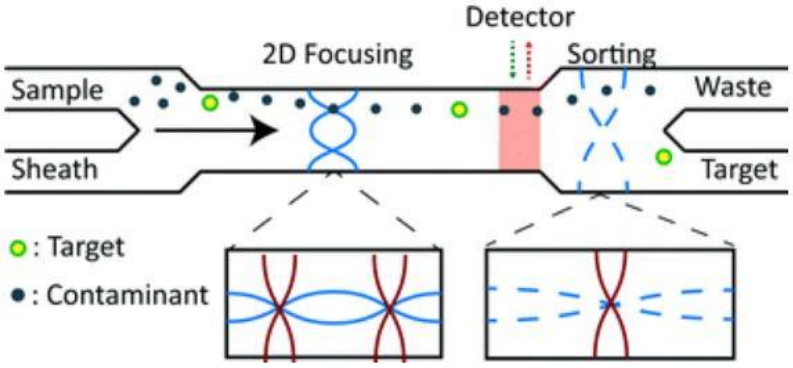

Figure 2.10 Prefocusing stage for particle and cell sorting [93].

2.4 Microfluidic channels

Microfluidics describes the research field of the control and manipulation of fluids on the sub-millimetre length scale. This has become possible by the adoption of MEMs fabrication technologies developed in the semiconductor industry to create devices that can be used to control and manipulate fluids [95]. They are usually in the form of networks of channels with lengths varying between 1-1000 μm, allowing the fluid sample to be induced and moved through. The ability to manipulate particles in volumes of fluid ranging from picoliters (pl) up to several millilitres, leads to many possible applications for the medical and biological industry. Chemical assays can be performed using only very small sample volumes (pl), potentially reducing the cost of reagents. Such an example is the detection of HIV and syphilis via an ELISA assay performed on a portable and low-cost microfluidic chip [96]. Microfluidic devices have proven to be useful as means of cell manipulation, since the fabricated sizes approached the cell size (μm), such as isolation of circulating tumour cells from whole blood using polymer based microfluidics in a high throughput manner [97].

The materials initially used to manufacture microfluidic devices was the same materials used in the semi-conductor industry, i.e. silicon and glass, and were created using standard post-fabrication procedures like photolithography and etching techniques. The limitation of using those materials were the complex bonding protocols, inflexibility and opacity in the case of silicon and relative high cost. In 1998, Whiteside's group pioneered the use of polydimethylsiloxane (PDMS) [98], a flexible, elastic and transparent polymer to create microfluidic channels. PDMS as a material has a number of advantages, such as relatively easy to pattern fluid channels into it, it is transparent therefore it is compatible for optical detection with various microscopy techniques, it is nontoxic making it ideal for cell applications, its surface chemistry can be tuned to be either hydrophilic or hydrophobic. Additionally, it can be bonded reversibly by having molecular contacts with the surface or irreversibly if exposed to air plasma by formation of covalent bonds to glass coverslips and other substrates including itself. Finally, it is a low-cost material compared to silicon. Due to these advantages PDMS has become a very popular material in many microfluidics applications. An example of the fabrication and operation principle of the PDMS microfluidic material network is shown in Figure 2.11.

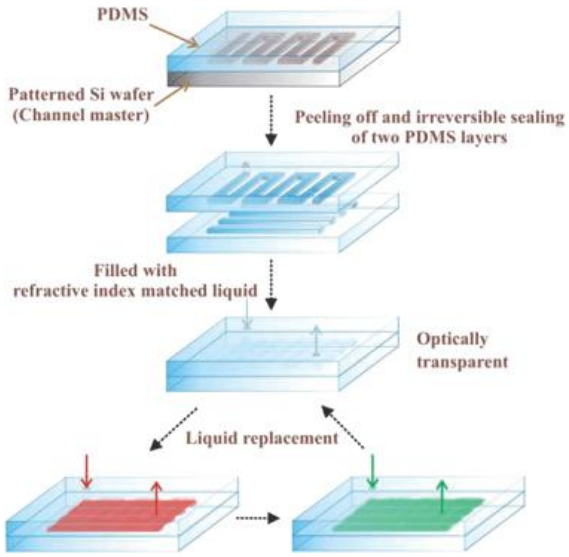

Figure 2.11 Schematic flowchart of the fabrication and operation principle of the PDMS microfluidic material network that can change colour on demand. Image reproduced from [99].

2.5 Surface acoustic wave devices

Surface acoustic waves (SAW) are produced at the surface of a piezoelectric material substrate. The most commonly used material in the literature is lithium niobate where interdigitated transducer (IDT) electrodes are created as shown in Figure 2.12. The frequency of the formed waves is determined by the size of the finger electrodes, the distance between them and the ultrasound wave propagation speed on the substrate. Using two opposing IDTs, standing SAWs are generated and can be coupled into the cell or particle containing liquid in a channel [99]. SAW devices have very efficient fluid-structural coupling owing to the presence of most of the energy adjacent to the interface. This makes them ideal for microfluidic actuation and manipulation applications. The presence of elastic energy at high frequencies, produced by the SAW, is responsible for the generation of high accelerations, reaching the maximum vibration velocity in the order of 1 m/s, resulting in an acceleration of at least 10^8 m/s^2. Microfluidic applications can be carried out entirely on chip powered by a palm-sized portable electronic driver circuit [100]. SAW microfluidics can address one of the most fundamental restrictions in microfluidics that excludes the extensive implementation of practical lab-on-a-chip devices, such as delivery of a complete microfluidics solution at the microscale, including sample preparation and analyte detection [101].

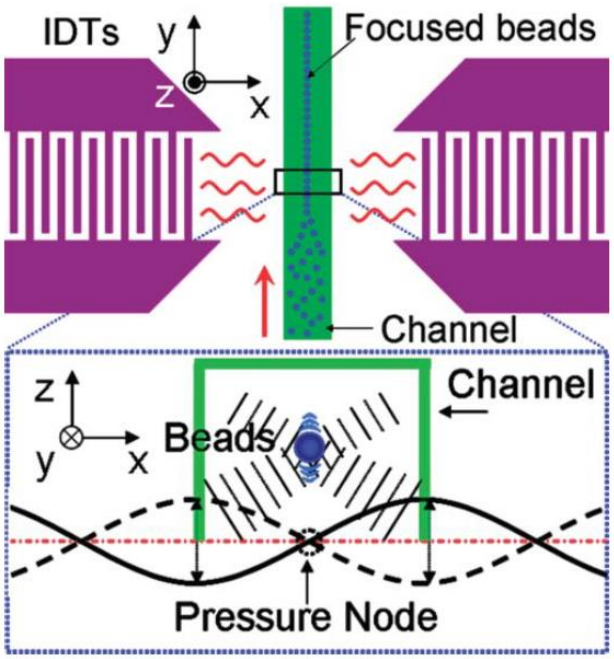

Figure 2.12 Schematic illustration of the working mechanism of a SAW focusing device [100].

2.6 Bulk acoustic wave devices

Piezoceramics such as lead zirconate titanate are also used for the construction of bulk acoustic wave (BAW) transducers. The resonance frequency of the transducer is proportional to the thickness of the piezoelectric material, thus in a specific frequency for each thickness the device works the best. The use of electrodes enables an electrical signal through the transducer which results in a mechanical motion under the form of a travelling sound wave. The wave propagation takes place in two basic forms, longitudinal and transverse waves. BAW transducers are usually connected to the microfluidic chip containing the channel through a coupling layer using glue , water or glycerol [102] to enable the transmission of the acoustic wave [90]. Similar techniques involve the attachment to an external wedge base and then joining them with glue [103]. The microfluidic chip acts as an acoustic resonator, where its dimensions are chosen to match a certain resonance condition, leading to a frequency that is chosen to generate a plane standing wave across the width of the microfluidic channel. The most common resonator designs employ dimensions to support half a wavelength where a single pressure nodal plane is generated in the centre of the microchannel, while resonances in the vertical direction are suppressed by the geometrical mismatch [104]. When referring to the resonance frequency, it means the fundamental frequency of the resonator. Nevertheless, in the literature multiple pressure nodal planes at higher harmonic frequencies are also used. An

example of a layered resonator is given in Figure 2.13, where a reflector and two opposing transducers are used.

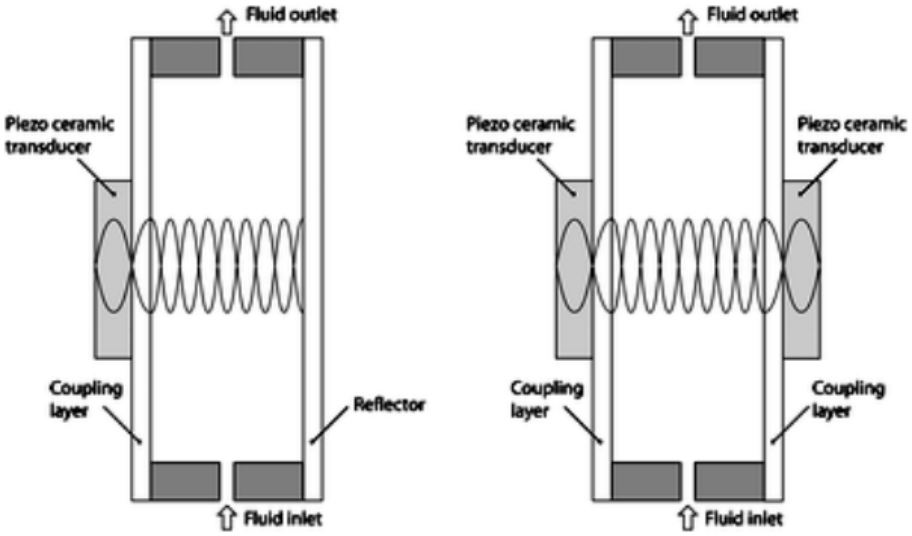

Figure 2.13 Schematic of a layered transducer using a reflector (left) and using two opposing transducers (right), image adapted from [90].

The dimensions and the material properties are the key aspects when designing a transverse resonator. The material provides the transmission of the acoustic energy into the medium at low loss (low damping effect) and exhibits high acoustic reflection properties to support a standing wave. The Q-factor is an indicator of the transmitted energy into a resonator. It describes the ratio of the energy stored in the actuated resonator over the energy losses during actuation (damping) at a specific resonant frequency. A high Q-factor device resonates with larger amplitudes at the resonance frequency and produces larger acoustic forces for smaller power inputs compared to a low Q-factor device [105]. An example of a transverse resonator is shown in Figure 2.14.

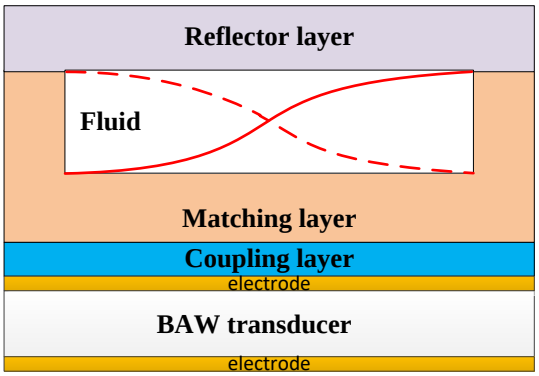

Figure 2.14 Schematic of a transverse BAW transducer attached to a microfluidic channel.

2.7 Acoustic streaming in microfluidic devices

When a transducer fabricated on the surface of a piezoelectric material is excited a travelling surface acoustic wave is transmitted. If a fluid is placed in the path of the surface waves it will absorb some of the energy of the SAWs during the transfer from the SAW substrate to the fluid. The absorbed energy has the form of a longitudinal pressure wave that propagates into the fluid at the Rayleigh angle (θ_R). The displacement fields of the leakage wave created by two opposing travelling SAWs are demonstrated in Figure 2.15. When SAWs that are propagating in opposite directions reach the sample fluid inside the microfluidic channel, the SAWs are transformed to leakage waves inducing pressure fluctuations, then the longitudinal pressure waves are emitted into the fluid at the reflection angle. These newly formed pressure waves can cause streaming and it can be observed in droplets and fluids in microfluidic channels placed in the path of the SAW beam.

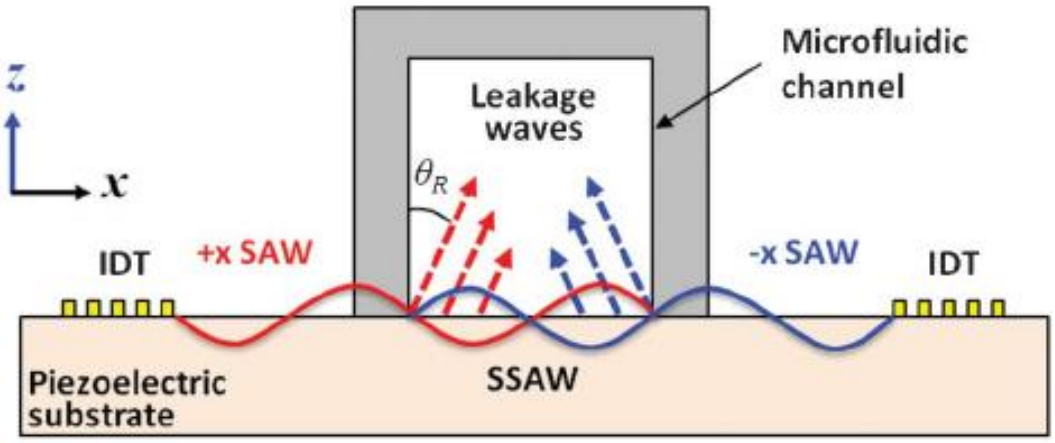

Figure 2.15 A cross-section schematic of a microfluidic channel and the two opposing transducers, establishing a SSAW across the channel width. This SSAW radiates acoustic leakage waves into the liquid at the Rayleigh angle. Image reproduced from [107].

The generated streaming can be powerful enough to drive fluid handling processes at microlitre and nanolitre fluid volumes. Pumping of a fluid from an inlet to an outlet through a microfluidic channel has been demonstrated [106], as well as in a closed PDMS channel [107]. The acoustic streaming itself has proven to be a useful method to mix fluid samples for cleaning steps and to mix reagents in microfluidic volumes, where the flow is often dominated by low Reynolds numbers [108]. SAW streaming in microfluidic channels has also been used to sort droplets and cells by driving them to separate channels. The streaming effect has also been demonstrated to remove non-specific binding on protein microarrays [109].

Flow patterns in fluid samples can be controlled by choosing the position of the saw beam relative to the fluid. By exposing half a droplet using a SAW beam, centrifugal flows can be set up in the droplet which can be used to sort particle and cells based on size and density. A similar process of size dependent particle capture using a streaming vortex created by a SAW beam is possible inside a microfluidic channel [16].

2.8 Sheath flow in microfluidic devices

Sheath flow is the injection of the sheath fluid from two lateral inlets to the main inlet of the microfluidic channel. Sheath flow focusing might be the most common method that has been implemented in microfluidic devices, which is used to drive the fluid of interest in a controlled focused laminar way inside the microfluidic channel. Many techniques have been realised for this type of focusing, such as pressure-driven sheath flows free of particles in order to focus

the particle suspension into the desired area [110], [111], [112], [113] or by using electric field-driven [114]. In general, one or more sheath flow fluids need to be used in order to achieve particle focusing.

In general microfluidic designs that are capable of 3-D hydrodynamic focusing require multiple sheath inlets and involve several alignment steps, which make the fabrication and operation of the device complicated. A novel approach has been proposed by Howell et al. using grooved microfluidic channels for achieving 3D sheath flow focusing [115]. Two basic designs have been implemented, a stripe-based and a chevron-based design. In the chevron design, a typical 2D sheath flow focusing is achieved by using two equal sheath flows that place the sample stream in the centre of the channel. Then, several pairs of chevrons cut into the top and bottom walls of the microfluidic channel are used to direct sheath fluid from the sides to the middle of the sample stream in the vertical direction. This isolates the sample stream from the top and bottom walls of the channel. The number of chevron pairs and the sheath-to-sample flow rate ratio can control the height and width of the focused sample stream, respectively. Figure 2.16 shows a schematic of the design of the chevron sheath flow channel.

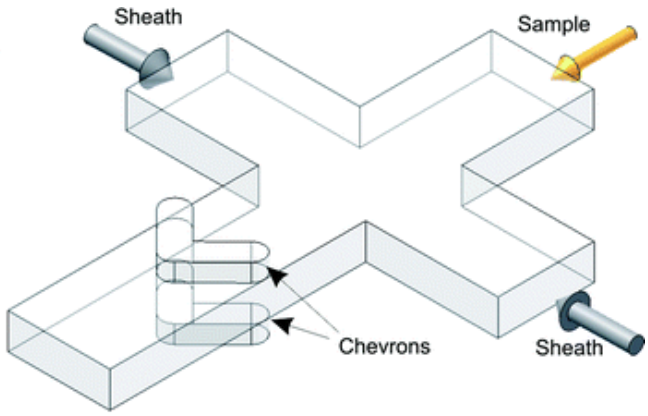

Figure 2.16 Schematic of the chevron based sheath flow design [117].

The chevron-based 3D sheath flow focusing method has demonstrated that it can focus polystyrene particles with a 5.6 μm diameter at a flow rate of 10 μl/min [116]. The same 3D sheath focusing design has been integrated into a flow cytometer for multiplexed detection of bacteria and toxins coated onto bead surfaces [116], [117]. Other designs of sheath flow focusing for microfluidic flow cytometers have implemented a micro-weir structure positioned right beneath the optical detection system [118]. Using this structure a separation of 5 μm and

10 μm in diameter polystyrene particles has been achieved in the vertical direction [119] with a reported flow rate of aqueous sample reaching approximately 14 μl/min.

Using sheath flow focusing, particles are typically focused to a stream travelling along the centre plane (2D focusing) or centreline (3D focusing) of a microfluidic channel. However, in some applications it is desired for the particles to flow in close proximity to the sensing electrodes deposited on the channel floor in order to increase the signal to noise ratio. This kind of vertical confinement can be achieved using a 2D horizontal sheath flow focusing with a stepped outlet channel [120]. Moreover, another approach is to use a third sheath to vertically squeeze the particle stream as demonstrated by Watkins et al. [121]. The 2D sheath flows force particles in the sample stream to move in a single file manner, while the 3D sheath flow guarantees the particles to be transported close to the sensing electrodes. With the use of this device a count of T lymphocytes at a flow rate of 4 μl/min and differentiation of live from dead/dying lymphocyte populations has been achieved.

2.9 Particle and cell manipulation using ultrasound microfluidic devices

Many studies in the literature have used ultrasound microfluidic devices in order to manipulate particles and cells by utilising a range of techniques such as fluorescence activated cell sorting (FACS) [122],[99]. This can also be done by combining two methods such as FACS and fluorescence activated droplet sorting (FADS) in microfluidic channels [123] operating at high sorting rates in a continuous flow. The aforementioned techniques rely on labelling the particles or cells beforehand in order to be able to identify and sort them providing high purity sorting but in a low throughput if multiple cells are required to be sorted. There are other techniques of label free handling of particles and cells that consist of size separation by free flow acoustophoresis (FFA). In FFA the net acoustic force drives cells or particles perpendicular to the direction of the flow towards a pressure node while they are travelling along the flow. Basic concepts of size based particle separation were performed by Giddings [124], where an external force field is allowed to act on a particle suspension perpendicular to the direction of the flow and particles that experience a higher force are translated faster across the laminar flow streams as illustrated in Figure 2.17, such a technique is called split flow thin fractionation (SPLITT). The schematic illustration in Figure 2.18 outlines the principle of free flow acoustophoresis in multiplex mode separation created by different forces acting on the particles depending on their

size. The same concept can be implemented with focused flow by utilising a pre-alignment stage and by sorting the particles according to their size as shown in Figure 2.19.

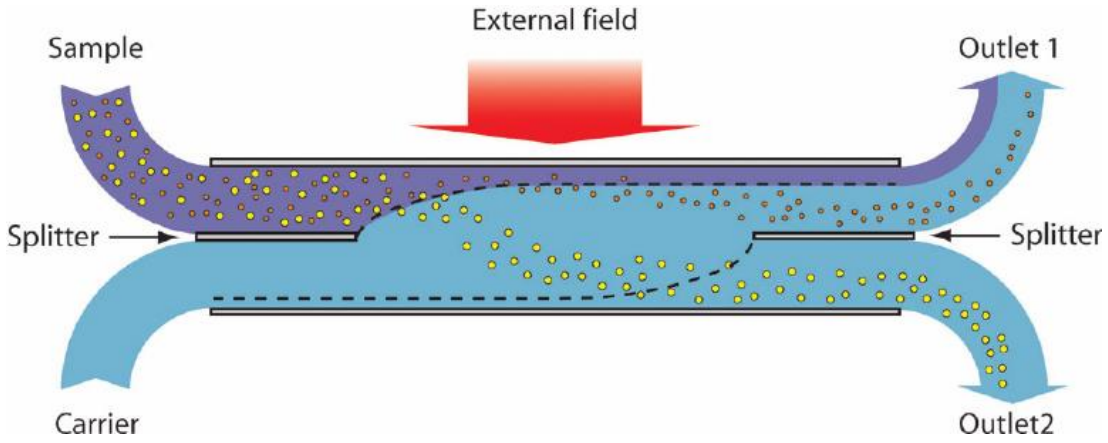

Figure 2.17 Schematic illustration of the principle of the split flow thin (SPLITT) fractionation. Image adapted from [127].

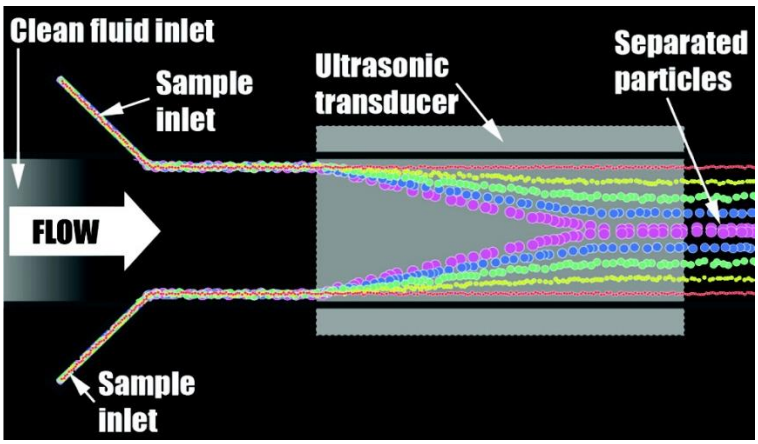

Figure 2.18 Schematic illustration of free flow acoustophoresis for multiplex separation of mixed suspensions. Image adapted from [92].

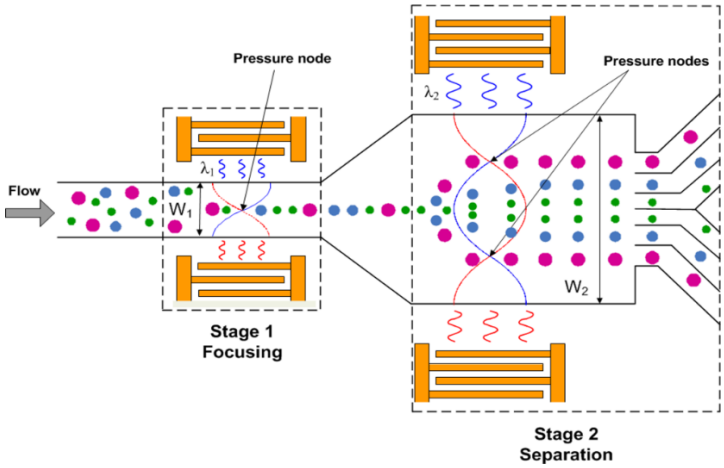

Figure 2.19 Schematic illustration of pre-focusing staged acoustophoretic SAW device for multiplex separation of mixed suspensions. Image adapted from [128].

The separation in free flow acoustophoresis mode is controlled by the magnitude of the employed force field and the flow rate, which depends on the retention time in the acoustically activated zone. The spatial dimension of a band of a given particle size at the channel outlet is defined by two factors. Firstly, by the width of the particle fraction when it enters the separation zone in relation to the channel width and the distance that the particle band traverses the channel before reaching the outlet. The second factor reflects the dispersion of the particle band as a function of the parabolic flow profile from top to bottom of the flow channel which means that particles display significantly different retention times in the acoustic field and hence have a lateral position in the channel which is dependent on the original location in the flow profile [125].

Standing surface acoustic wave (SSAW) devices have been vastly utilised for applications of manipulation in continuous flow of particle and cells in microfluidic devices. Shi et al. first reported SSAW-based continuous separation of particles in a flow stream in a PDMS microfluidic device [126]. Following that work Nam et al. developed a similar device setup and demonstrated the function of the device for sorting particles of different size, in a mixture of large and small particles of 10, 5 and 1 μm in diameter, that were pumped through a separation channel from the central inlet while introducing sheath flow from the side inlets of the device as shown in Figure 2.20.

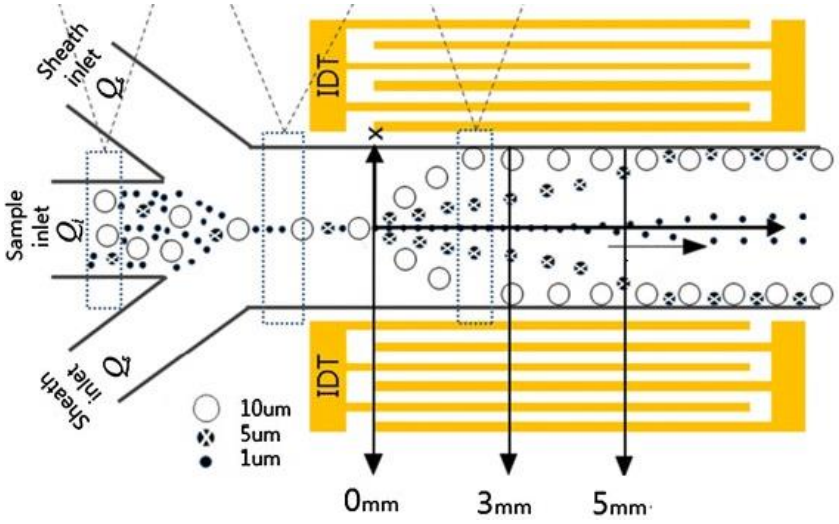

Figure 2.20 Diagrams of a microfluidic device and working principle. The sample and sheath flows containing particles of three different diameter sizes (1, 5, and 10 μm). Image reproduced from [131].

The same device setup was applied in order to sort red and white blood cells from platelets due to the size difference between them [127]. The SSAW-based sorting process effectively removed 99% of blood cells and accomplished 74% separation efficiency for platelets. A different technique used by Ding et al. sorted particles in a constant flow. The implementation was similar to the one mentioned above but with the difference that the interdigitated transducers were fabricated in a tilted angle to the microfluidic channel [74] as shown in Figure 2.21. Furthermore, the ability of the tilted angle standing surface acoustic wave (taSSAW) method was demonstrated for human cancer diagnostics by accurately separating MCF-7 breast cancer cells from normal human white blood cells. Another approach for particle and cell manipulation in SSAW devices is to separate them based on their physical properties, such as the contrast factor φ. Petersson et al. utilised acoustic forces in a standing wavefield to discriminate lipid particles from erythrocytes in whole blood, since the contrast factor of erythrocytes has a positive sign they would agglomerate on the nodes while the lipids with a negative sign of the φ they would gather at the antinodes. The presented technology proposed a new method of cleaning, i.e. removing lipid emboli from shed blood recovered during cardiac surgery.[18]

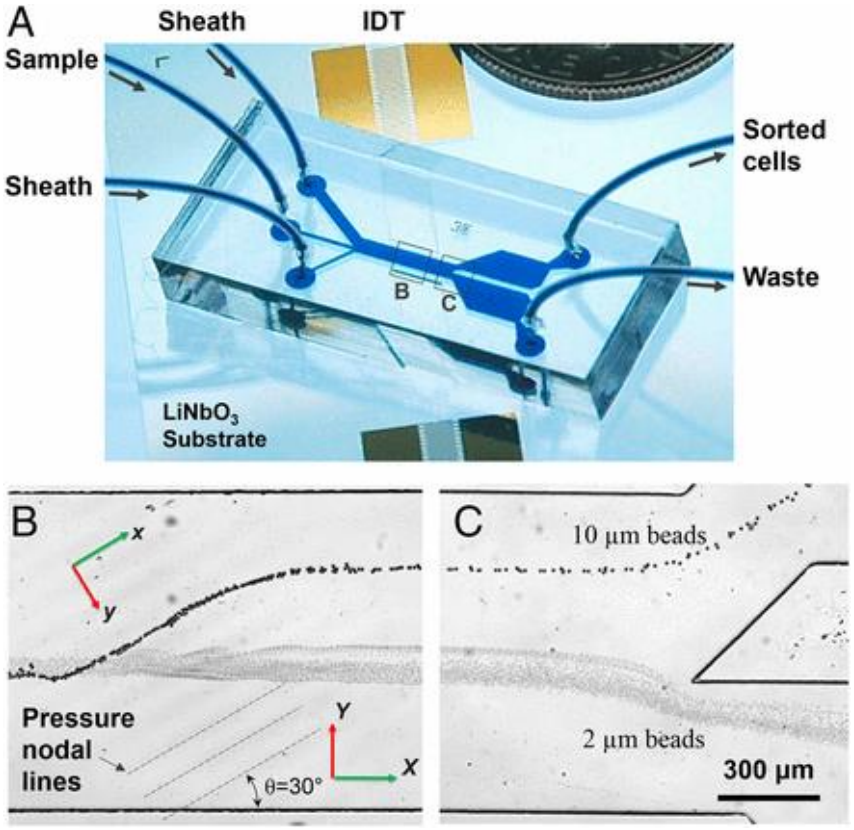

Figure 2.21 Schematic illustration of working principle and device structure. (a) Photo showing a taSSAW-based cell-separation device. (b) and (c) Separation process for 10 and 2 μm diameter polystyrene beads in the taSSAW working region and the outlet region, respectively [74].

3. Theory

3.1 Introduction

The piezoelectric effect was discovered in 1880 by Jacques and Pierre Curie. The principle is that when a mechanical pressure is applied on specific materials such as quartz or topaz, electrical charges appear and the voltage acquired is proportional to the initial applied pressure. Such materials are called piezoelectric materials, and by using them a few applications were developed. The first application was the piezoelectric ultrasonic transducer. Furthermore, the piezoelectric effect can be reversible, which means a transducer could transform the mechanical energy of the applied pressure to electric energy by the acquired voltage and can also transform the electric energy into mechanical energy by using the converse piezoelectric effect,.

3.2 Materials with piezoelectric properties

Both piezoelectric and passive materials are used in ultrasound standing wave device for manipulation of particles and cells. The properties of the piezoelectric material that compose the ultrasonic transducer affects the amplitude of the output acoustic energy, thus the piezoelectric material is an important factor to be considered. A diverse set of piezoelectric materials can be used as active elements for the construction of an ultrasound transducer which include, piezoceramics [18], [128], piezopolymers [129], single crystals [130] and piezocomposites [131], [132]. All piezoelectric materials are anisotropic and centre asymmetric. Crystals are isotropic from the optical point of view, but they are anisotropic in terms of elasticity.

Among the family of the piezoceramic materials, the most commonly used is the Lead Zirconate Titanate (PZT) described by $[Pb(ZrxTi1\text{-}x)]O3$, $(0 \leq x \leq 1)$, which is an intermetallic inorganic compound that has been a research subject since 1952 [133]. Many applications have been found in the fields of micro-electro-mechanical systems (MEMS) and nano-electro-mechanical systems (NEMS) that use PZT material. PZT is a metallic oxide based material that has good piezoelectric properties, such as electromagnetic coefficient, providing higher sensitivity and operation in greater temperature from previously developed piezoelectric

materials such as Barium Titanate (*BaTiO3*) or quartz. A great variety of PZT forms have been developed by altering the ratios between the Zr and Ti and the dopants. A wide range of PZTs is commercially available for sensing applications, actuators, transducers and generators.

According to their properties piezoceramics can be categorized as hard or soft. Piezoceramics defined as hard have the advantages of low dielectric losses, high mechanical quality factor (*Qm*) and better linearity compared to the soft. This makes them ideal candidates for particle and cell manipulation applications, since the transfer of the maximum possible power is the main consideration. In comparison, the soft piezoceramics have higher sensitivity, permittivity and displacement, but as already mentioned they have higher losses and lower *Qm*. Thus soft piezoceramics are more suitable for sensing applications, since the sensitivity is the key characteristic. A comparison between the properties of the soft and hard piezoceramics is given in Table 3.1. The electromechanical coefficient k^2 is one of the most defining properties which gives the amount of the applied electrical energy that is converted into mechanical:

$$k^2 = \frac{d^2}{s^E \varepsilon^T} \tag{3.1}$$

where d is the piezoelectric strain coefficient, s is the mechanical compliance with E as superscript indicating that the compliance is measured with closed circuit, and ε is the dielectric constant where T denotes that there are no external forces.

A piezoelectric material can be characterised by its elastic, piezoelectric and dielectric properties. These properties are related to the stress T, strain S, dielectric displacement D and electric field E, which are produced by the piezoelectric effect. There are different ways of writing the fundamental equations depending on which variables are of interest, the basic piezoelectric equations are given in the next equations, two of the elastic equations are shown in equation (3.2) and two of the dielectric equations are presented in equation (3.3):

$$S = s^E \cdot T + \left[d\right]^t \cdot E \qquad T = c^D \cdot S - h \cdot D \tag{3.2}$$

$$D = d \cdot T + \varepsilon^T \cdot E \qquad E = -g \cdot T + \left[\varepsilon^T\right]^{-1} \cdot D \tag{3.3}$$

where g is a constant and c is the elasticity coefficient with D as superscript denoting that it is measured in open circuit.

Table 3.1 Comparison of Soft and Hard piezoceramics key characteristics

List of Characteristics	Soft	Hard
Electrical Resistance (*R*)	very high	lower
Dielectric Constant (ε)	larger	smaller
Electromechanical Coupling Factor (*k*)	larger	smaller
Linearity	poor	better
Mechanical Quality Factor (*Qm*)	lower	higher
Piezoelectric Constants	larger	smaller
Permittivity	higher	lower
Coercive Field	low	higher
Dielectric Losses	higher	lower
Polarization / Depolarization	easier	more difficult

A high electromechanical coupling coefficient is required for high acoustic reflection applications, providing the advantage of decreasing the insertion losses of the device. If the coupling coefficient is low that would limit the relative bandwidth [134]. Relying on its specific characteristics PZT can be processed in forms such as thin and thick film or bulk form depending on the application. For manufacturing piezoceramics in bulk form, high temperature 1100 ºC$\leq T \leq$1700 ºC is required, for achieving the desired patterns coming from raw material form. As the manufactured process described, bulk PZTs are, in the most cases, dense, robust and of low porosity. A drawback of bulk PZTs is that they are quite thick (over 0.5 mm) in comparison with other PZTs. However, if required, lower thickness can be achieved during the fabrication of the transducer but is highly cost effective. That disadvantage of bulk PZTs can be overcome by utilising thin and thick film PZT devices, achieving less than 0.2 mm of thickness, that are commonly deposited directly on the substrates. The thickness of deposited PZT film has to be approximately the same as the thickness of the substrate, otherwise the effective piezoelectric response of the PZT film will vary from the one of the bulk PZT, due to stresses within the film caused by clamping of the substrate.

PZT structures have topped the industrial market over the past years, but due to their environmental potential risks derived from the toxicity of lead (Pb) when processed at high temperature [135], the scientific community has turned to alternative lead free piezoelectric materials that are more environmental friendly. Though, till recent development of lead free piezoelectric devices advances, no suitable replacement of PZT regarding its performance has been established. Lead free piezoelectric materials have poor durability and weak piezoelectric effects [136]. Recent articles are investigating the potential use of lead free piezo materials and exploring the mechanical stress [137] and that may worth considering in the future.

Piezoelectric polymers have high piezoelectric stress constant *e*, which makes them better for high sensitivity sensor applications than ceramics. Due to low elastic stiffness factor C^D piezoelectric polymers are tough and because they are lightweight they have the advantage of processing flexibility. As a typical piezoelectric polymer, Polyvinylidene fluoride (PVDF) is fabricated in thin film form and has many applications in sensors, transducers and even surface acoustic wave devices. Many combinations between other piezoelectric materials have been studied to enhance the performance and durability, such as sandwich PVDF thin film between composites [138], and copolymers such as (PVDF-TrFE) films as sensing components [139] with the advantage of high electromechanical coupling factor *k*. One of the common purposes of piezopolymers is the fabrication of flexible devices.

Piezocrystals are the oldest known forms of piezoelectric materials and were discovered by J. and P. Curie and were developed later for acoustic applications. Those crystals were gradually replaced by PZT, though Lithium Niobate $LiNbO_3$ is still one of the most used substrates for particle manipulation applications. Relaxor ferroelectrics are materials which have a spontaneous electric polarization that can be reversed by the application of an external electric field. They exhibit high electrostriction which is a property that causes them to change their shape under the application of an electric field. The relaxor ferroelectric phenomena were first found in Pb(Mg1/3Nb2/3)O3 PMN the lead magnesium niobate solid solution system in 1958. Furthermore ferroelectric single crystals are relaxor-PT based and compared to the traditional PZT ceramics, the piezoelectric coefficient d_{33} is increased and the electromechanical coupling factor k_{33} is increased from <70% to >90% [140]. For instance, some of those materials are $(1-x)Pb(Mg_{1/3}Nb_{2/3})O_3–xPbTiO_3$ type (PMN–PT), $(1-x)Pb(Zn_{1/3}Nb_{2/3})O_3–xPbTiO_3$ type (PZN–PT) and $(1-x-y)Pb(In_{1/2}Nb_{1/2})O_3– yPb(Mg_{1/3}Nb_{2/3})O_3–xPbTiO_3$ type (PIN–PMN–PT).

3.3 Ultrasonic transducers

Piezoelectric ultrasonic transducers convert the applied mechanical energy to electric by the direct piezoelectric effect and use the converse piezoelectric effect to convert the applied electric energy to mechanical. A typical structure of a piezoelectric ultrasonic transducer is assembled with a layer of piezoelectric material using thin electrode layers such as silver, on both sides which are wire-connected. The acoustic impedance between the piezoelectric material and the medium to be introduced to, are used for matching in order to improve the energy transmission. Matching layers are located on the front side of the piezoelectric material. The backing layer is placed on the back sided plate of the transducer for a range of purposes. One is to reduce the vibration of the piezoelectric element, and the other is to attenuate and absorb the transmitted acoustic energy in that direction which is called absorber [141], or to reflect the acoustic energy which is called reflector [142]. Depending on each application purpose of the backing layer, the material is chosen accordingly [143]. Figure 3.1 illustrates the complete assembly of a transducer, as well as showing the polarisation of the electric signal depending on the stretch of the material and vice versa.

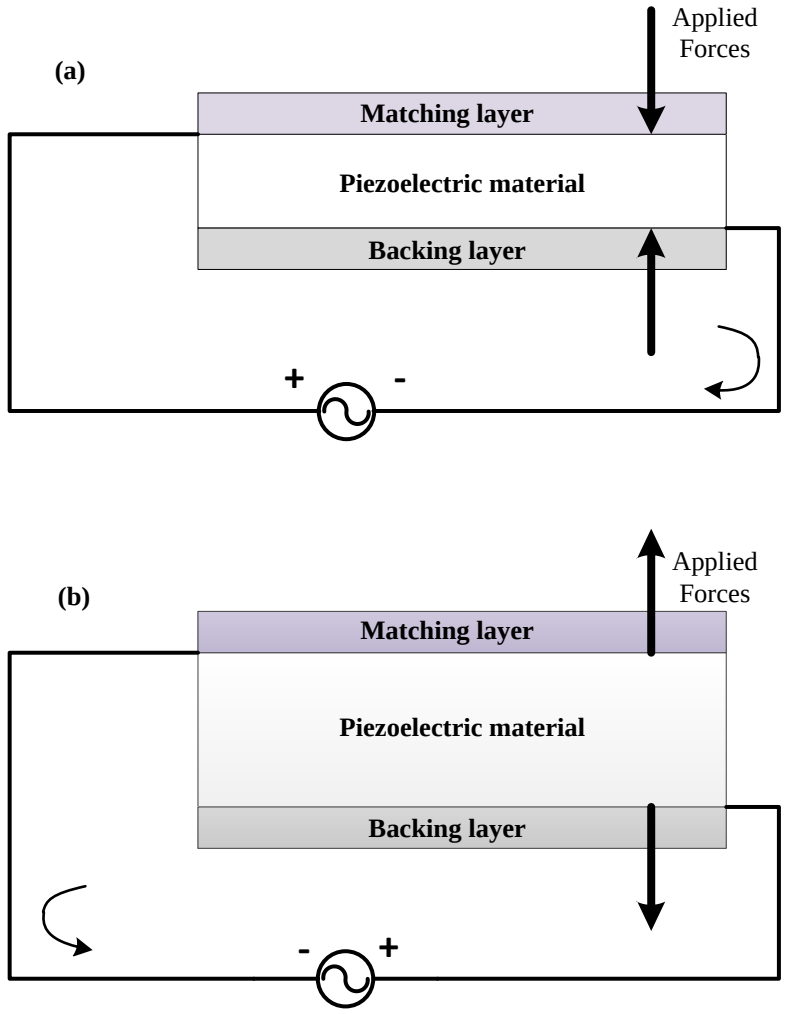

Figure 3.1 Schematic diagram of a piezoelectric ultrasonic transducer (a) when compressing (b) when expanding.

The antiresonant frequency (f_a) of a piezoelectric transducer, is related to the thickness of the material and the longitudinal velocity of sound (υ_L) is following the material stretching direction. If the internal losses are not taken into account, then f_a is considered equal to the frequency of maximum impedance (f_n) and the parallel resonant frequency (f_p). On the other hand, the resonant frequency (f_r) is considered equal to the frequency of minimum impedance (f_m) and the series resonant frequency (f_s).

Ultrasonic transducer arrays are commonly used in practical applications, due to the lack of a single element fabricated transducer, not only in the field of medical sensing and imaging [144] but also in the field of non-destructive testing [145]. Ultrasonic transducer arrays utilise multiple transducer elements. By controlling each element from the dynamic point of view [146] electronic beam steering, focusing and scanning can be achieved [147]. The benefits of

such manipulation can lead to more reliable devices, reduction of the testing time [148] and better quality of measurements. The general types of geometries of transducer arrays are, the 1D linear arrays, the curvilinear or circular arrays, annular arrays, x-D arrays where 1<x<2 and 2D arrays that are shown in Figure 3.2.

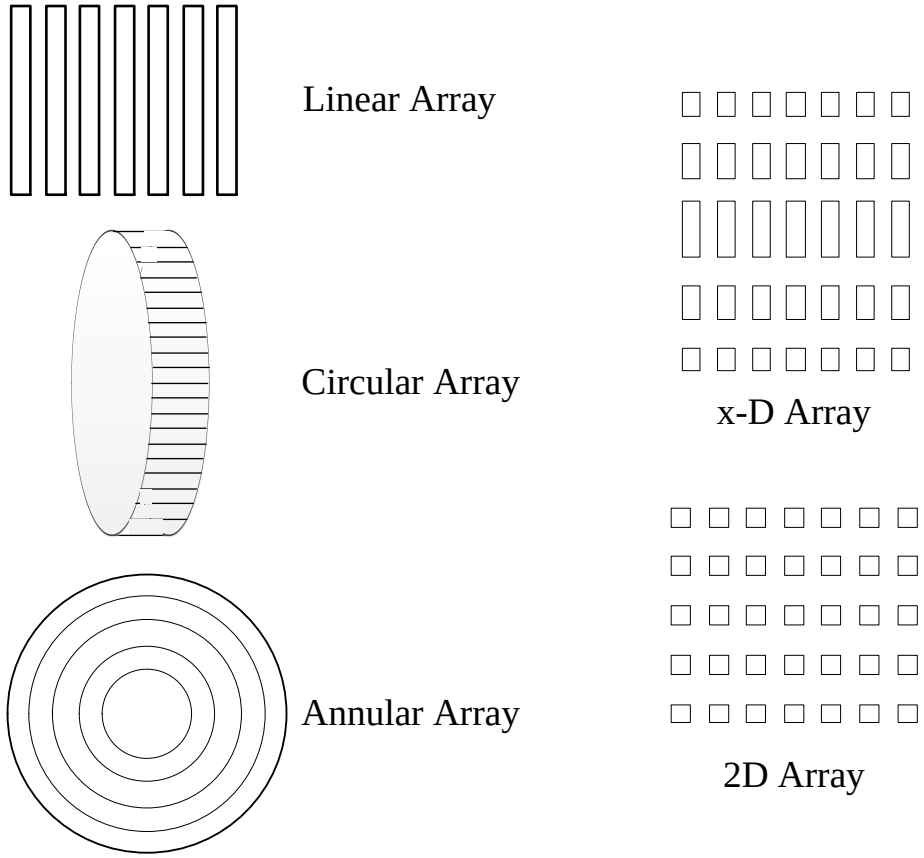

Figure 3.2 Types of transducer arrays.

In 1D linear arrays, a number of identical transducer elements is set in a line in one dimension (1-D) in order to produce a transducer array. The distance between the centres of two contiguous elements is called the pitch of the array, and the gap between them is known as the kerf. The linear array usually has a typical spacing of one wavelength (λ). Changing that spacing could result in a change of the resonant frequency of the transducer. When a linear array is active, only a subset of elements is in use each time for transmitting or receiving purposes. The ultrasound beam is transmitted in the vertical direction to the element surface providing a reduced active aperture than the entire transducer. Ultrasound beam focusing and steering can be achieved, if a phase delay is presented to the applied signal to each element of the transducer array. These linear arrays with phase delay control, having all the elements of the array activated grouped as one, are called phased linear arrays.

Curvilinear or circular arrays are similar to linear arrays, but the physical design of the transducer elements is curved, either in a concave or a convex structure, allowing a highly focused beam shape in the former case and a sectorial beam shape in the latter. The advantage of such arrays is a wider point of view.

Annular arrays are fabricated by implementing coaxial ring elements that are nested in each other in a circular piezoelectric element. Each one of these elements usually has equal area to keep the electrical impedance similar. Annular arrays are usually similar to curvilinear arrays controlled by dynamic phase delays to achieve an adjustable focused beam, that can focus in different depths [149].

x-D arrays are similar to linear arrays, but they utilise multiple elements in the elevation direction in order to allow both of the directions to be dynamically controlled by using phase delays. According to the symmetry, the number and the size of the separate elements in the elevation direction [150], these arrays can be classified as 1.25-D, 1.5-D and 1.75-D, where 1.5-D is the most common one.

Typically, 2D arrays have a large number of elements creating a matrix. The ultrasound beam can be fully steered in 2D giving the advantage of maximum electronic control [151]. Nevertheless, the cost is considerably higher than 1D due to the difficulties in fabrication, the electrical interconnections, and also the complex electronic control system needed.

3.4 Ultrasound standing waves

Sound waves need a physical medium of propagation in order to transfer vibrations, therefore they cannot propagate in vacuum like electromagnetic waves do. What humans interpret as sound, is actually a result of vibrating particles in a medium, due to pressure that has been applied to the medium, most common medium are air and water. For micro-channels used in acoustophoretic applications, these vibrations are formed by a voltage application at specific frequencies to a transducer that is attached to the micro-channel, by converting electrical signals to mechanical vibrations. The pressure wave created in acoustophoresis is called ultrasound in the frequency region of the order of MHz, which is not detectable by the human ear, since it exceeds the human hearing upper limit of 20 kHz. In solids the sound propagates with both longitudinal and transverse waves. Though in liquids, the direction of a sound wave is strictly longitudinal, which means adjacent particles in the medium affect each other by the

oscillating point of view, another commonly used name of this process is compression. This oscillating manner leads to a superposition process, if two longitudinal ultrasonic waves propagating in the opposite direction and have equal amplitude, a static pattern of nodes and antinodes spread throughout the whole medium can be created [152]. Therefore, there are maximum and minimum interaction locations between the longitudinal sound waves, where there is no propagation of energy. This resulting wave is called ultrasound standing wave. The equation below describes the longitudinal displacement as a function of the position and time for a transmitted wave in the positive direction:

$$y_{+}(x,t) = A\sin(kx - \omega t) \tag{3.4}$$

where A is the total amplitude of displacement of the occurred longitudinal waves, k is the wave number which is calculated by $k = 2\pi/\lambda$, x is the longitudinal position, ω is the angular frequency that equals to $\omega = 2\pi f$ and t is the time. While the expression of a transmitted wave in the opposite direction is given by the following equation:

$$y_{-}(x,t) = A\sin(kx + \omega t) \tag{3.5}$$

The superposition of the two waves forming a standing wave is given by equation (3.6). The result was produced by using the trigonometric sum-to-product identity

$$y(x,t) = y_{+}(x,t) + y_{-}(x,t) = 2A\sin(kx)\cos(\omega t) \tag{3.6}$$

which explains why particles at the nodes can be observed as motionless. The pressure variation of a plane acoustic wave travelling inside a fluid to the positive and negative x direction is given by the next equation

$$p_{\pm}(x,t) = p_{ac}\sin(\omega t \mp kx) \tag{3.7}$$

where p_{ac} is the pressure amplitude of the wave. By applying the same technique as for the extraction of equation (3.6), the superposition of the pressure variation of a standing wave is given by the next equation:

$$p(x,t) = 2p_{ac}\cos(kx)\sin(\omega t) \tag{3.8}$$

The acoustic pressure field and the longitudinal displacement of a standing wave is demonstrated in Figure 3.3

This movement of the particle towards pressure nodes or antinodes is the result of wave scattering on the acting on the surface of the particle which denotes a force in the direction of the wave propagation.

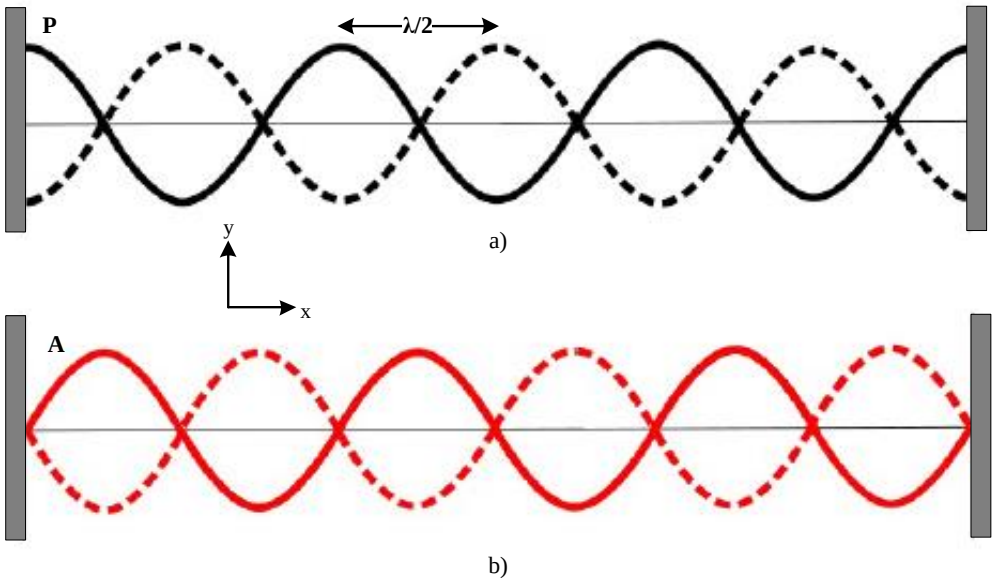

Figure 3.3 a) Acoustic pressure field and b) longitudinal displacement of a standing wave.

3.5 Ultrasound Acoustic radiation force

The acoustic radiation force has been studied for many years since it was discovered by Kundt (1868) [49] who demonstrated the effect by using cork dust in a glass tube, and King in (1934) [53] provided analytical solutions on the problem of the force on an incompressible sphere in a fluid of viscosity equal to zero, also known as superfluid, under the influence of travelling or standing waves. This study was based on the particle diameter being considerably smaller than the incident wavelength. By developing further this analytical study Yosioka and Kawasima created the solutions for compressible spheres in superfluids [153] before Gor'kov [55]. Calculations in more depth, in order to include viscosity and heat conductivity, have been performed by Doinikov [154] and Mitri [155]. Nevertheless, the effects of these factors are only significant where travelling waves are involved [56], rather than standing waves; thus for most devices developed to date, the results based on Gor'kov [55] and Yosioka and Kawasima

[153] are appropriate for calculating the forces involved, which will be explained in section 3.5.1.

There are two main forms of radiation force caused by different acoustic fields: the primary radiation forces (F_{pr}) and secondary radiation forces (F_{sr}). F_{pr} is derived by the primary ultrasound field that is introduced into the medium and drives the particles towards the pressure nodes or antinodes of the ultrasound field. F_{sr} is created due to mutual interactions between particles if they are close to each other in an ultrasound field. Hence, the values of F_{sr} are usually much smaller than those of F_{pr} [17].

3.5.1 Primary acoustic radiation force

Particles suspended inside a liquid medium under the effect of a standing acoustic wavefield are experiencing a gradient force on the direction of the acoustic pressure applied or on the opposite direction depending on the mechanical properties of the particles. With the restriction of the diameter of the particles being less than half the wavelength (λ/2) of the standing wave [153]. This gradient force acting on the particles is called primary acoustic radiation force (F_{pr}) and takes place due to pressure variations on suspended particles inside a liquid medium. More specifically, this results in a local alteration of the acoustic field in a scattering form around the surface of the particle. The motion of the particle is triggered by the pressure difference on its surface.

The primary acoustic radiation force is a function of the mechanical properties of the particle (density and compressibility) in relation with the properties of the liquid medium and also the velocity and pressure fields in the medium. The expression for the primary acoustic radiation force on a compressible sphere in an arbitrary acoustic field was given by Gorkov [55] after he extended the theory of Yosioka and Kawasima for compressible spheres. The time average acoustic radiation force is a gradient of a potential:

$$\langle F \rangle = -\nabla U \tag{3.9}$$

where U is the acoustic force potential, which is described by

$$U = V\left[\frac{b_1}{2\rho_m c_m^2}\langle p^2 \rangle - \frac{3b_2\rho_m}{4}\langle |\upsilon|^2 \rangle\right] \tag{3.10}$$

where V represents the volume of the particle, p and v is the pressure and velocity field, respectively, while ρ_m and c_m give the density and speed of sound in the medium. The compressibility factor b_1 and the density factor b_2 are represented by the following equations (3.11) and (3.12), respectively.

$$b_1 = 1 - \frac{1}{\gamma \delta^2} \tag{3.11}$$

$$b_2 = \frac{2\gamma - 2}{2\gamma + 1} \tag{3.12}$$

Where γ is the density ratio of the particle (ρ_p) and the medium (ρ_m), while δ represents the speed of sound ratio of the particle (c_p) and the medium (c_m), which are described by the following equations

$$\gamma = \frac{\rho_p}{\rho_m} \quad , \quad \delta = \frac{c_p}{c_m} \tag{3.13}$$

A strong one dimensional coupling effect at a single frequency excitation is usually observed instead of a complex 3D resonance for acoustophoretic particle manipulation. With the approximation of the F_{pr} to a single dimensional plane standing wave made by assuming that the chosen frequency supports a strong resonance field in only one direction and that the wavelength is much larger than the radius of the particle [156], then the axial component of the force F_{pr} is given by:

$$F_{pr} = 4\pi\varphi k r^3 E_{ac} \sin(2kx) \tag{3.14}$$

Where k is the wave number and is defined by

$$k = \frac{2\pi}{\lambda} \tag{3.15}$$

While r is the radius of the particle, x is the distance of the particle from the node and φ is the acoustic contrast factor which is given by the following equation

$$\varphi = \frac{5\gamma - 2}{2\gamma + 1} - \frac{1}{\gamma \delta^2} \tag{3.16}$$

The compressibility β is defined by the next equation, which shows its connection to the variables of the density and the speed of sound.

$$\beta = \frac{1}{\rho c^2} \tag{3.17}$$

By applying equations (3.13) and (3.17) into equation (3.16), the acoustic contrast factor can be rewritten as:

$$\varphi_{(\beta,\rho)} = \frac{5\rho_p - 2\rho_m}{2\rho_p + \rho_m} - \frac{\beta_p}{\beta_m} \tag{3.18}$$

While the acoustic energy density E_{ac} is given by:

$$E_{ac} = \frac{p_{ac}^2}{4\rho_m c_m^2} \tag{3.19}$$

where p_{ac} is the acoustic pressure amplitude. By combining equations (3.14), (3.15), (3.17) and (3.19), the following expression for the primary acoustic radiation force is derived

$$F_{pr} = \frac{2\pi^2}{\lambda} r^3 p_{ac}^2 \beta_m \varphi_{(\beta,\rho)} \sin\left(\frac{4\pi x}{\lambda}\right) \tag{3.20}$$

From equation (3.20), it is readily derived that the primary acoustic radiation force is proportional to the cube of the particle radius and is proportional to the applied frequency. Furthermore, the magnitude and the direction of the F_{pr} is also dependant on the acoustic contrast factor, which changes regarding the density and the compressibility of the particle and the surrounding medium. As an example a polystyrene particle suspended in water is defined by less compressibility than the medium and is denser than the medium. By using equation (3.16), it is concluded that the contrast factor has a positive sign and as a result the particle will move to the nearest pressure node. Compared to an air bubble that has higher compressibility

and is less dense than the surrounding medium (e.g. water). This results in a negative sign of the contrast factor making the air bubble move towards the nearest antinode. Figure 3.4 illustrates the acoustic radiation force and the pressure field at the resonance frequency in a standing cavity that fits one node of the standing wave. In the same graph it can be seen that the predicted movement of particles depends on not only the contrast factor, but also the force vector.

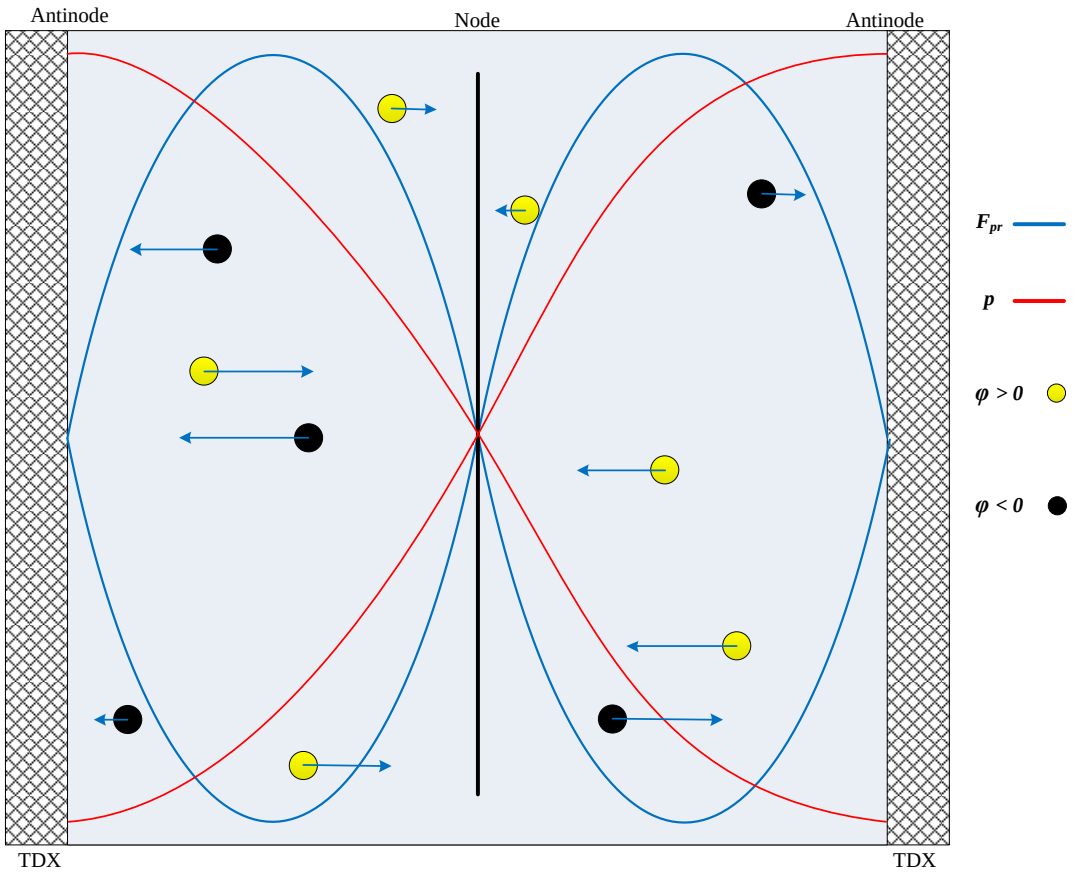

Figure 3.4 Representation of the acoustic force and the pressure field in a standing cavity under the effect of the resonance frequency of two opposing transducers. Motion of particles regarding the sign of the acoustic contrast factor.

The maximum pressure is located at the antinodes while the minimum pressure is positioned at the nodes. The F_{pr} acting on a particle located on an antinode is equal to zero and reaches its maximum value at the equidistant point between the pressure node and antinode.

The theory described by King, Yosioka and Kawasima, and Gor'kov is based on inviscid fluids. Doinikov took into consideration the fluid viscosity and the heat conduction. He found that in standing waves the acoustic radiation forces acting on spheres do not strongly depend on the viscosity of the fluid, but the forces in propagating waves are usually higher by orders of

magnitude than the previous theories based on inviscid fluids. Furthermore, he discovered that the forces acting on compressible spheres in fluids that are heat conducted are negligible for plane standing waves[157].

3.5.2 Secondary acoustic radiation force

When multiple particles are found near to each other in the acoustic field, the scattered acoustic field from the particles will acoustically generate forces between the particles themselves. These particle against particle interaction is known as secondary radiation forces (F_{sr}) [158], also called Bjerknes forces [159]. The forces are dependent on the distance between the particles. Therefore, the forces are usually negligible until the particles are in neighbouring proximity, e.g. after particles are aligned in the pressure nodal plane by the effect of the primary radiation forces.

Weiser et al. [160] followed the experimental studies by Crum [161] and calculated the secondary radiation forces between two identical and compressible spheres, under the effect of a plane acoustic stranding wave, the expression for the F_{sr} [158] is given by the following equation:

$$\left\langle F_{sr} \right\rangle = 2\pi r^3 \left(\frac{\left(\rho_p - \rho_m\right)^2 \left(3\cos^2\theta - 1\right)}{6\rho_m d^4} \upsilon^2(x) - \frac{\omega^2 \rho_m \left(\beta_p - \beta_m\right)}{9d^2} p^2(x) \right) \tag{3.21}$$

where r is the radius of the sphere, ρ_p and ρ_m are the density of the particles and the medium, respectively; moreover the variable θ expresses the angle between the direction of the propagating sound wave and the imaginary line connecting the centres of the spheres, d describes the distance between the two spheres, $\upsilon(x)$ is the velocity of the undisturbed field at the exact positions of the particles, ω is the angular frequency, β_p and β_m are the compressibility of the particles and the medium respectively, and $p(x)$ defines the pressure of the undisturbed field at the exact position of the particles.

The necessary condition to make the secondary forces significant is that the distance between the particles should be very small and the particles themselves should be much smaller than the propagating acoustic wavelength. In equation (3.21) an assumption was made, that a standing wave exists in the x direction.

The secondary force is dependent on the orientation of the particles with respect to the direction of the wave propagation, thus the force can be attractive if the sign is negative or repellent if the sign is positive. By analysing the first term of the equation (3.21), it can be seen that it has no effect at particles on the pressure antinodes of the standing wave as it disappears from the equation. On the other hand, the second term vanishes from the equation at the pressure nodal plane and has no effect on particles that find themselves at the pressure nodes. If the value of the angle θ is equal to 0, then the first part of the equation becomes positive, thus the direction follows a repulsive force impact. If the direction of the wave propagation is perpendicular to the aligned particles meaning θ=90º then the force becomes negative, which means it has an attractive impact to the aligned particles as shown in Figure 3.5. The second part of the equation is free of any dependency from the value of the angle θ and represents attractive force, meaning the particles with negative contrast factor will always be attracted to each other.

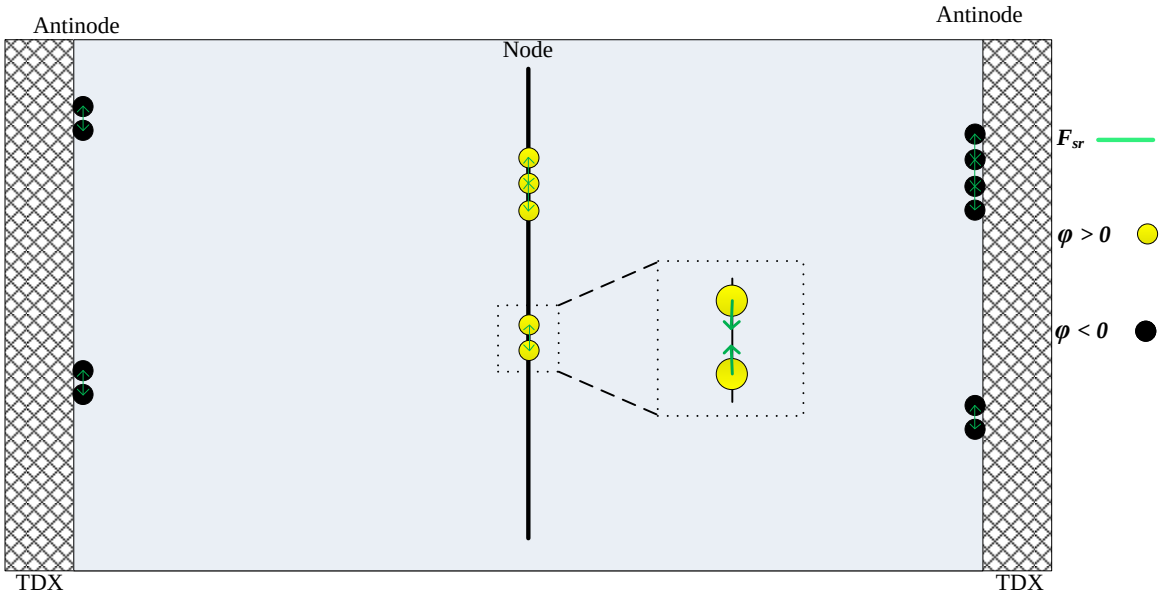

Figure 3.5 Representation of the secondary forces in a standing cavity, motion of particles depending on their position on the acoustic field.

3.6 Stokes' drag force

In a low Reynolds number (*Re*) region, in microfluidics field, the particles in a fluid will move in a controlled manner due to the laminar flow. The viscous force is higher than the inertial forces. When trying to manipulate particles to reach the middle of a microfluidic channel via ultrasound acoustic standing waves, at the beginning of excitation of the transducers the friction force is equal to zero while the acoustic radiation force (F_{rad}) accelerates the particle. The

frictional force is also known as the Stokes' drag force F_d, which is described by the Stokes' law summarised by the following equation:

$$F_d = 6\pi\eta r\upsilon \tag{3.20}$$

where η is the dynamic viscosity of the fluid, r is the particle radius, and υ is the velocity of the particles. The Stokes' law denotes that when the particle velocity increases, the drag force increases in a linearly manner, and the linear condition applies also on the size of the particle. At a very short time of the order of ms, the particle accelerates and reaches a velocity where the condition $F_d = F_{pr}$ occurs. Right afterwards, the particle keeps moving at this constant velocity. As a result, if the velocity of the particle is known and with a given size, it is possible to calculate the force output.

The equation of the drag force is based on the assumptions that the particles are completely spherical, the fluid that they are inside is incompressible, the flow in the channel is laminar and the flow dynamic is not disturbed by any interaction between particles that may occur. The streaming lines of a laminar fluid flow and the forces acting on a particle are illustrated in Figure 3.6.

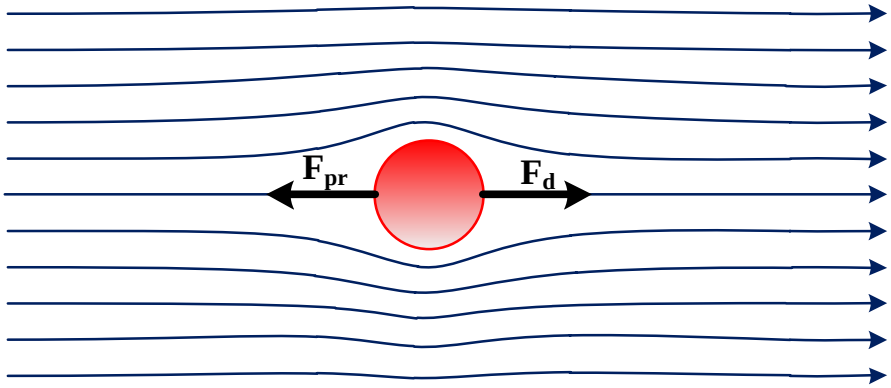

Figure 3.6 Stokes' Law schematic representation of acting forces on a particle.

3.7 Acoustic streaming

The size of the particles influences their acoustophoretic movement when inside a microfluidic channel. Particles of diameter larger than 1.5 μm can move towards the pressure nodes and antinodes under the effect of the primary acoustic radiation forces applied. On the other hand,

small particles of diameter less than 1.5 μm can be exposed to fluid vortices that were acoustically generated in the bulk liquid medium. The absorption of acoustic energy inside the medium associates these vortices with the acoustic streaming. The primary acoustic radiation force applied on small particles, cannot exceed the drag force of the induced streaming, thus small particles cannot follow the large particles to the nodes or antinodes. Acoustic streaming can be mostly identified by two forms, boundary layer driven streaming and the Eckart streaming.

The boundary layer driven streaming is distinguishable in two subcategories. The first one is the outer layer streaming, in which Lord Rayleigh investigated the streaming induced by standing waves between parallel plane walls [162]. The second one is the inner layer streaming or Schlichting streaming, which describes a more viscous fluid layer than the bulk fluid due to a proximity to a bounding surface. Acoustic energy dissipates into the inner boundary layer and spawns vortices which subsequently generate bulk fluid vortices in the outer boundary layer. This type of streaming is widely seen in microfluidic resonators and is especially pronounced in thin microfluidic channels where the influence of the thick inner boundary layer is stronger. The outer layer streaming can be enhanced if the aspect ratio of the channel is decreased or it can be diminished if the aspect ratio of the channel is increased. In a laminar flow regime streaming can be used to mix fluids [163]. Induced streaming in a microfluidic system can also be an active means for particle separation [164]. The maximum fluid velocity of the fluid vortices is located near the top and bottom wall of the resonator while it is decaying when approaching the centre of the vortex. Figure 3.7 shows a schematic representation of inner boundary layer streaming layer and outer (Rayleigh) streaming vortices in a microfluidic channel that fits one standing wave propagating towards the x direction.

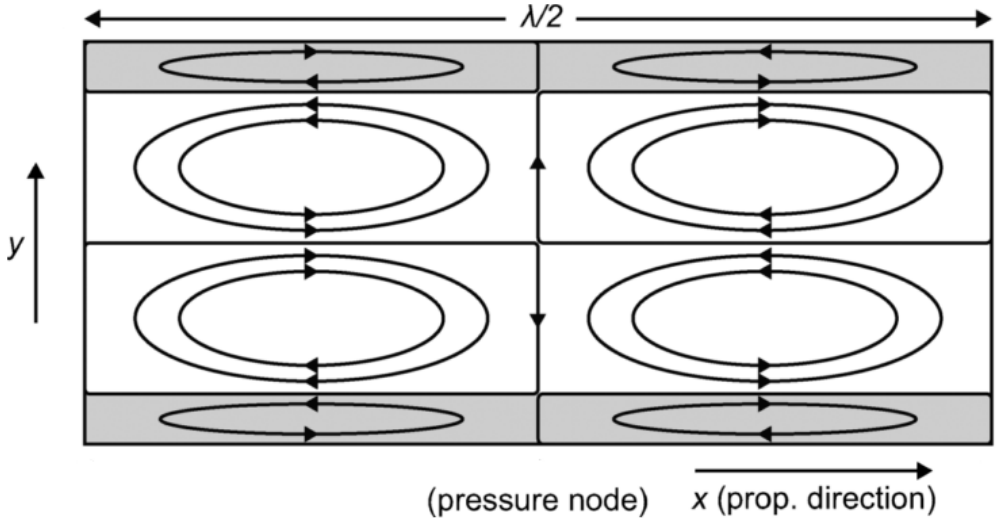

Figure 3.7 Schematic representation of inner boundary layer streaming layer and outer (Rayleigh) streaming vortices in a channel with a standing wave propagating along x direction. The pressure node is located at x = 0, which is the plane in which small particles particles and cells would be trapped by acoustic radiation forces. Image reproduced from [165].

Eckart streaming or quartz wind is the result of acoustic energy dissipation in the bulk of a fluid when a transmitted acoustic wave travels through it. This effect takes place in standing waves at high frequency where the channel dimensions are large, as this supports sufficient wave attenuation in the bulk liquid. In microfluidic devices, Eckart streaming is not dominant over other acoustic streaming forms, the main reason is that the boundary layer effects are more powerful than the bulk effects at microscale dimensions [165].

3.8 Surface Acoustic Wave (SAW) devices

3.8.1 Wave propagation in a SAW device

Surface acoustic waves (SAW) are mechanical waves that propagate along the surface of a medium. Lord Rayleigh was the first to introduce the SAWs, who dealt with the research of surface acoustic propagation along the surface of a semi-infinite isotropic medium [166]. Thus, SAWs are also named as Rayleigh waves. Surface acoustic waves are formed due to a combination of waves, a longitudinal or compressional wave and a shear or transversal wave which can have a normal displacement component to a boundary. Figure 3.8 illustrates the wave propagation of a longitudinal wave and a transverse wave that construct a Rayleigh wave.

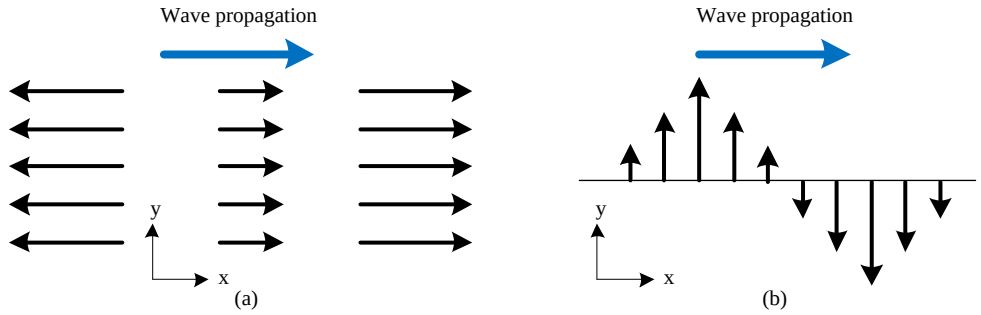

Figure 3.8 Schematic representation of wave propagation (a) of a longitudinal wave and (b) of a transverse wave at the positive x direction.

Figure 3.9 demonstrates the surface acoustic wave propagation through a medium, highlighting the particle motion under the effect of the travelling wave over time. Small cubes in the figure represent the particles in the medium.

The surface acoustic waves propagate along the surface of the medium with elliptical particle motion that comprises of both the parallel and the perpendicular direction of propagation in the plane of the raypath. The amplitude of the particle displacement depends on the position depthwise and decreases exponentially in the direction below the material surface, resulting in almost no motion of particles at deeper than one acoustic wavelength. The density of the energy of a SAW is very high and SAW devices are highly sensitive to changes in the surface and environment [167], since most of the acoustic wave energy is restrained within one wavelength normal to the substrate surface.

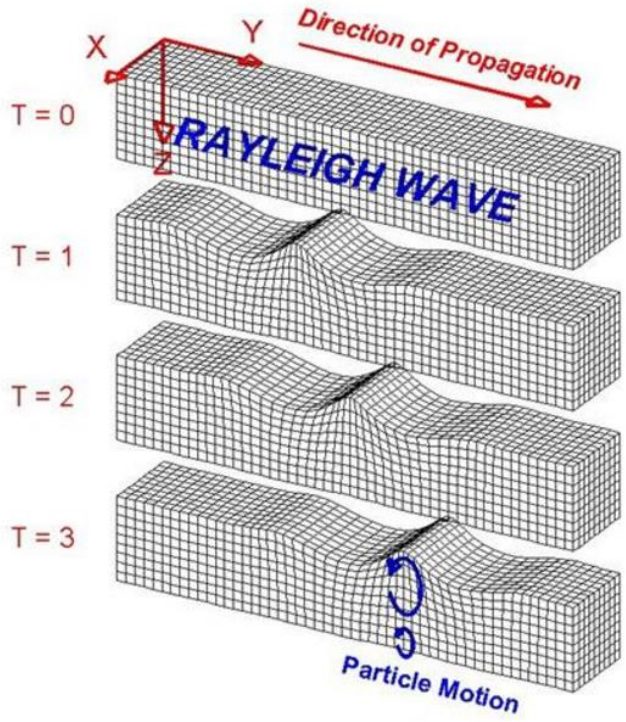

Figure 3.9 Schematic representation of a Rayleigh wave propagation through a medium, where T denotes the time [173].

SAW devices have the advantage of less energy dissipation in the microfluidic domain due to the inherently confined SAW energy to the substrate surface before reaching the channel. Moreover, SAW is capable of very high frequency content and does not need high resonant constructions such as a high resonance chamber for providing acoustic forces [168]. Thus, SAW propagation techniques are more widely implemented for acoustic-based microfluidic devices compared to the bulk acoustic wave (BAW).

3.8.2 Materials for surface acoustic wave (SAW) devices

SAW based devices are commonly created by implementing interdigitated electrodes on top of a piezoelectric material. The piezoelectric effect is derived by solid material in order to produce an electric charge when it is subjected to a mechanical pressure, and vice versa. Some of the piezoelectric materials commonly used for the generation of SAW are quartz (SiO_2), lithium niobate ($LiNbO_3$), and lithium tantalate ($LiTaO_3$). Table 3.2 summarises the properties of wave velocity (υ_{sw}) for these materials depending on the direction of the cut and the propagation direction. The choice of the piezoelectric material and cut is critical and is subjective to two main aspects. The first consideration is the beam steering. In an anisotropic solid, the surface acoustic wave velocity depends on the direction of propagation. The second field of interest is

to determine how effective the piezoelectric conversion of the electric signal to mechanical energy is, thus a strong piezoelectric electromechanical coupling coefficient k^2 is required.

Table 3.2 Dependency of the wave velocity and electromechanical coefficient on the orientation of the cut of different materials

Material	Cut Orientation	Direction of propagation	Velocity of wave (m/s)	k^2(%)
Quartz	ST	X	3158	0.14
$LiNbO_3$	128º Y	X	3980	5.5
	41º Y	X	4792	17.2
	Y	Z	3488	4.9
$LiTaO_3$	X	112 Y	3290	0.75
	36º Y	X	4160	5
	42º Y	X	4022	7.6

Quartz has very low electromechanical coupling coefficient (k^2). This low k^2 of quartz limits the relative bandwidth. The values of the coefficient k^2 of lithium niobate and lithium tantalate are much larger than that of quartz, thus these materials are more appropriate for low loss and wide band applications. As a drawback though, those two materials have a low thermal tolerance, making them thermally fragile. Furthermore, the optical transparency of $LiNbO_3$ can be advantageous in combining acoustic and optical particle manipulation into one hybrid system. In this work, $LiNbO_3$ has been chosen as the material of the substrate for the SAW device due to all the aforementioned benefits.

4. Dynamic Acoustic Field

4.1 Principle of operation

In this chapter a novel technique for manipulating particles and cells is described. The basic principle of operation of the Dynamic Acoustic Field (DAF) is described in the following section. When two opposing transducers (TDXs) are excited two travelling waves are transmitted from opposite directions which allow standing waves to be formed. As described in equation (3.20) (see Section 3.5.1), a linear pattern of nodes and antinodes is formed. Figure 4.1 shows a schematic of what was described above. The total number N of the nodes that can fit in between the two transducers is equal to their distance χ divided by half of the wavelength $\lambda/2$ of the excited signal, $N = \chi / \lambda/2$. Particles and cells in the media will agglomerate at the desired area of operation, under the effect of the acoustic pressure applying forces. They will accumulate in the nodes if the acoustic contrast factor (φ) equation (3.18) (see Section 3.5.1) is higher than 0 or in the antinodes if the acoustic contrast factor is less than 0.

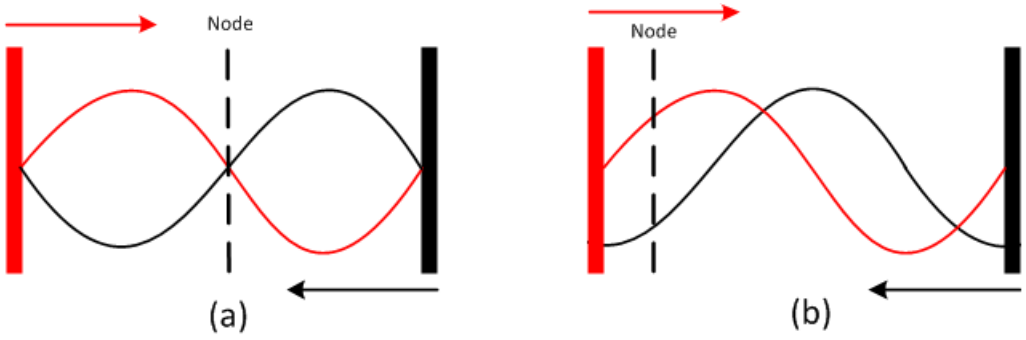

Figure 4.1 Schematic illustration of two opposing transducers (a) with 0° phase and (b) with 180° phase between them showing their wave excitation forming a standing wave.

The Dynamic acoustic field takes advantage of the fact that the phase of one of the transducers can be changed with respect to the other, which translates this linear pattern of nodes and antinodes in the direction of the chosen phase shift, and consequently the particles or cells will be transported along with translation of the nodes. The phase shift described above is shown in Figure 4.2, where the phase of one of the transducers is shifted from 0° to 360°, which describes a full cycle, for the duration of time t_{ramp} and stays there for the duration of time t_{rest} and this pattern is repeated for several cycles.

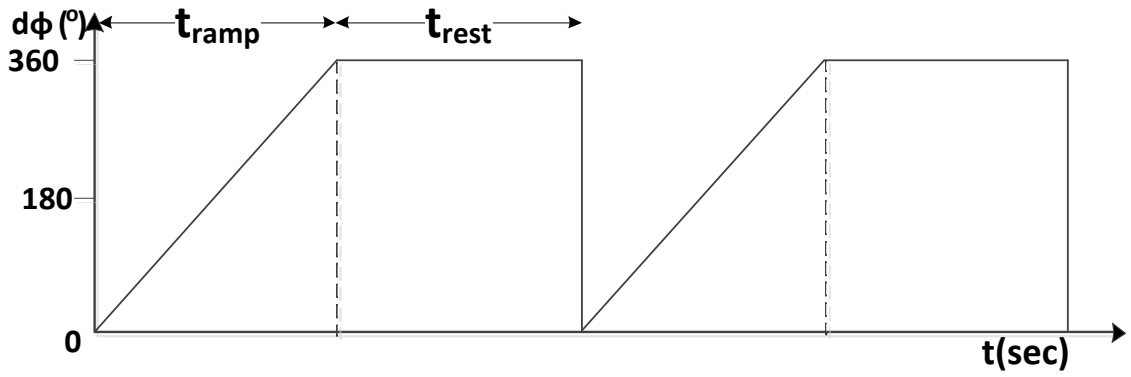

Figure 4.2 Schematic representation of the principle of operation of the DAF method.

4.2 Acoustic separation simulations

4.2.1 Acoustic separation by size

In order to predict the behaviour of the particles under the effect of the dynamic acoustic field a numerical method has been used to understand the particle separation mechanism. The code was developed in Visual Basic during the preliminary work by A. Bernassau. The particle behaviour was modelled under different particle properties (size and density), dynamic acoustic field, liquid viscosity and liquid flow. The program is taking into account the acting forces on the particles by calculating the primary acoustic force F_{pr}, equation (3.20), and viscous drag force F_d, equation (3.22) as a function of time (see Section 3.6).

The equation of motion of a particle labelled by its position *r(t)* is given by

$$\frac{\partial^2 r}{\partial t^2} = \frac{\partial \upsilon}{\partial t} = \frac{F_{tot}(r,\upsilon,t)}{m} = a(r,\upsilon,t) \tag{4.1}$$

where F_{tot} is the sum of F_{pr} and F_d, with m describing the mass of the particle, a is the acceleration as a function of particle position r and the relative particle velocity υ at a time t.

These motion equations were integrated step by step using the Verlet algorithm [169][170], equations (4.2) and (4.3) to produce the expected movement of the particles.

$$r(t+\Delta t) = 2r(t) - r(t-\Delta t) + a(t)\Delta t^2 \tag{4.2}$$

$$\upsilon(t) = \frac{r(t+\Delta t) - r(t-\Delta t)}{2\Delta t} \tag{4.3}$$

Where r is the particle position, υ its velocity and Δt the integration time step.

The computer program can simulate the movement of particles among different types of particles in terms of their radius and density. Figure 4.3 denotes the predicted particle separation of two classes of particles with different sizes, where smaller particles of 6 μm diameter are presented in red colour and larger particles of 10μm diameter are shown in green colour. The two populations were separated during the activation of the dynamic acoustic field after the duration of one full cycle. The 10 μm particles were transported to the next node along with the translation of the nodes. For this specific example t_{ramp} and t_{rest} were selected equal to 5 seconds providing the ratio between them (t_{ramp} /t_{rest}) to be equal to 1.

Another simulation has been carried out in order to verify the sorting capability of the proposed method regarding the size of the particles or cells. This was done by constructing the primary acoustic radiation force equation in Matlab, the source code is given in Appendix A. As can be seen from the result in Figure 4.4, it can be easily derived that larger particles experience higher acoustic radiation forces acting on them.

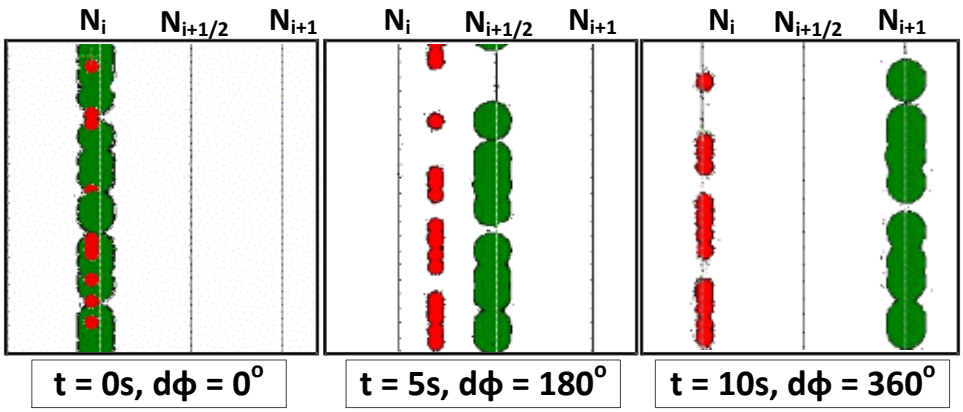

Figure 4.3 Simulation of particle separation by size using the DAF method with green colour representing the 10 μm diameter particles and with red colour the 6 μm diameter particles [177].

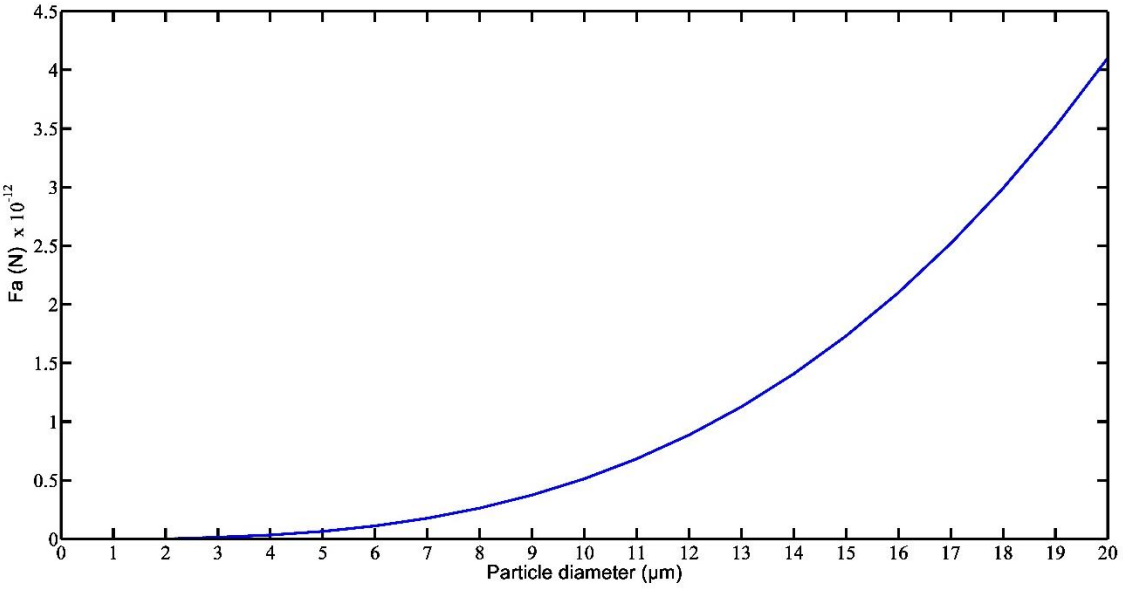

Figure 4.4 Matlab simulation of primary acoustic force acting on particles versus their size.

4.2.2 Acoustic separation by density

The simulation for the particle density separation capability was completed in the same way as the one described for the acoustic separation by size. This means that the same computer program was used as before to produce the graph shown in Figure 4.5, where the size of all the particles used was kept the same at 10 μm but the density of the two populations was different. For this specific simulation the two populations were selected to have the density of polystyrene particles at ρ = 1.05 g/cm^3 and iron-oxide filled beads at ρ = 1.41 g/cm^3.

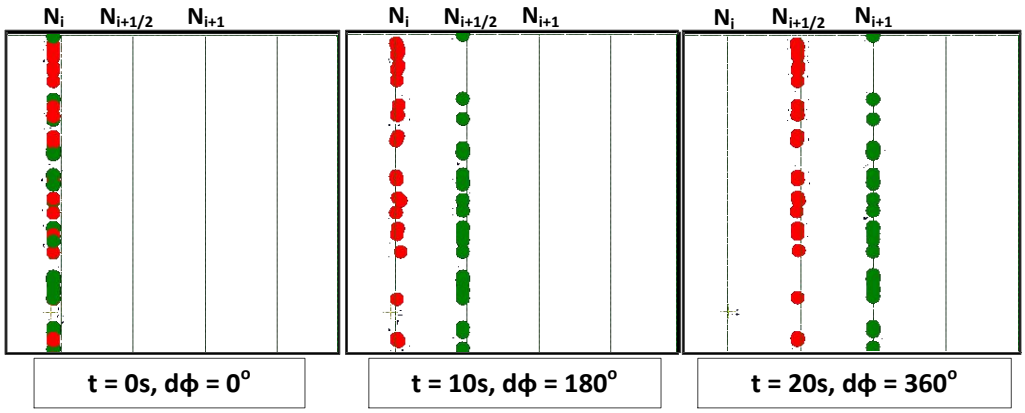

Figure 4.5 Density separation simulation for particles of density ρ =1.41g/cm^3 (green colour) and ρ =1.05 g/cm^3 (red colour).

As it can be concluded by the Figures 4.3 and 4.5, the total time needed of a complete cycle of the density separation simulation is noticeably increased in comparison with the size simulation. It can also be inferred that the sorting depending on the density is going to be much more difficult than the size sorting since particles do not have great difference between their densities, while cells experience even less difference in terms of density. Again, a Matlab simulation was carried out in order to verify and strengthen the hypothesis of sorting regarding the density of the particles. Figure 4.6 demonstrates the result of that simulation showing the change of the primary acoustic radiation force in comparison with the density change.

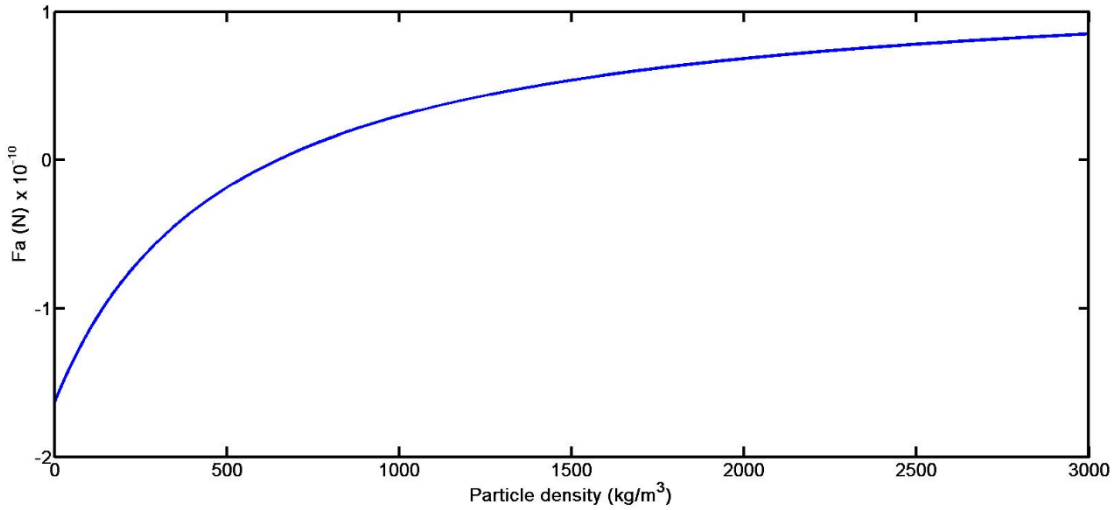

Figure 4.6 Simulation of the acoustic radiation force versus the particle density change.

4.3 Control Labview

In order to communicate with the signal generator, a Labview code was produced to control two channels of the signal generator simultaneously. Both the signals derived from the channels can be manipulated to have the same frequency, same amplitude and be capable of changing the phase between the two channels. A Labview code was implemented in order to rapidly change the phase between the transducers. As an example, a phase shift of 40^{o} was applied to one of the transducers every 0.5 s while keeping the other transducer at its initial phase. The Labview program is also tuneable to manipulate the signal generator to run different number of cycles depending on the experiment's requirement. There is a controller called *Rep* which sets how many times the cycle will be repeated.

An important factor is how much time (t_{rest}) the system will stay at the end of each run at 359º, that factor is given by the sum of the t_1 and the t_{delay} controllers, which in this example is t_{rest} = t_1+ t_{delay} =0.64s+1s=1.64sec. Thus, the total time to complete one full cycle is equal to the sum of t_{rest} and t_{ramp}, where t_{ramp} is given by the equation (4.3)

$$t_{ramp} = \frac{360^o}{d\varphi} \cdot t_1 \tag{4.3}$$

which corresponds to the time until no increment will take place. In this case the total time was T_{tot} =1.64s+6.4s=8.04sec. What has been explained above is illustrated in Figure 4.7.

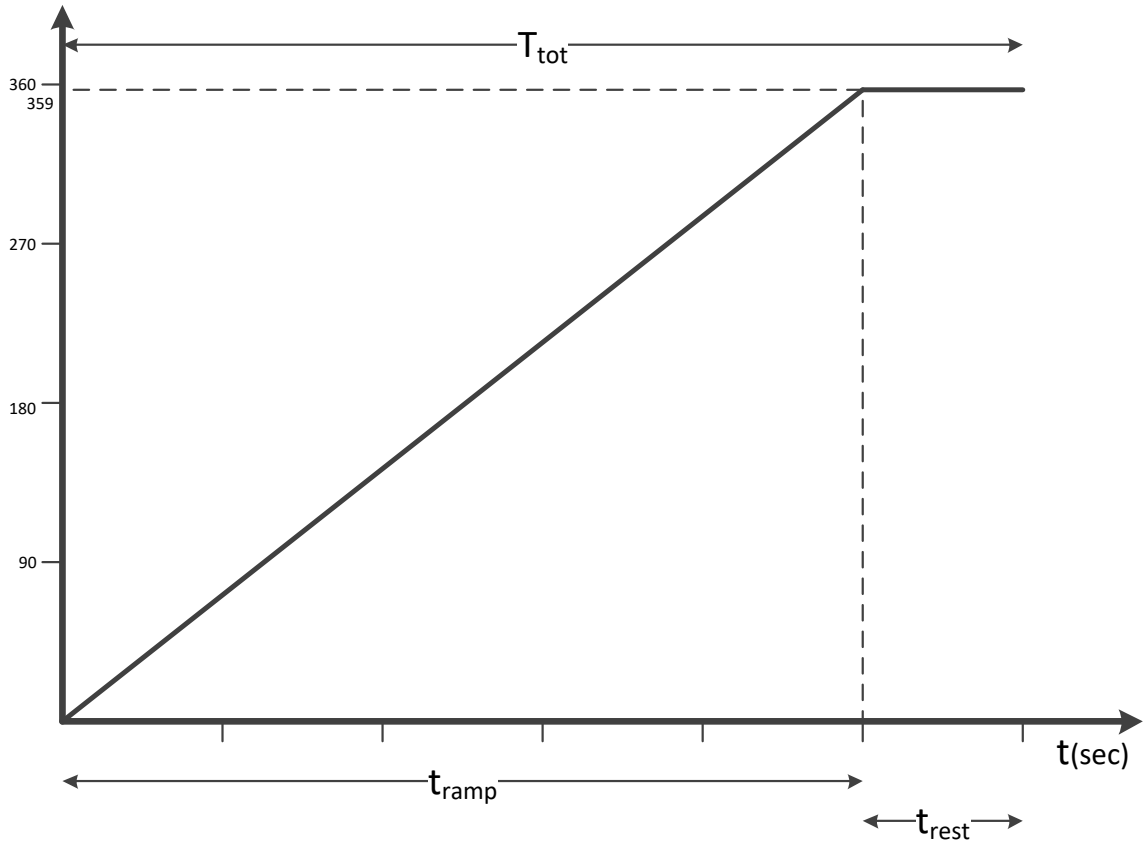

Figure 4.7 Total time for a complete cycle.

4.4 Ultrasound devices using PZT plates

As a preliminary work an ultrasonic device for micro-patterning and precision manipulation of micrometre-scale particles has been demonstrated by Bernassau et.al [27]. The device was constructed by using eight piezoelectric transducers shaped into an octagonal cavity. By exciting different combinations of transducers simultaneously, and by controlling the phase delay between them, different acoustic landscapes can be created to pattern micro-particles into lines, squares, and more complex geometrical shapes. When operated with all eight transducers simultaneously, the device can manipulate the two dimensional acoustic pressure gradient; thus it is capable of positioning and translating a single tweezing zone to different locations on a surface in a precise and programmable manner. For the purpose of this application only one set of opposing transducers is required [171].

4.4.1 Fabrication of ultrasound devices using PZT plates

For the fabrication of the BAW device, lead zirconate titanate (PZT) plates were used with a matching layer in the front face of the piezoelectric material. The matching layer was used in order to achieve matching between the acoustic impedance of the piezoceramic with the medium that the wave is going to be propagated, resulting to a much higher energy transfer through the excitation of the transducer. On the other hand a backing layer that most of the conventional BAW devices use, was not necessary for the purposes of this work, since the matching layer's thickness was optimised using one-dimensional transmission line model as described by C. Courtney et al. [82] to minimise the reflection of the occurrence waves. The last component needed in order to have a single element ultrasonic transducer was the electrical connection that will drive the signal from the source. In Figure 4.8a is shown a transducer before the matching layer was cut to the appropriate size and Figure 4.8b shows a fully fabricated single element transducer after all the described components were added.

Figure 4.8 Fabrication of transducer a) before and b) after cutting off the excess of alumina layer.

In particular for the fabrication of the BAW device, it was used the PZT with part number NCE51 Noliac piezo ceramic plates with a size of 0.5cm x 0.5cm. Then a matching layer of aluminium oxide (Al_2O_3) or alumina loaded epoxy was applied on the front side of the ceramic. The ratio used was 10% of alumina inside the epoxy called EpoFix. The technique for achieving this, was by moulding around the area of the ceramic plate with Teflon blocks and then add the alumina loaded epoxy in liquid form. A pre-stage of degassing was necessary in order to remove any air bubbles that were produced during the mixing of the epoxy solution and then wait until it was dry to solid form. The next step was to cut the alumina layer into the desired thickness.

Following that stage, the impedance of all the fabricated transducers was measured in the network analyser and only pairs of matched transducers regarding their frequency and impedance were bonded on a flexible kapton ribbon. Each pair was facing each other and a final shape of an octagon device was formed. Then, this octagon shaped flexible ribbon was mounted in between two transparent thick pvc parts, one part used as a base and one as a top fixative with a hole. The hole was made in order to introduce the medium containing the particles or cells needed in each experiment. Then, this whole system was glued on top of a PCB that was designed for having 8 isolated pins for each transducer. After soldering each side of the transducers to the correct pin, the SMA connectors were soldered in each output. Figure 4.9 illustrates a fully fabricated octagon device.

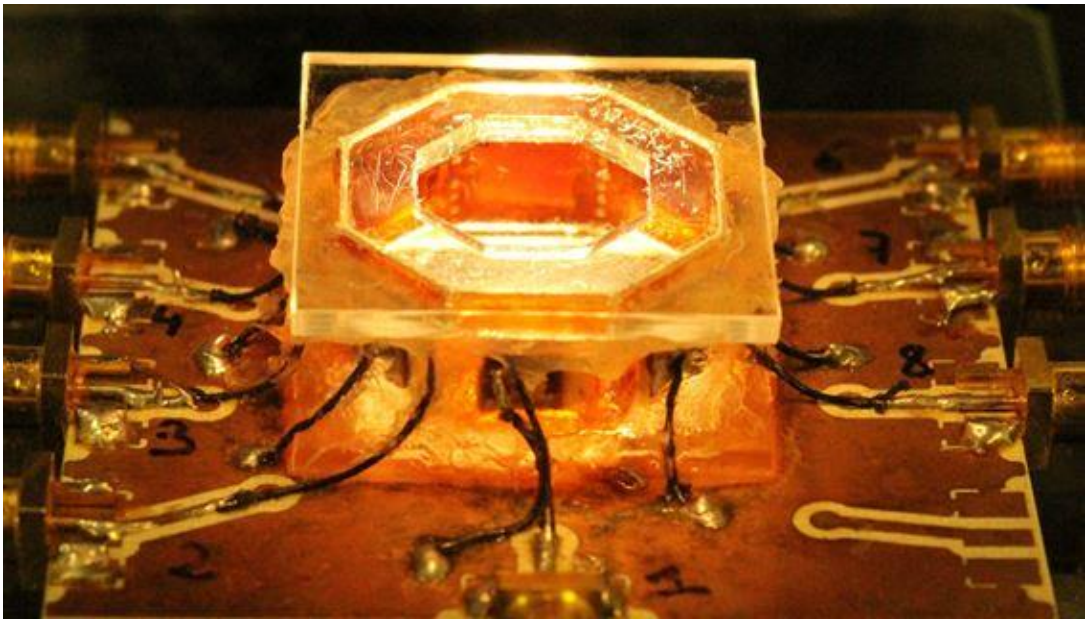

Figure 4.9 Fully fabricated octagon device using PZT plates.

4.4.2 Characterisation of BAW devices

For the characterisation of each PZT transducer the network analyser of Agilent technologies E5071B was used. By measuring the SnP parameters on the network analyser the impedance and the frequency of each transducer can be obtained. Thus, by matching those characteristics between two transducers, it can be achieved a perfectly matched pair of transducers. By utilising this pair into the device and by facing each other, it provides perfect standing waves in the distance between them and also a constant period between each standing wave. In the following image on Figure 4.10 an example of a S11- parameter measurement taken from the network analyser is demonstrated. The S11-parameter gives information on the reflection coefficient, meaning the fraction of the electric signal reflected back to the network analyser. A sharp dip in the reflection spectrum around the expected frequency range was used to find the exact resonant frequency of each transducer. In order to determine which transducers have matched resonant frequencies and impedances, the measurements were analysed by using the software Wincal, which provided a Smith chart, a frequency response and the impedance of the transducers, an example of this analysis for a pair of transducers is shown in Figure 4.11. The Smith chart is an alternative representation of the scattering parameter S11 which is plotted on the complex reflection coefficient plane in two dimensions and is scaled in normalised impedance.

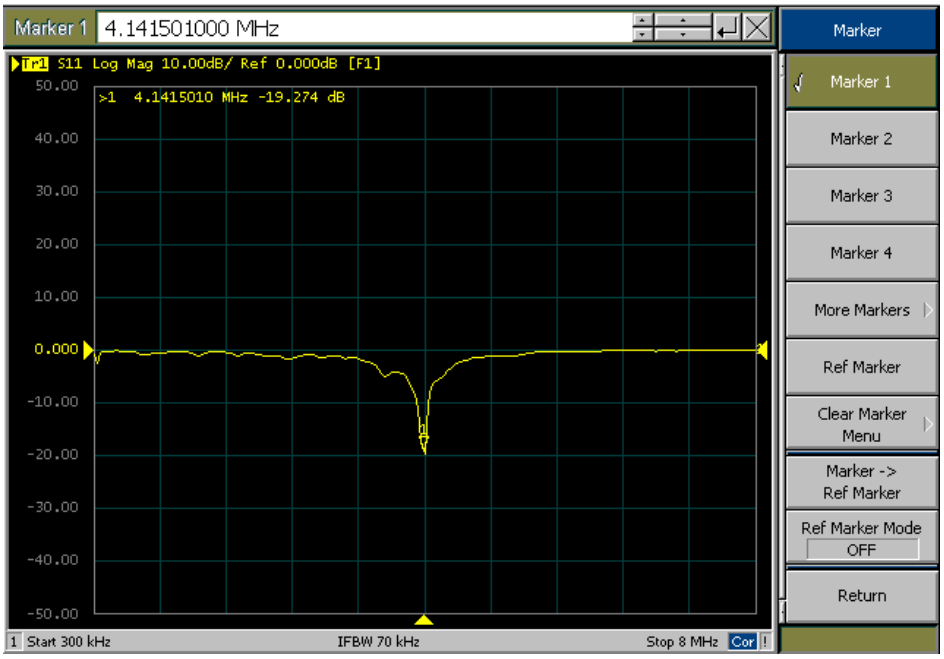

Figure 4.10 Image of the network analyser of a PZT plate transducer.

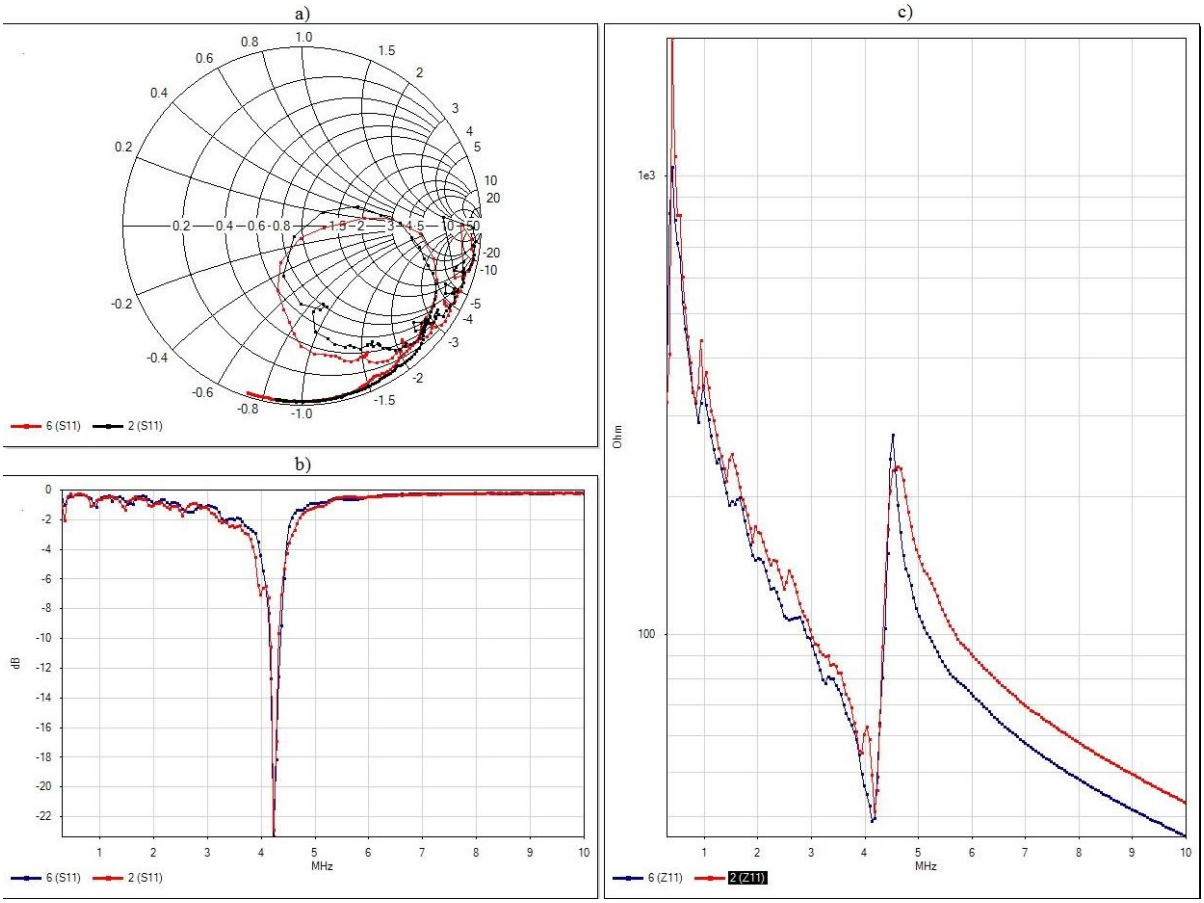

Figure 4.11 Wincal software showing the comparison of S11 parameters of two transducers under the form of a) Smith chart b) frequency response and c) impedance spectrum.

As it can be observed from the measurements analysis shown in Figure 4.11, those two transducers depicted have a great match regarding their frequency response and their impedance output, which is readily obtained from the Smith chart Figure 4.11a, but also from the graph showing the frequency response in Figure 4.11b that is almost identical for those two transducers. One more aspect of the excellent matching of those two transducers is depicted on the graph of Figure 4.11c showing the impedance versus the input resistance of each transducer, which as can be see is almost identical in the area of frequency of operation.

4.5 Ultrasound Surface Acoustic Wave (SAW) devices

4.5.1 Fabrication of ultrasound SAW devices

An ultrasound SAW device can be fabricated using several techniques and materials as described in section 2.6. In this work Lithium Niobate ($LiNbO_3$) was used as a substrate with high piezoelectric properties, in order to achieve a very long IDT aperture for accommodating a throughput microfluidic channel for particle and cell sorting. More specifically, a double sided polished black $LiNbO_3$ at 127.86^o Y- cut (The Roditi International Corporation Ltd, England) was used. The first step of the fabrication process was to dice the 3-inch wafer into 6 pieces with the desirable dimensions of (3.7 by 2.5) cm for hosting the designed IDTs. Since $LiNBO_3$ wafer is very sensitive while getting cut, a special blade is required, also a small layer of resist on the top side was spun to avoid any cracks during this procedure. The size of the effective area of each transducer (IDT aperture) was 1.5 cm and the PDMS microfluidic channel that was going to be placed on top of the substrate had a full length of 2.5 cm, including inlets and outlets. Thus, the best ratio between the 3-inch wafer and the area covered by each device was chosen to be six pieces per wafer. The design of the IDTs was completed by using the computer aided design (CAD) software L-Edit (Tanner EDA). Figure 4.12 shows the comparison between the size of full wafer and the size required for a SAW device taken from L-edit.

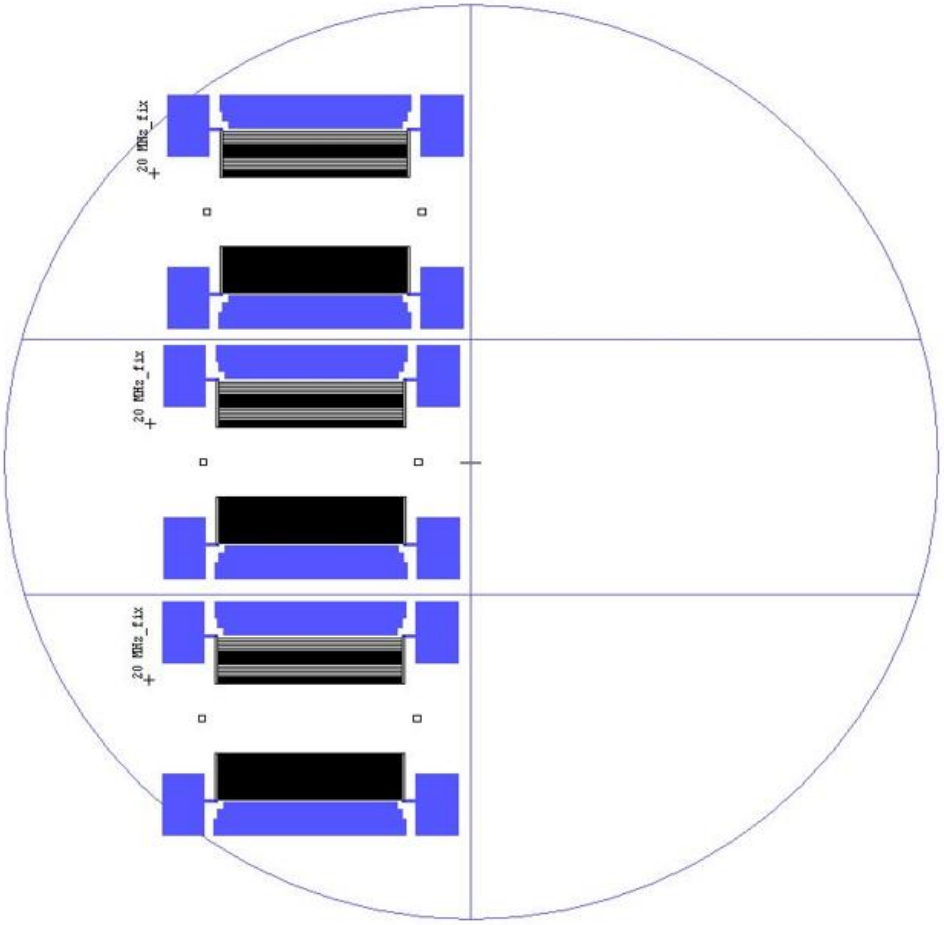

Figure 4.12 L-edit capture of a 3-inch wafer deciding the size dicing.

Each transducer was constructed of 20 fingers with equal distance spacing between each finger. The distance of each finger was determined by the desired frequency of operation of each transducer. The following equation is showing the dependency of the frequency to the size of the fingers if the acoustic velocity transmitted on the $LiNbO_3$ substrate on a given direction is considered as constant, $f = \upsilon_{SAW} / \lambda_{SAW}$, where f is the frequency of operation, υ_{SAW} is the velocity of the sound on the substrate on a given direction and λ_{SAW} is the wavelength of the SAW.

By choosing the finger width and the finger pitch to be equal, the connection between the finger width (w_{finger}) and the SAW wavelength is given by the following equation, $w_{finger} = \lambda_{SAW} / 4$. As a result, given that the velocity of the acoustic wave in $LiNbO_3$ in the direction of the x axis is equal to 3990 μm/sec [172], then the width of each IDT finger for achieving a frequency of 20 MHz should be equal to 49.5 μm. Figure 4.13 illustrates the aforementioned parameters on an IDT.

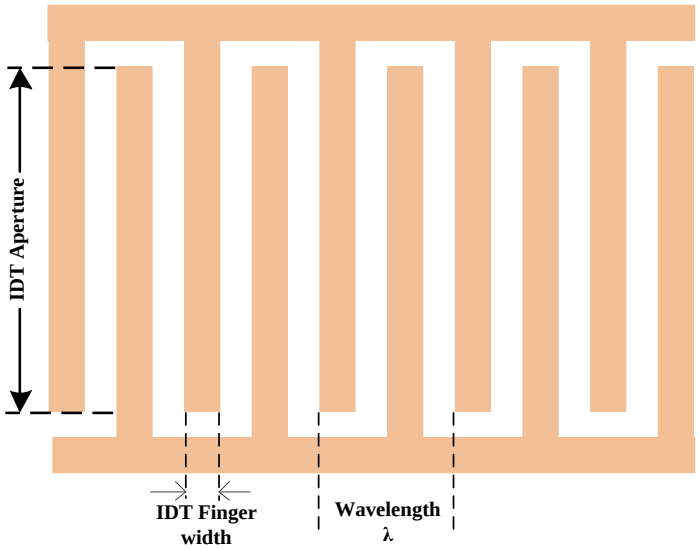

Figure 4.13 Representation of an interdigitated transducer displaying the parameters of interest.

The actual frequency of the fabricated transducer needs to be measured, due to a lot of factors that can affect the actual frequency, such us the alignment of the written pattern on the substrate and the precision of the cut of the $LiNbO_3$ provided. This measurement of the actual frequency was equal to 19.77 MHz which is very close to the expected 20 MHz. The conventional bidirectional IDT may not be the most efficient, due to the wave propagation in two opposite directions with half of the acoustic energy wasted. The simplest way to gain some energy is to reflect back some of the waves by using a reflector IDT [173]. An example of the design of a pair of transducers with reflectors facing each other is shown in Figure 4.14 the picture was taken from the L-edit file.

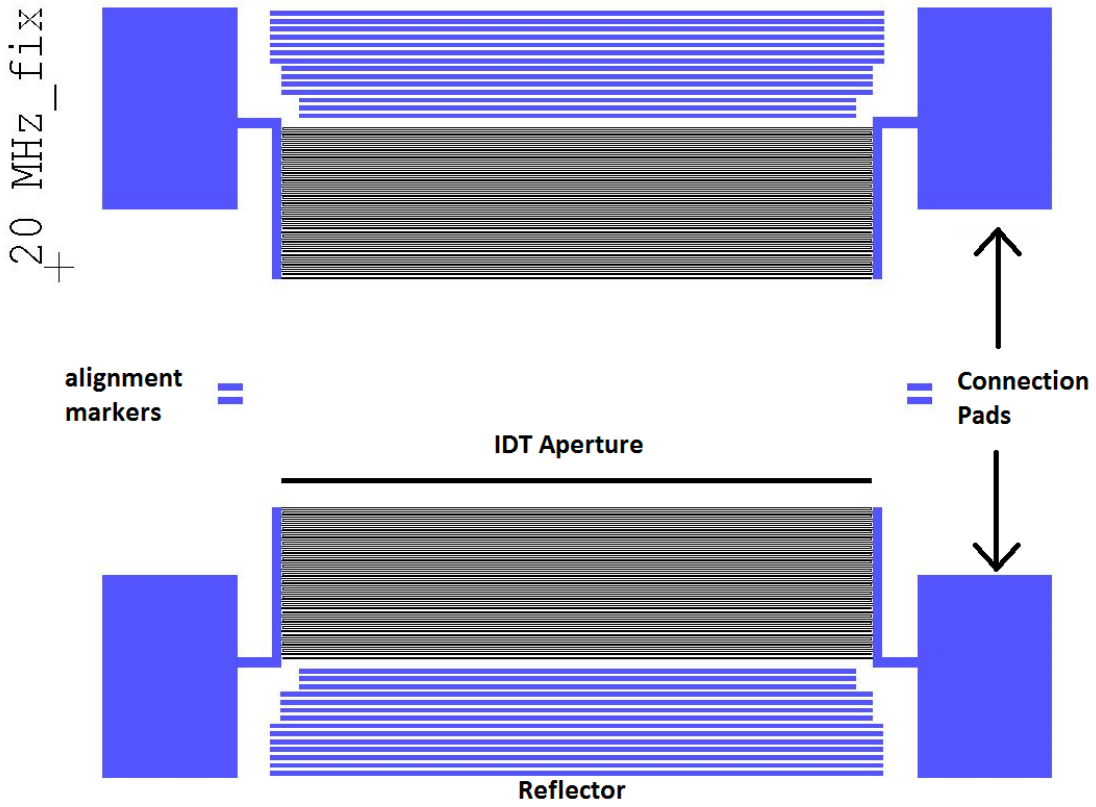

Figure 4.14 L-edit capture of a pair of transducers.

4.5.1.1 Electron beam lithography

After the wafer has been diced, each sample had to be cleaned in the clean room by using the standard procedure. Firstly, the sample is placed in a beaker filled with acetone and the beaker is then placed into the ultrasound bath for 5 minutes, then it is followed by methanol for 5 minutes and IPA for five minutes in ultrasound bath as well. After that, the samples are baked for 5 minutes at 90 degrees Celsius for dehydration. Next each sample is placed inside the barrel asher for oxygen plasma treatment before the stage of resist spinning. The purpose of this is to provide an extra cleaning step and to roughen the surface of the sample for resist to stay on the surface. Consequently, the next step is spinning the suitable resist on top of the substrate. In this case a negative resist protocol is used before sending the samples to the electron beam lithography tool VB6 in the JWNC. More specifically, a first layer of 12 % 2010 PMMA was used, which has a lower molecular weight in comparison with the second layer of resist, indicating higher sensitivity when exposed to the electron beam. It was spun at 5000 rpm for 60 seconds and then prebaked in the hotplate for 1 minute at 65^{o}C, followed by the core baking for 5 minutes at 95^{o}C and last post baked at 65^{o}C for 1 minute. Subsequent, the deposition of a second layer of 2041 at 4 % PMMA was used with the same spinning

parameters. The core baking at 95ºC was set at 2.5 minutes, while the prebake and post bake steps were kept the same. This second layer has higher molecular weight than the first one, resulting in the required undercut in order to have discontinuity between the metal that needs to be deposited and the metal that needs to be discarded. Afterwards, the samples are sent to the VB6 for writing the pattern on top of them. However, $LiNbO_3$ is very sensitive to electron beam lithography, thus an extra step must be introduced to avoid charging that can render the sample unusable. This is achieved by evaporating a layer of 10 nm gold on top of the resist using the metal evaporation (Plassys) tool, hence providing a protection for the sample from the charging effect.

After the pattern is written the layer of gold is removed by using the gold etch solution, which is a wet etch procedure. Then the next step is to develop the resist and observe the desired pattern on the substrate. For the development process the IPA MIBK 2.5:1 developer was used at 25ºC. At this point the sample is ready to follow the metallisation step which it will be described at section 4.5.1.3.

4.5.1.2 Photolithography

For the photolithography procedure the first steps for cleaning the substrate are the same as described in the electron beam lithography procedure. For the resist spinning step a positive photoresist procedure has been followed. More detailed S1818 photoresist was used, utilising a more complicated recipe for spinning as the edge bead effect formed during the spinning needed to be avoided. The first step of spinning was set at 1000 rpm with a ramp of 250 for 5 seconds; the reason for this was to avoid any ununiformed areas from happening. Following the second step was set at 4000 rpm using a ramp of 2000 for a period of time of 60 seconds. Finally, the last step was set at 0 rpm with a step of 1000 rpm at 3 seconds in order to stop smoothly the procedure. For the soft bake procedure, the sample was placed on the hotplate baked at 110 ºC for 3 minutes and 15 seconds. The next step was to rehydrate the photoresist before the exposure to UV light. This was accomplished by using the Microposit developer from concentrated 1:1 mixed with RO water for 100 seconds and then rinse it under water for 5 minutes. The following step was the U.V. light exposure using the (MA-6, SUSS Micro Tec AG)), in order to complete this step a chrome photomask should have been fabricated beforehand. This step was completed by submitting the design as a VB6 job in JWNC and a 5x5 inch chrome mask was produced. Then by aligning the sample in the MA6 under the

desired pattern of the mask UV light was emitted through the mask and the desired pattern was written on the substrate. Due to the use of positive photoresist the exposed areas of the resist are completely gone after the development. The last step before the metallisation process was the development of the photoresist after the exposure using the Microposit developer from concentrated 1:1 mixed with RO water for 75 seconds and rinse under RO water for 5 minutes. The next step was the metallisation process which is described as follows.

4.5.1.3 Metallisation

Before the metallisation process begins there is a step that needs to be followed every time; this step is treating the substrate with the oxygen plasma using the barrel asher. This is of high importance, for removing any residue of photoresist left from the development process and also to ensure that the surface of the substrate is rough enough for the first layer of the metal deposited to be adhered correctly. Failing or skipping this step could result in corruption of the pattern or in some cases completely not adhered metal layer. The following step was the metal deposition using the evaporation tools Plassys 2 and Plassys 4 in the JWNC. For the purpose of fabricating these IDTs the first layer was Titanium (Ti) due to its great adhesion properties on top of lithium niobate and then a layer of gold (Au) on top of the Ti layer. The thickness of each material was 15 nm of Ti and 60 nm of Au. This recipe provided a well adhered and robust pattern that could lead to a fast lift off process. For the lift off process the samples were soaked in acetone and then in a hotbath at 50^{o}C for an hour. After that the pattern was easily observed and if it was not, allowing a little more time in acetone would be sufficient. What was described above can be seen by the flow diagram of the fabrication process depicted in Figure 4.15.

Figure 4.16 shows a black $LiNbO_3$ at 127.86^{o} Y- cut orientation substrate with two fabricated opposing transducers on top of it. At this stage the sample was ready for post processing inside or outside the cleanroom.

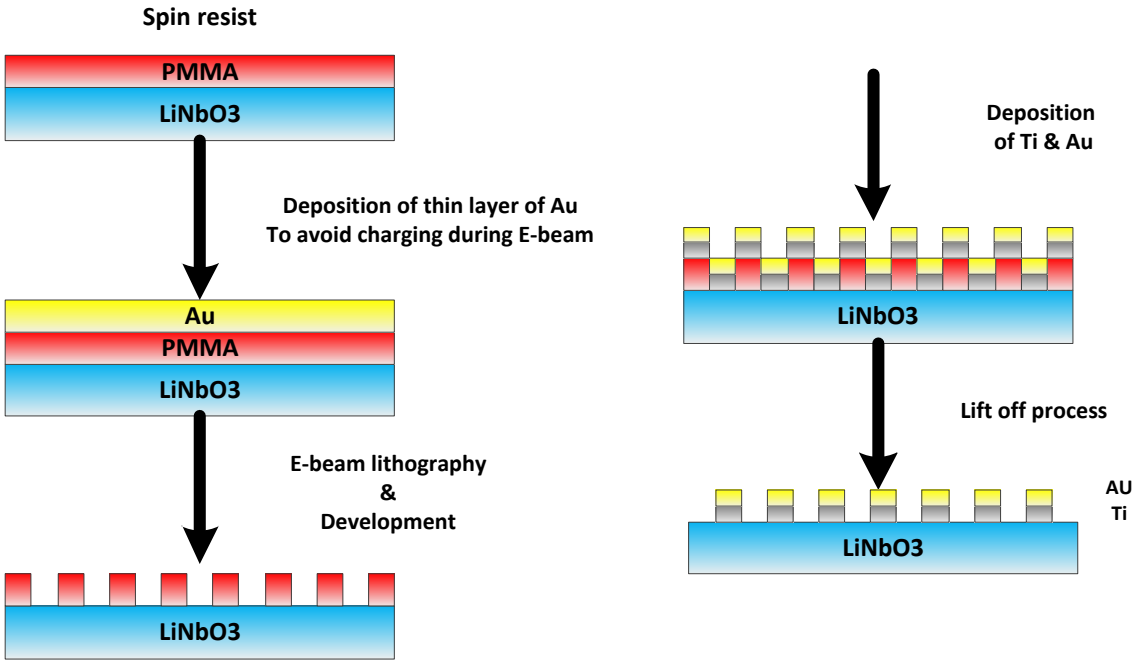

Figure 4.15 Flow diagram of the fabrication process of a pair of opposing IDTs.

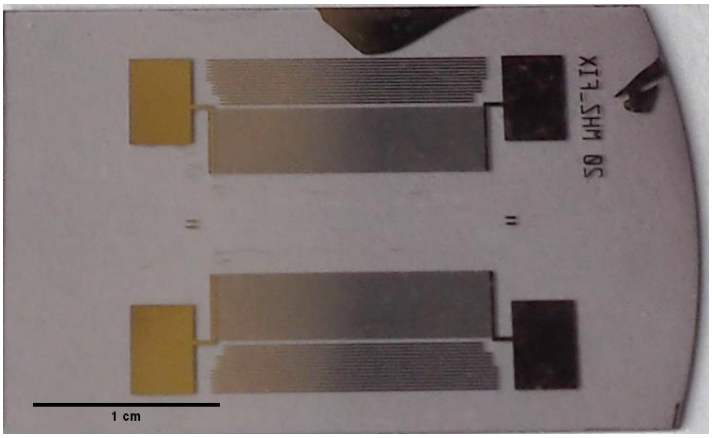

Figure 4.16 Fabricated SAW device.

4.5.2 Fabrication of SU8 microfluidic channels

The first step for the fabrication of the microfluidic channels was to make a mould constructed from patterned SU8 (negative photoresist) on top of a silicon (Si) substrate, by using a standard UV photolithography procedure. For patterning the SU8 the first step was to clean the Si substrate, which was completed by putting the substrate inside acetone for 5 minutes in an ultrasound bath, then it was soaked 5 minutes in methanol and 5 more minutes in IPA. Afterwards, the dehydration procedure was followed as described in Section 4.5.1.1. The next step was the SU8 resist spinning. SU8 is a versatile material that can achieve thickness from 3

µm to 150 µm depending on the viscosity of the SU8 and the spinning time and speed. For instance, SU8 3005 can reach 5-6 µm in thickness while the SU8 3050 can reach up to 60-70 µm according to the datasheet from the manufacturer. Using the developed spinning procedure it was managed to achieve thickness equal to 140 µm. Figure 4.17 shows the measurement of such a thickness using the dektak tool in the JWNC, this particular sample was spun at 1000rpm for 30 seconds using the SU8 3050.

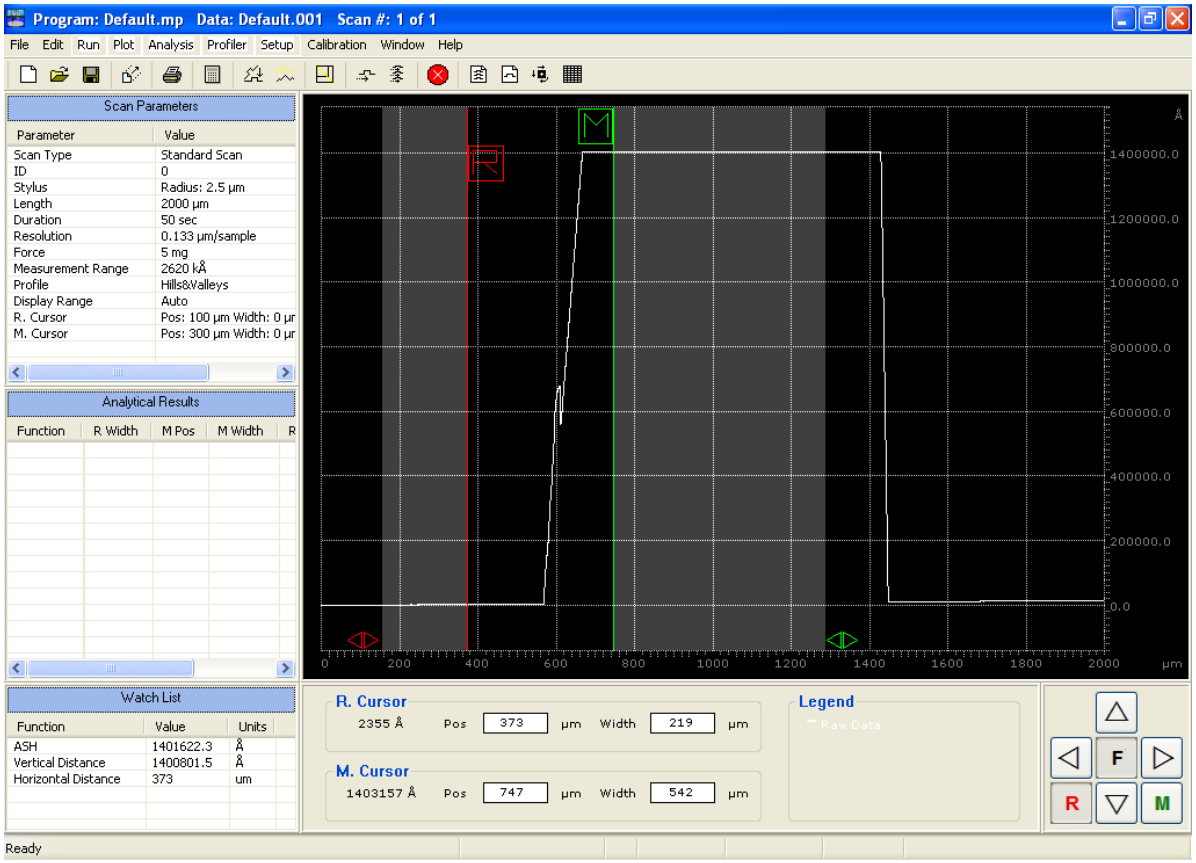

Figure 4.17 Dektak measurement of SU8 thickness.

For the development of the following process two key characteristics were taken into consideration, the first one was the speed of the spin and the other was the time of the spin. For this work a thickness of 50 µm SU8 was needed which was achieved by utilising the following procedure. The first step of the spinning procedure was set at 700 rpm with a ramp of 100 for 5 seconds, the reason for this was to avoid any non-uniform areas from occurring. The second step was set at 3250 rpm using a ramp of 250 for a period of 20 seconds. Finally, the last step was set at 0 rpm with a step of 1000rpm at 3 seconds in order to stop smoothly the procedure. For the soft bake procedure, the sample was placed on the hotplate baked at 95 ºC for 30 minutes. Leaving the sample to dry in room temperature for an hour or even overnight if

possible was necessary for avoiding the sample to get stuck on the mask plate during the UV light exposure. The following step was the UV light exposure using the (MA-6, SUSS Micro Tec AG)), in order to complete this step a chrome photomask should have been fabricated beforehand. This step was completed by submitting the design as a VB6 job in JWNC and a 5x5 inch chrome mask was produced. Then by placing the sample in the MA6 under the desired pattern of the mask UV light was emitted through the mask and the desired pattern was written on the substrate. Due to the use of negative photoresist the exposed areas of the resist stayed intact while the unexposed areas were completely gone after the development. Afterwards, for the post exposure bake step that was making the SU8 hard and adhered to the substrate, the sample was placed at 100 ^{o}C for 3 minutes. The development of the SU8 photoresist was completed by using the EC Solvent for 5 minutes and rinse in isopropanol for 5 more minutes. The next and final step was the baking stage for mechanical cure, at 120 ^{o}C for minimum 2 hours. Figure 4.18 illustrates the flow diagram that was followed in order to fabricate the SU8 mould for the PDMS microfluidic channels.

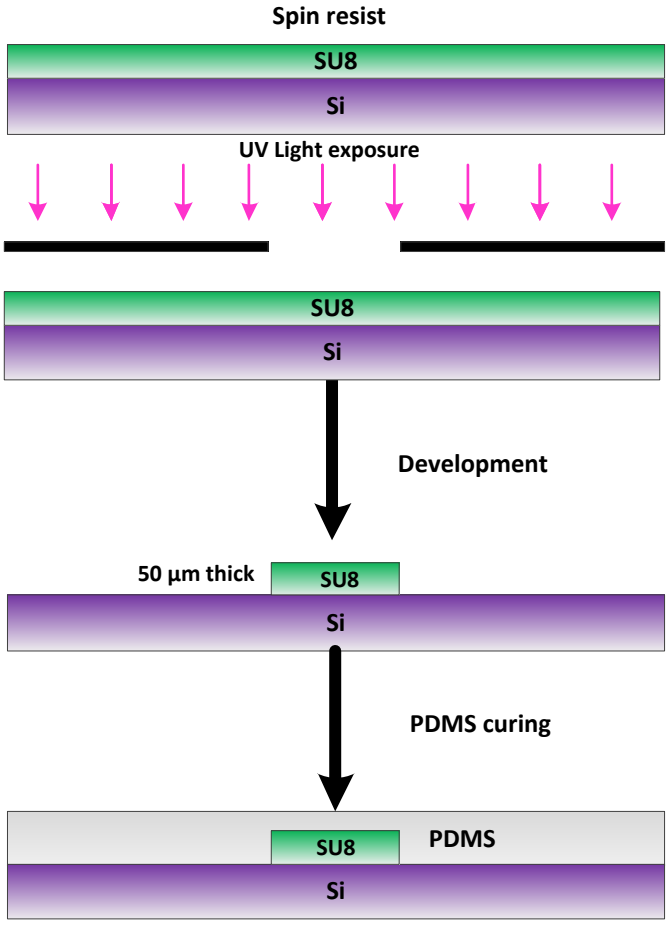

Figure 4.18 Flow diagram for the fabrication of SU8 moulds for microfluidic channels.

Figure 4.19 illustrates a patterned SU8 microfluidic channel mould with three inlets and three outlets, with a measured height of 47 μm and the width of the channel designed at 100 μm.

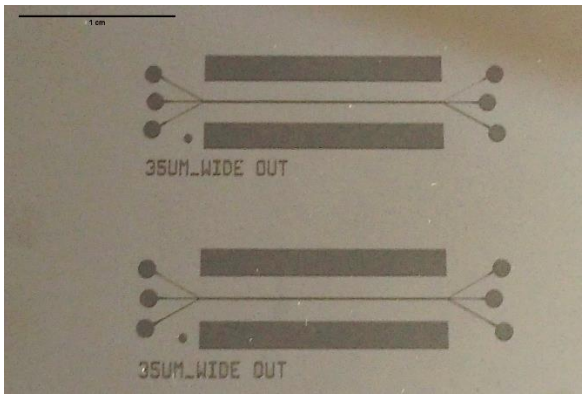

Figure 4.19 Image of patterned SU8 microfluidic channel mould.

4.5.3 Fabrication of PDMS microfluidic channels

The need of microfluidic channels for transporting particles and cells from the inlets to the outlets, drove the use of polydimethylsiloxane PDMS. It is a polymer, which can be easily patterned and bonded on top of the substrate by chemical treatment of the surfaces to make weak Vanderwaals forces that could hold fluid pressures up to around 5 psi [174], thus, providing the advantage of not having leakages and also a sturdy bond over time after reusing the same device.

In order to pattern the PDMS, a substrate is needed for hosting the reversed pattern that could be used as a mould. This surface for such an application is a silicon substrate. SU8 resist can be patterned on top of the silicon substrate and then use it as a mould for the PDMS as described in detail in section 4.5.2. A last step is required in order to make the surface of the mould hydrophobic, this process is called silanisation. Providing the advantages of easy demoulding of the PDMS microchannel from the SU8 mould [175], and also minimising any residue that might occur during this process. In order to achieve this, the SU8 mould was placed inside a mixture solution of 30 μl of Trichloro (1H,1H,2H,2H-perfluorooctyl) silane (Sigma Aldrich) [176] and 50 ml of heptane (Heptane CHROMASOLV ®Plus, Sigma Aldrich) leaving it to cure for 10 minutes and then rinse under RO water.

The PDMS comes in two parts from the supplier, one elastomer base sylgarg 184 part and one curing agent. For the preparation of the PDMS a mix of 10:1 ratio between the elastomer base

and the curing agent was used. The mixture was placed into a degassing chamber in order to remove the airbubbles created during the mixing of the two parts. The degassed content was then transferred into the mould that was fabricated in section 4.5.2. For the curing process of PDMS, the whole system is placed into the oven for two and a half hours at 65 ^{o}C. The microfluidic channels can now be demoulded and stored for future use; this procedure can be repeated several times. When loss of the hydrophobic properties is observed, the silanisation process can be repeated in order to reuse the same mould. A last step before the microfluidic channel could be bonded on top of the substrate is to make the holes of the inlets and outlets for the tubes to be attached on the channel. That was achieved by using a 2 mm PDMS puncher, often described as biopsy punch for medical applications. The following images in Figure 4.20 a) and b) show the PDMS microfluidic channel before and after the holes were made, respectively.

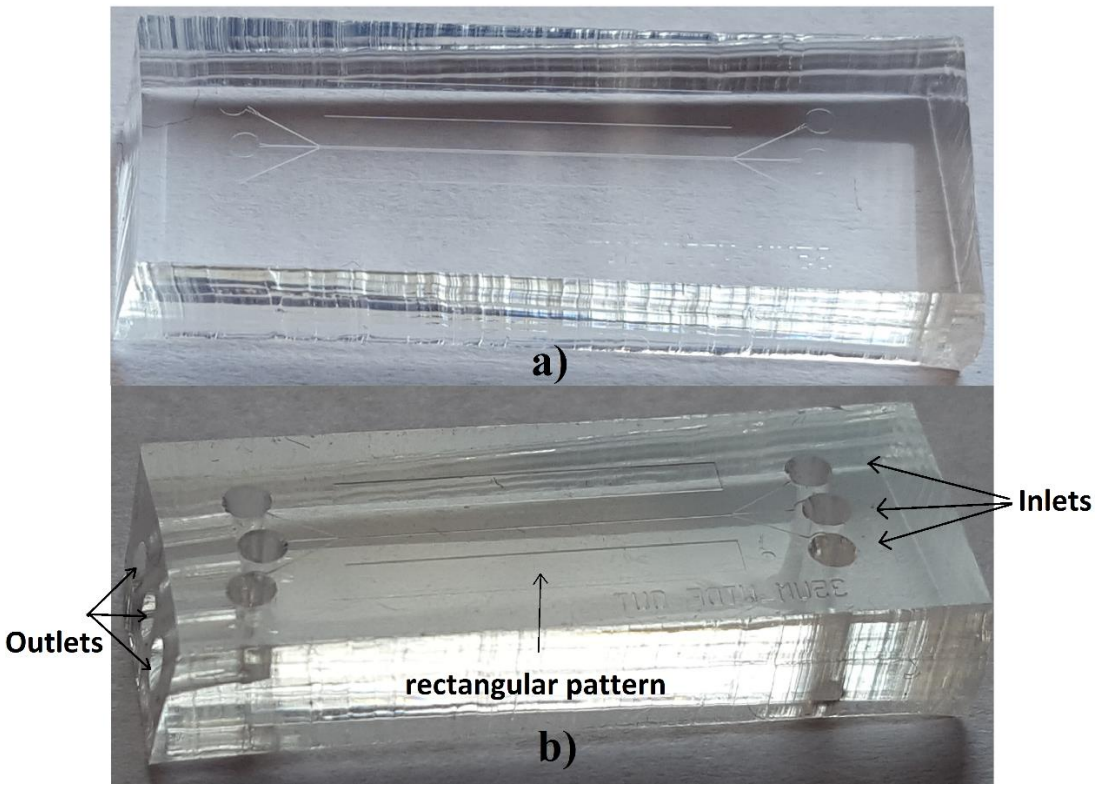

Figure 4.20 Image of fabricated PDMS microfluidic channel a) without holes and b) with holes.

As can be observed from Figure 4.20, two rectangular patterns were placed parallel to both sides of the channel for allowing the surface waves to travel into the channel with the minimum absorption from the PDMS.

4.5.4 Bonding PDMS channels on top of SAW devices

At this point the PDMS channels are ready to be bonded on top of the SAW device. The first step is to clean both the substrate and the PDMS channel by placing them in methanol in an ultrasonic bath for 10 minutes and blowing them dry using a nitrogen gun. Then place them in the oven for 30 minutes at 90ºC in order to dry them completely. The next step is the most critical one and needs to be followed exactly otherwise it may result in repeating all the steps described above or even worse the channel may come off after the curing time. That step is to put both the SAW substrate and the PDMS channel inside the barrel asher in the clean room for O_2 plasma exposure with the surfaces to be bonded facing up. PDMS material is mostly assembled from repeated units of $–O\text{-}Si\text{-}(CH_3)_2$, which on exposure to oxygen plasma develop silanol groups (Si-OH) at the expense of methyl groups CH_3. The oxidation of the surface layer increases the concentration of hydroxyl groups and this leads to the formation of strong intermolecular bonds [177]. As the silanol groups are polar in nature, they make the exposed surface highly hydrophilic. When two such layers are brought into contact, these silanol groups condense with each other. For both PDMS and $LiNbO_3$, these reactions produce Si-O-Si bonds after loss of a water molecule. This results in covalent bonds forming the basis of a tight irreversible seal between the layers [178]. The parameters used for this procedure after a lot of try and error were 100mW for 2 minutes and then immediately make the bond between the two surfaces by bringing them in contact and making sure to align the channel parallel to the transducers. If the bond was not good enough, then the channel should be removed and repeat all the steps. If the bond seems strong then the device is placed inside the 90ºC oven for a minimum of 30 minutes or overnight for curing. Due to the fact that the alignment of the bond needed to be performed by hand and there was only one chance to make it, a lot of devices were suffering from misalignment. By adding an extra step in that procedure perfect alignment has been achieved every time. This extra step was to put 1 or 2 drops of methanol on the LiNbO3 substrate before making the bond, providing the opportunity to move the PDMS channel on the substrate and find the perfect alignment, the methanol drops would evaporate shortly after leaving the PDMS on top of the substrate to cure. The next image illustrated in Figure 4.21 shows an example of a PDMS microfluidic channel after the bonding described above.

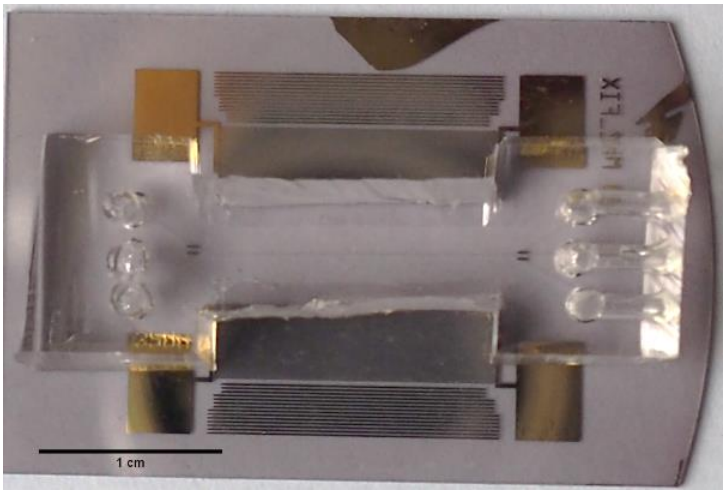

Figure 4.21 Image of a bonded PDMS microfluidic channel on top of a SAW device.

4.5.5 Characterisation of SAW devices

For the characterisation of the fabricated SAW device the network analyser of Agilent technologies E5071B was used. By measuring the scattering or S-parameters of each IDT on the network analyser, the reflection coefficient of the SAW device can be determined. The S-parameter describes an electrical network as a black box and contains information about the magnitude and the phase of the signal. It is affected by the frequency and the impedance of the load and the source. The S11-parameter gives information on the reflection coefficient, meaning the fraction of the electric signal reflected back to the network analyser. A sharp dip in the reflection spectrum around the expected frequency range was used to find the exact resonant frequency of the IDT. As it can be seen in Figure 4.22, the measured resonant frequency of the fabricated IDT is equal to 19.78 MHz which is very close to the value derived from the simulations equal to 20 MHz. The measurements were analysed by using the software Wincal, which provided a Smith chart, a frequency response and the impedance of the transducers, an example of this analysis for a pair of transducers is shown in Figure 4.23.

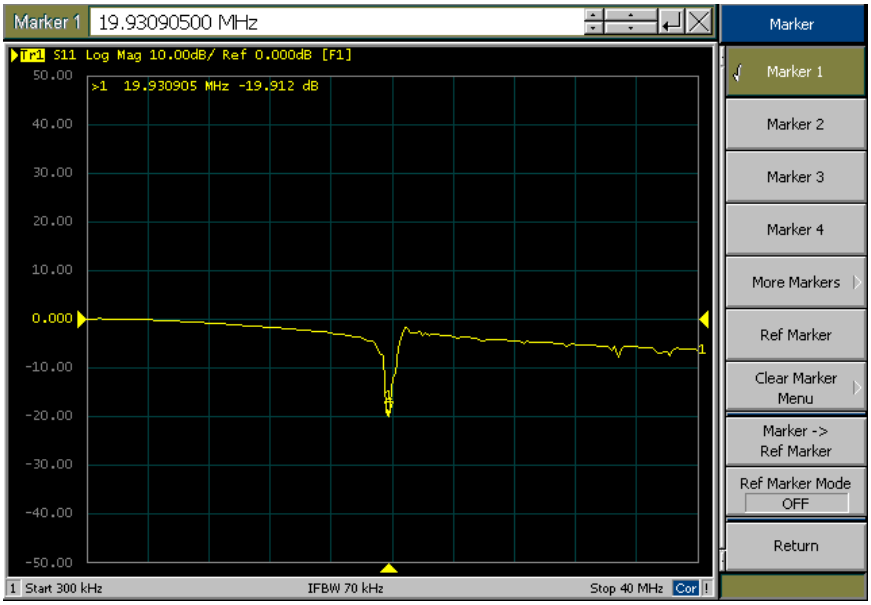

Figure 4.22 Image of a network analyser measurement of a transducer on a SAW device.

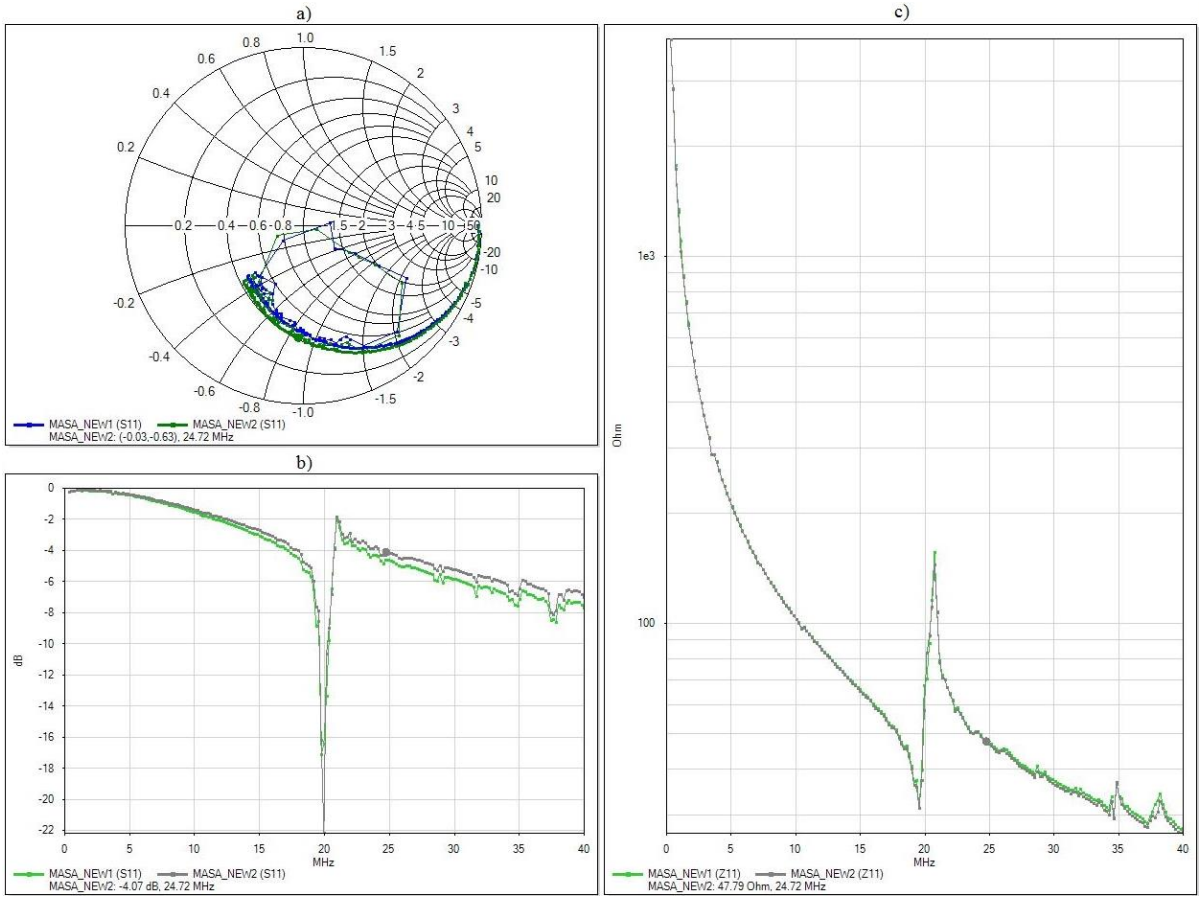

Figure 4.23 Wincal software showing the comparison of S11 parameters of two IDTs on a SAW device under the form of a) Smith chart b) frequency response of a typical reflection spectrum and c) impedance spectrum.

4.6 Summary

In this chapter a novel acoustic manipulation method of particles and cells was presented. The principle of operation of the dynamic acoustic field by continuous change of the phase of one of the opposing transducers was demonstrated. Acoustic separation simulations were presented in order to demonstrate the ability of the proposed method to sort particles and cells. Firstly, the separation simulation of the sorting capability depending on the size of the particles and cells was presented. Secondly, the separation simulation of the sorting capability regarding the particle and cell density was described. An overview was given of the mechanism of controlling the signal generator and achieving fast phase shift between the TDXs through the use of Labview. The methods and materials were presented, that were used in order to fabricate and characterise the TDXs of the BAW device. The techniques and the materials of the fabrication of the SAW device were given, along with the characterisation of the IDTs. The methods of the fabricated microfluidic channels were presented accompanied with the bonding technique of the channel on top of the $LiNbO_3$ substrate used in order to fabricate a throughput SAW device.

5. Experimental results using PZT plate device

5.1 Experimental setup

For the purposes of this set of experiments an arbitrary waveform generator (TGA12104, Thurlby Thandar Instruments, UK) has been used in order to drive the signal to each transducer and synchronise them. This allows independent control of the amplitude, phase and frequency of each channel. Furthermore, instead of driving the signal directly to each TDX, it was amplified and matched by high-speed buffers (AD811 Analog Devices USA; BUF634T, Texas Instruments, USA), before being fed to the transducers via length matched coax cables. This is important because according to the theory of the acoustic radiation forces, see equation (3.14), the forces can be increased by increasing the acoustic pressure gradient. This can be achieved with high focused ultrasound simply by introducing an electrical signal into the device. Thus, the signal has the minimum of distortion when arriving on each transducer, with the advantage of using the maximum energy that the generator can provide. In order to control the signal generator a Labview code was generated as described in section 4.3, by communicating through a general purpose interface bus (GPIB). Then the signal was fed initially in phase to each transducer in order to have the particles aligned at the nodes under the effect of the standing waves that were formed from the opposing transducers as described in section 4.1. The device was placed under an inverted microscope with the capability of taking images of the particles in real time while conducting the experiment. Figure 5.1 illustrates the experimental setup of the BAW device.

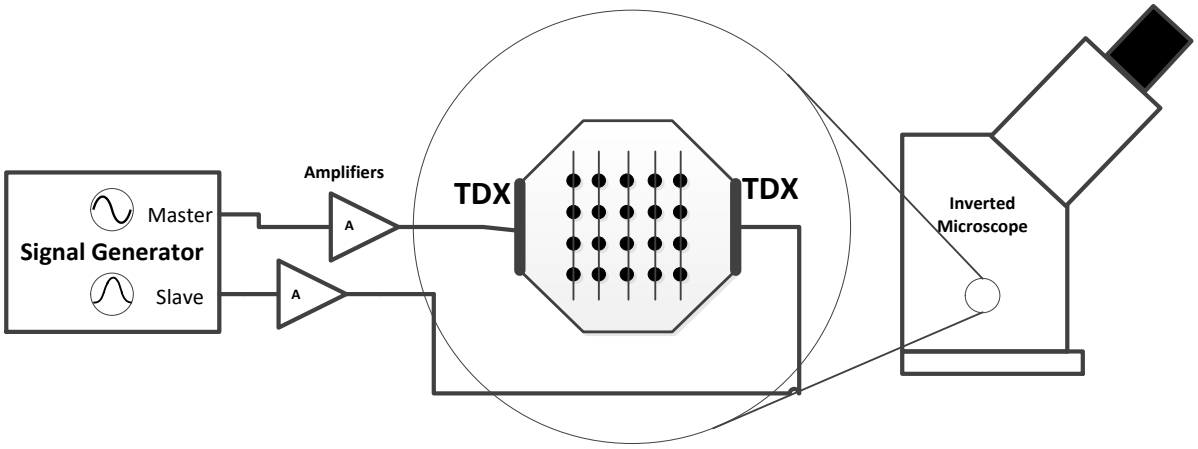

Figure 5.1 Experimental setup of experiment using the BAW device.

Due to the Eckart streaming effect [179], the height level of the particles in the cavity inside the ultrasound device had to be risen to an equal height level to the middle of the transducer. The material that was used in order to achieve that is called agar. Agar has a powder form, but when mixed with water it gains a liquid form at temperatures between 95º and 100º C. When the temperature drops to room temperature agar dries and becomes solid in a transparent form. Agar has very good acoustic properties and sound can travel through it. It can last for the duration of the experiment, approximately half day, but then slowly shrinks if not kept hydrated and needs to be changed for the next experiment. Simply by heating up the mixture that is already prepared, it can be used for the next experiment. The proportion of agar in water was 1.5 grams of agar in 100 ml of deionised (DI) water.

5.2 Sorting particles by size

This section describes the ability of the device of sorting particles of different diameter. As a starting point for the proof of concept sorting experiments of 45 μm from 10 μm polystyrene particles took place, in a homogeneous medium inside a cavity between a pair of opposing transducers as described in section 4.4.1 (see Figure 4.10). The reason that polystyrene particles were used in the experiments was the fact they are a reasonable substitute for biological cells [180]. The results showed that the sorting was successful and are summarised in more detail in section 5.2.1. The sorting capability of the DAF method was further investigated by experiments on sorting 10 μm from 6 μm polystyrene particles, the results are described in section 5.2.2. Further, successful experiments of sorting 10 μm from 8 μm particles in diameter are described in section 5.2.3 and finally in order to push the limits of the method and device, sorting of 6 μm from 5 μm particles was achieved, with only 1 μm difference in diameter between the two populations.

During the experiments the frequency of the transducers used was at 4.00 MHz which was the resonant frequency of those transducers, with the amplitude of the signal set to 8 Vp-p. At this frequency, the wavelength of the sound waves in water is $\lambda = 370$ μm (the velocity of sound in water is 1480 m/s) [181]. Each standing wave is formed at a distance of $\lambda/2 = 185$ μm [17],[182] from the previous one, where the particles agglomerate at the nodes under the acoustic pressure acting on them. In order to estimate the magnitude of the acoustic pressure applied to the different diameter of particles (5,6,8,10, and 45) μm, the time needed for the particles to agglomerate at the nodes starting from a randomly distributed motion state was investigated. All the particles details are given in Appendix A. These experiments were repeated five times

at five different locations within the device using time-lapse microscopy. The drag force, F_d, derived from the dimensions and density of the particles as well as the viscosity of the medium, equation 3.20, allows the acoustic pressure amplitude acting on the particles to be calculated. Those values were calculated equal to 4.8 $\times 10^4$ Pa, 8.5$\times 10^4$ Pa, 9.4$\times 10^4$ Pa, 11.2$\times 10^4$ Pa and 12.1$\times 10^4$ Pa for 5, 6, 8, 10 and 45 μm diameter polystyrene particles, respectively [183].

5.2.1 Sorting 45 and 10 μm particles

For the separation experiments that were performed, a mixture of particles of the two populations has been used. The particle concentration of both the 45 μm and 10 μm was 4.99 x 10^3 particles/ml and 4.55 x 10^5 particles/ml, respectively. The ratio of the mixture of the 45 and 10 μm particles was 1:100. There was no aggregation of particles observed at this concentration. As described in section 4.2.1, the time variant acoustic field was able to transport, and at the same time, separate particles according to their size as shown in Figure 5.2.

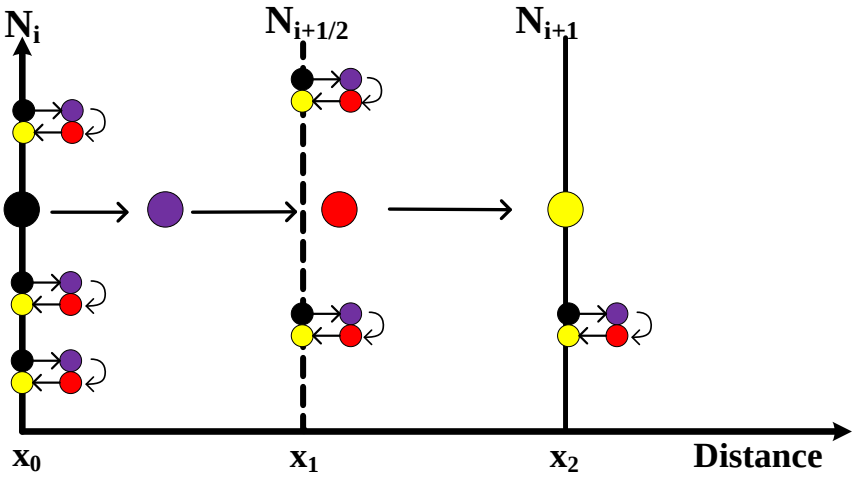

Figure 5.2 Expected position of the particles as a function of time (represented by colour).

Figure 5.2 shows the expected behaviour of the large and small particles over time, with the different colours representing a time interval in relation with the initial position of the nodes indicated by N_i and N_{i+1} and antinodes indicated by $N_{i+1/2}$ of the acoustic landscape, (black is equal to t_0, purple t_1, red t_2 and yellow t_3). Smaller particles experience less force and consequently move over a smaller distance. During the period of time, t_{rest}, the smaller particles return to their initial position while the larger particles transport and settle at the next node.

Figure 5.3 shows particle traces as a function of time (119 frames covering 60 s) in a hyperstack of images as they have been collected from an experiment with the parameters of t_{ramp} set at 5sec and t_{rest} equal to 7sec. The colour time scale bar shows the change from frame 1 darker black to frame 119 brighter white. As it is readily observed, the 45 μm diameter particles followed the shifted acoustic field. This means that they were moving towards the right hand side, while the 10 μm diameter particles stayed close to the position of the original node. The program that has been used in order to capture all the images is the HCImage live of Hamamatsu. The objective lens used for this experiment was the x5 Hamamatsu lens at 100 μm per 145 pixels and the time between each frame was 0.5 s. The average velocity of the small and large particles during t_{ramp} was 5.6 ± 0.5 μm/s and 16.6 ± 1 μm/s, respectively.

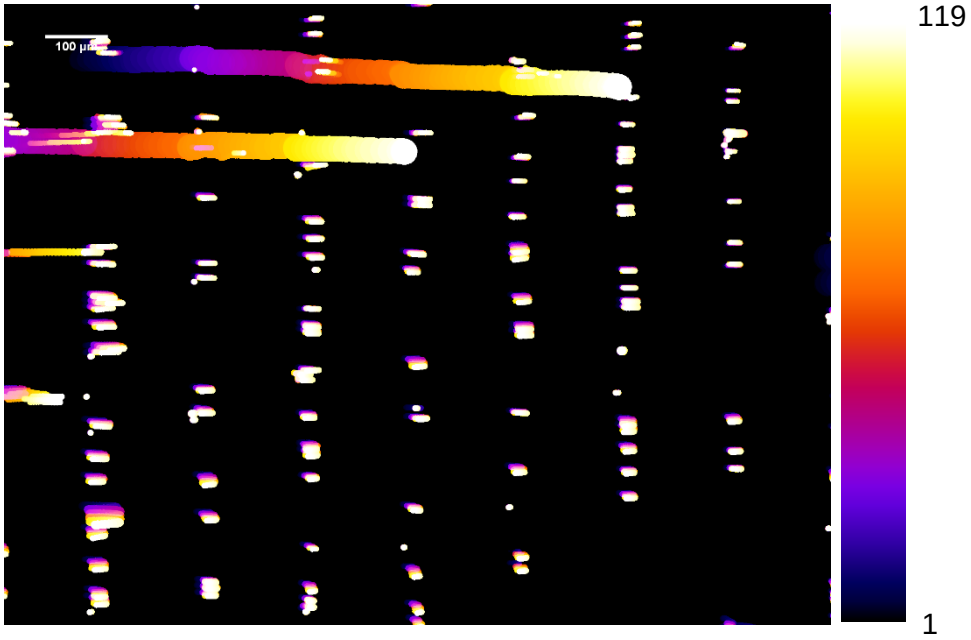

Figure 5.3 Experimental results for sorting 45 and 10 μm particles.

Figure 5.3 was created by using FIJI/ImageJ software. The image stack was then analysed and the particle positions were extracted. The extracted data (x, y, particle area) were used to calculate the efficiency given in equation (5.1) and purity shown in equation (5.2) of the particle separation for each experiment by computing the particle density projected along the nodal lines and analysing the time variation of this density. Seven consecutive nodes can be observed in Figure 5.4a that show the initial position for 10 and 45 μm diameter particles. Figure 5.4b shows the displacement of a 45 μm particle and a 10 μm particle for five cycles of continuous phase shift including the period of time of t_{rest}. If that displacement is expanded to the total amount of the particles, then it can be seen that the large particles successively travel during

t_{ramp} and stabilise during t_{rest} at the next node, resulting in an overall displacement over time. While the small particles can only move slightly during t_{ramp} therefore not being able to overcome the midpoint of the nodes and consequently return to their initial node position during t_{rest}.

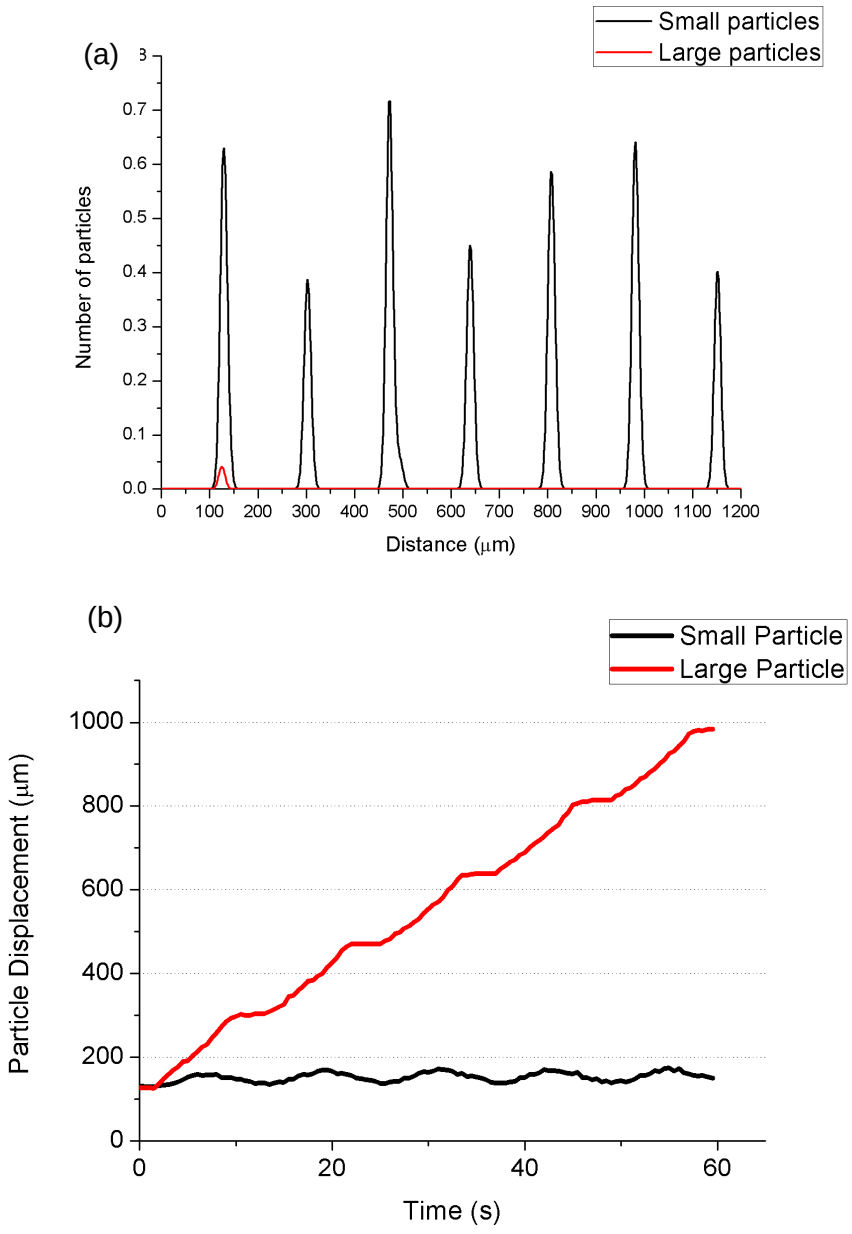

Figure 5.4 Graph (a) showing the total amount of the particles aligned at the nodes and (b) showing the particle displacement for a 45 μm particle (red colour line) and a 10 μm particle (black colour line).

In order to evaluate the experimental results, a factor was needed to measure the successfully separated particles from the mixed population. Thus, the factor of efficiency has been used,

which was calculated by measuring the total amount of the targeted population to be separated (in this case the 45 μm particles) that actually managed to get separated and divide that number by the total amount of the targeted population in the mixture. This percentage can provide the essential information of how efficient the separation was. Also, another factor was needed that could provide the equally essential information of how contaminated the separation by unwanted particles was. This factor is called purity and it was calculated by measuring the total amount of the targeted population to be separated that indeed got separated, divided by the total amount of particles that were separated at the end of the experiment. The description above can be displayed as an equation given as follows.

$$Efficiency = \frac{\text{Target particles in desired area}}{\text{Total target particles in sample}} \cdot 100\% \tag{5.1}$$

$$Purity = \frac{\text{Target particles in desired area}}{\text{Total particles in desired area}} \cdot 100\% \tag{5.2}$$

By combining those two figures of merit in a final grade of separation in order to get a single figure of merit that is dependent on the ramp time and the rest time during the experiment. This final grade is defined as the average of purity and efficiency as shown in the formula below.

$$Final\ grade = \frac{Efficiency\ +\ Purity}{2} \tag{5.3}$$

The DAF method has been used in order to simulate the separation efficiency demonstrated above using the same parameters as the experiments. Table 5.1 (a) shows the simulation results of the final grade. The red coloured regions represent the experimental parameters where the particle separation was not successful whereas the blue areas show the successful separation of particles by using the parameters stated in the Table. Table 5.1 (b) shows the experimental results of the final grade. In the blue regions the achieved separation was higher than 90.1% by using the corresponding parameters while the red coloured regions represent the parameters where less than 80 % separation was achieved. A yellow area in the middle can be observed that shows those parameters where the separation was successful by 80 % – 90 %. Comparing the computational and the experimental results, it can be concluded that there is a good match

between the simulation and the experimental data if the yellow area is considered as successful separation.

Table 5.1 (a) Simulation results and (b) experimental results of the final grade of the separation performance, depending on the ramp and rest time

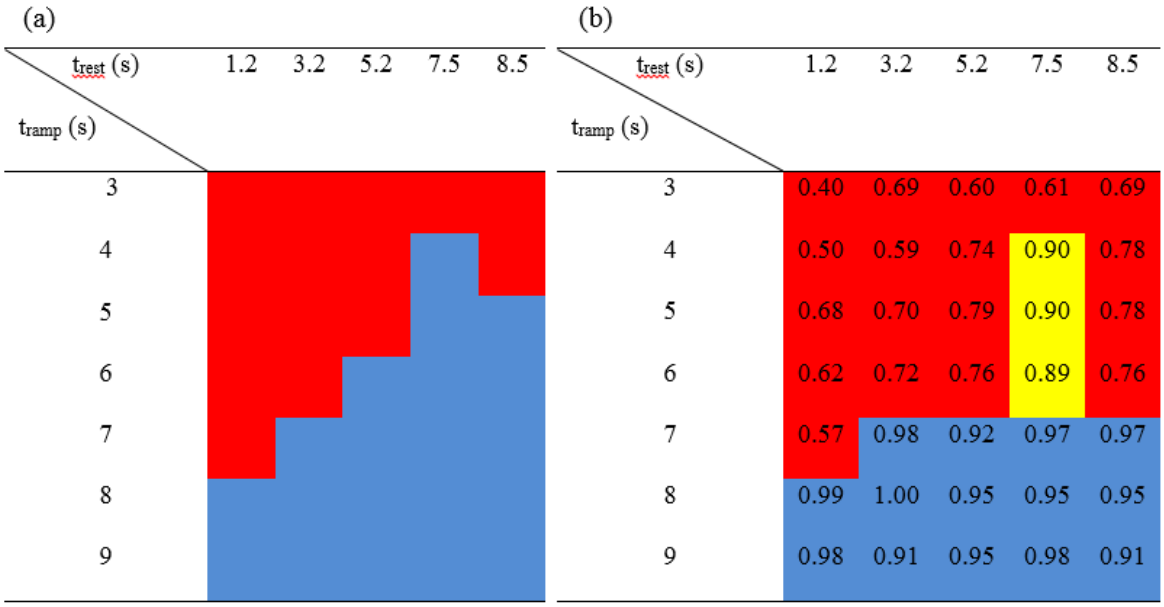

As it can be observed, the separation performance can be improved by rising the t_{ramp} and t_{rest} parameters until it reaches a maximum point. This is an indication that the acoustic forces acting on the particles of interest require a minimum time to overcome the inertia and viscous force in order to transport the particles from the node N_i to the next node N_{i+1}. The ramping time t_{ramp} is the critical parameter, since it has the greatest impact on the separation result. Less influential parameter is the value of t_{rest} on the separation results. When suitable parameters are selected the separation process reaches its best experimental performance: with the separation ratio achieving ~100 % purity and efficiency.

5.2.2 Sorting 10 and 6 μm particles

The simulation and experiments have been replicated using 10 and 6 μm diameter particles. For the separation experiments that were performed for the 10 and 6 μm polystyrene particles, a mixture of particles of the two populations has been used where the particle concentration of 10μm and 6μm polystyrene particles was 16.38 x 10^5 particles/ml and 75.6 x 10^5 particles/ml,

respectively. The ratio of the mixture of the 10 μm and 6 μm particles was 1:4.6. By using this concentration there was no aggregation of particles observed.

Figure 5.5 illustrates particle traces as a function of time (with 71 frames covering 142 seconds) displayed in a hyperstack of images as they have been collected from an experiment with the parameters of t_{ramp} set at 16.2sec and t_{rest} equal to 17sec. The colour time scale bar shows the change from frame 1 darker black to frame 71 brighter white.

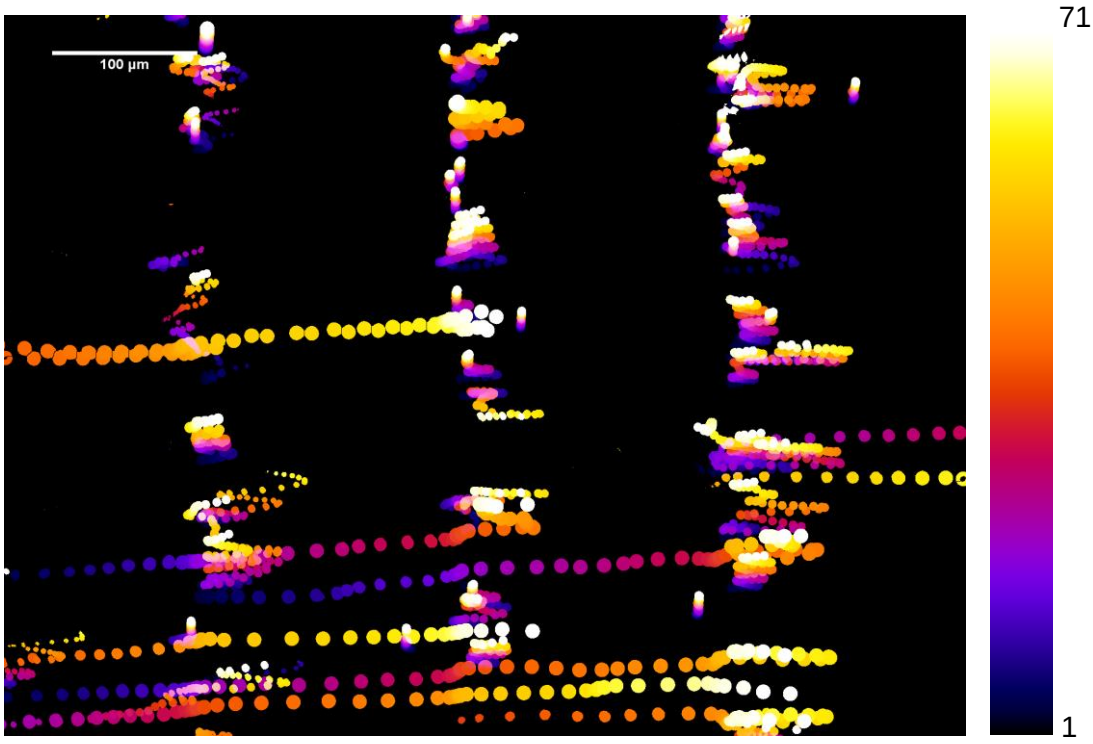

Figure 5.5 Hyperstack of images of experimental results for sorting 10 and 6 μm particles.

As it can be observed, the larger particles 10 μm follow the shifted acoustic field, which means that they are moving from left to right, while the 6 μm diameter particles stay close and return back to the original node. The objective lens used for this experiment was the x10 Hamamatsu lens which corresponds to 100 μm per 290 pixels, the time between each frame was 2 s. The average velocity of small 6 μm and large 10 μm particles during t_{ramp} has been measured at 2 ± 1 μm/s and 10 ± 1 μm/s, respectively. Figure 5.6 illustrates the displacement of a 10 μm in diameter particle versus time and also the displacement of a 6 μm particle on the same graph.

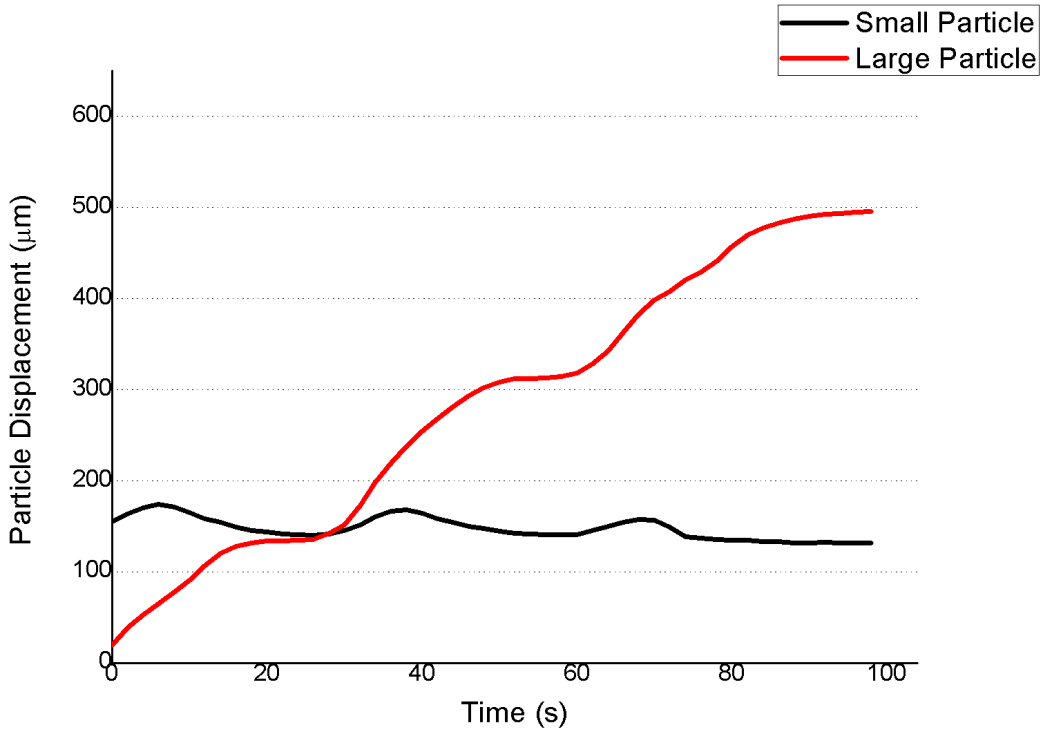

Figure 5.6 Graph showing the particle displacement for a 10 μm particle (red colour line) and a 6 μm particle (black colour line).

As it can be seen by the graph shown in Figure 5.6 the larger particle (10 μm) follows the constantly shifting acoustic field and thus transporting along to the next node each time the phase shift is applied. On the other hand, the smaller particle (6 μm) cannot follow this phase shift since it is not experiencing the same acoustic forces as the large one, which is derived by equation (3.20) as described in section 3.5.1. During the time of t_{ramp} the effect of the phase shift is readily obtained by the slope on the graph for the large particle with the red coloured line and during the period of t_{rest} which can be observed as a horizontal line the particle settles at the next node equal to half the wavelength. At this point, it is worth mentioning that each time a new cycle of phase shift starts, a different gradient follows after the resting period.

In order to evaluate the experimental results, the equations (5.1), (5.2) and (5.3) need to be used, for calculating the efficiency, the purity and the final grade, respectively. For the experiment analysed above the calculation of the efficiency was found to be 97.2 %, the purity was at 97 %, giving a total final grade of 97.1 %. The map of the region of operation for this set of experiments has not been produced since the goal of these experiments was to prove that it can be achieved a high percentage of efficiency and purity.

5.2.3 Sorting 10 and 8 μm particles

In order to push the limits of the device further with particle size difference of only 2 μm in diameter, experiments using 10 and 8 μm particles were performed. The simulation and experiments had been replicated using 10 and 8 μm diameter particles. For the separation experiments that were performed for the 10 and 8 μm polystyrene particles, a mixture of particles of the two populations has been used, where the particle concentration of 10μm and 8μm polystyrene particles was 6.77 x 10^5 particles/ml and 17.7 x 10^5 particles/ml, respectively. The ratio of the mixture of the 10 and 8 μm particles was 1:2.6. By using this concentration there was no aggregation of particles observed.

The experimental setup for this experiment was set to V= 9Vp-p and the frequency of the input signal was set to f = 4.2MHz. The time of t_1 for this experiment was chosen to be 0.97sec using 9 sequential steps of 40 degrees increment between each step, until reaching the 360 degrees of a total phase shift, which gives the final time of t_{ramp} equal to 8.73sec. The time of t_{rest} was chosen to be equal to 3.77sec. Figure 5.7 illustrates particle traces as a function of time (64 frames covering 63 seconds) displayed in a hyperstack of images as they have been collected out of the experiment described above, with the colour time scale bar showing the change from frame 1 darker black to frame 64 brighter white.

The larger particles10 μm can be observed to follow the shifted acoustic field, which means that they are moving from one node to another, while the 8 μm diameter particles move slightly and return back to the original node.

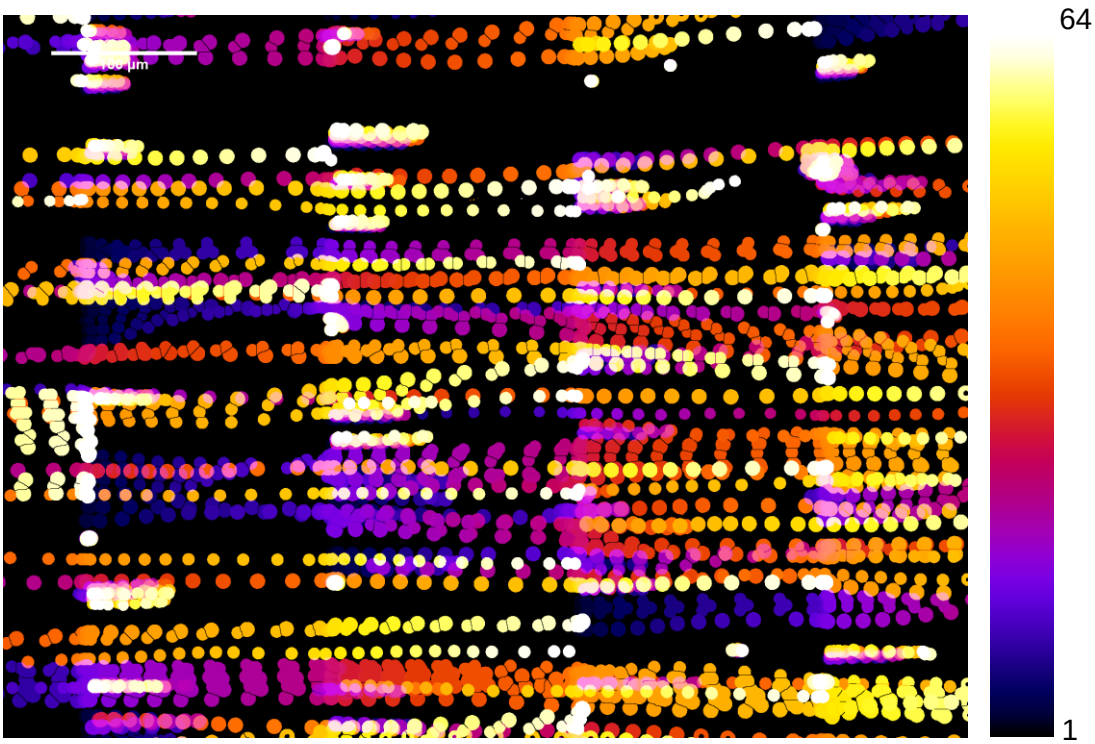

Figure 5.7 Hyperstack of images of experimental results for sorting 10 and 8 µm particles.

The objective lens used for this experiment was the x10 Hamamatsu lens which corresponds to 100 µm per 290 pixels, the time between each frame was 1 s. The average velocity of small 8 µm and large 10 µm particles during t_{ramp} has been measured at 9.2 ± 1 µm/s and 19.9 ± 2 µm/s, respectively. The distance between each standing wave measured from this experiment was found to be 170µm which is really close to the $\lambda/2$=176 µm of the theoretical value.

In the graph depicted in Figure 5.8 is displayed the displacement of a 10 µm and 8 µm polystyrene particle in diameter versus time on the same graph. Again, it can be seen by this graph that the larger particle (10µm) follows the continuously shifting acoustic field, thus transporting along to the next node each time the phase shift is applied. Unlike the smaller particle (8µm) which cannot follow this phase shift as discussed earlier.

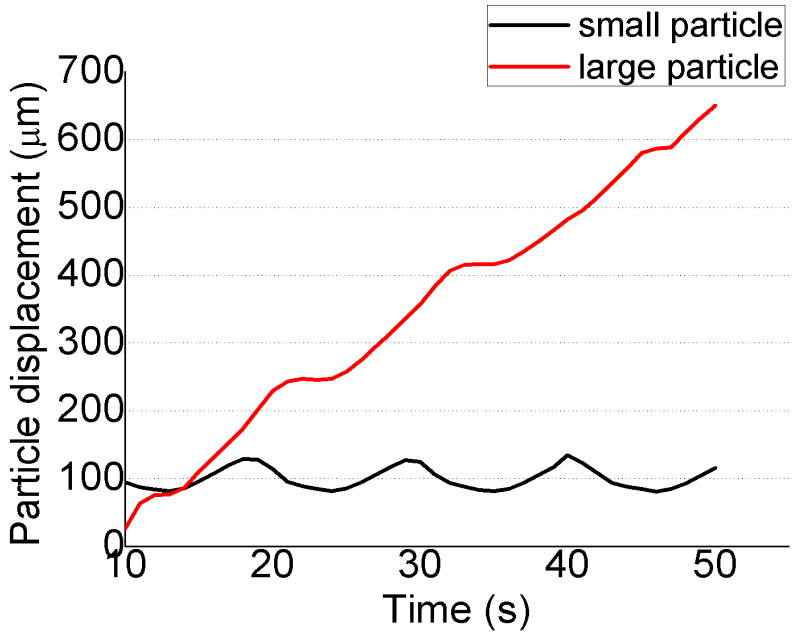

Figure 5.8 Graph showing the particle displacement for a 10μm particle (red colour line) and an 8μm particle (black colour line).

For the experiment analysed above the efficiency was calculated at 96 % while the purity was 64 % which concludes to a total final grade of 80 %. The achieved final grade of this set of experiments was satisfying enough in order to prove the concept of the idea that this device can sort particles such close in diameter as 2 μm. Consequently, for this set of experiments the full amount of experiments was not taken in order to cover all the region of possible experimental results.

5.2.4 Sorting 6 and 5 μm particles

The promising results of the sorting experiments of 10 μm and 8 μm polystyrene particles drove the goal of the next set of experiments, pushing further the limits of the capabilities of the method and device by implementing sorting experiments on 6 and 5 μm particles. For the separation experiments that were performed for the 6 μm and 5 μm polystyrene particles, a mixture of particles of the two populations has been used where the particle concentration of 6 μm and 5 μm particles was 4.5 x 10^6 particles/ml and 18.4 x 10^6 particles/ml, respectively. The ratio of the mixture of the 6 μm and 5 μm particles was 1:4.

The experimental setup for this experiment was set to V= 9Vp-p and the frequency of the input signal was set to f = 4.2MHz. The time of t_1 for this experiment has been chosen at 1.4sec using 9 sequential steps of 40 degrees increment between each step until reaching the 360 degrees of

one total phase shift, which gives the final time of t_{ramp} equal to 12.6sec. The time of t_{rest} was chosen to be equal to 7.2sec. Since the size difference of the particles is so small and considering the large amount of particles inside the mixture, it is very difficult to recognise each population from the hyperstack of images. The picture that is introduced in Figure 5.9 shows the 6 and 5 μm particles aligned at the nodes with both transducers turned on and in phase just before the phase shift starts.

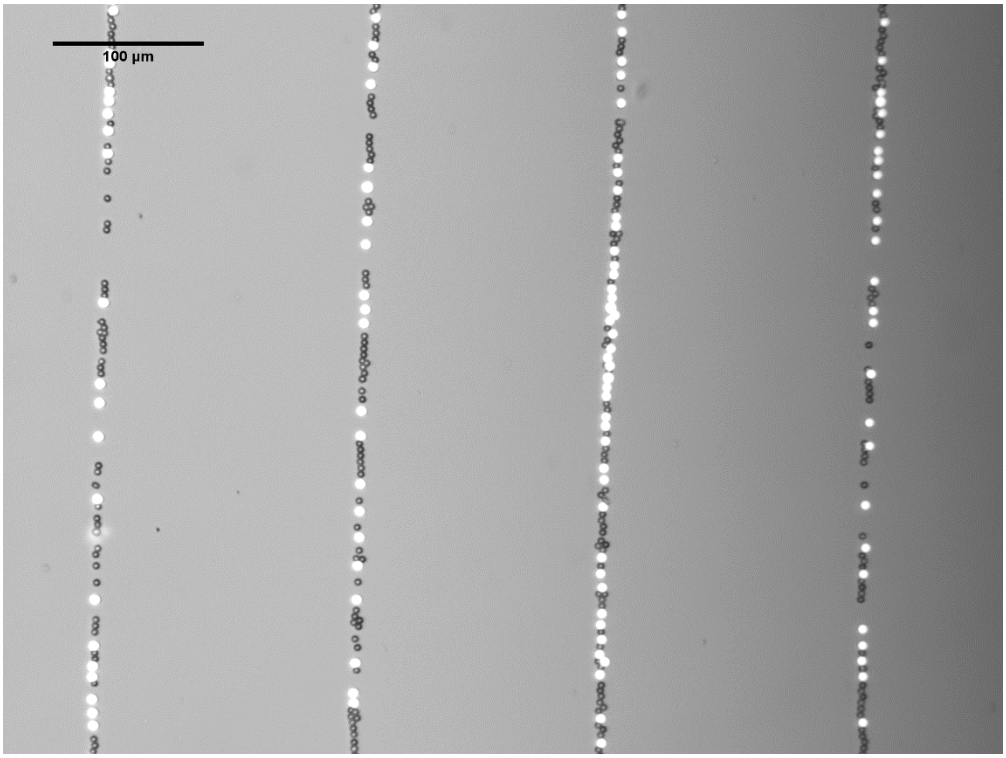

Figure 5.9 Aligned 6 and 5 μm particles under the effect of two opposing transducers.

As it can be observed from Figure 5.9 the larger particles of 6 μm diameter are brighter than the smaller ones. That is due to the fact that particles of 6 μm diameter have been chosen to be fluorescent, thus providing the opportunity to distinguish the two populations easier during the experiments but also during the analysis of the results. In that picture on the top left corner a scale bar is demonstrated showing the length of 100 μm. The distance between each standing wave measured from this experiment was found to be 174μm which is almost equal to the $\lambda/2$=176 μm of the theoretical value.

Figure 5.10 shows particle traces as function a of time (101 frames covering 99 seconds) displayed in a hyperstack of images as they have been collected out of the experiment described

above, with the colour time scale bar showing the change from frame 1 darker black to frame 101 brighter white.

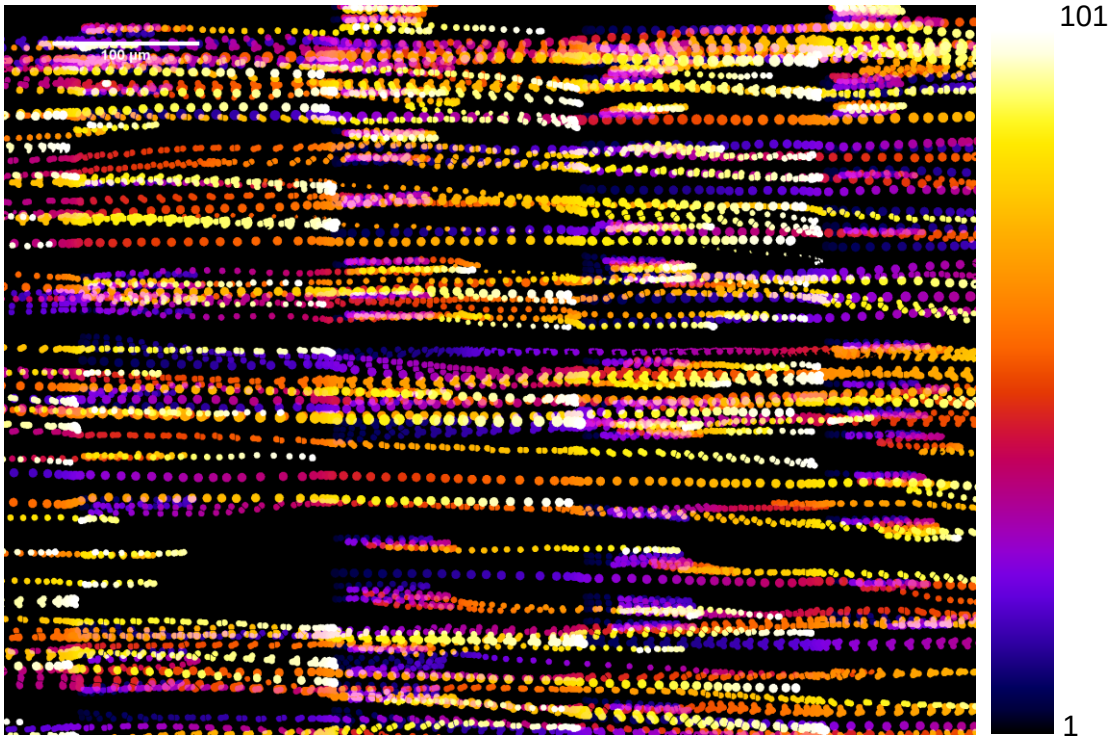

Figure 5.10 Hyperstack of images of experimental results for sorting 6 and 5 µm particles.

The objective lens used for this experiment was the x10 Hamamatsu lens which corresponds to 100 µm per 290 pixels, the time between each frame was 1 s. The average velocity of small 5 µm and large 6 µm particles during tramp has been measured at 5.7 ± 1 µm/s and 11 ± 1 µm/s, respectively.

Figure 5.11 presents the displacement of a 6 µm and 5 µm diameter particle versus the time on the same graph.

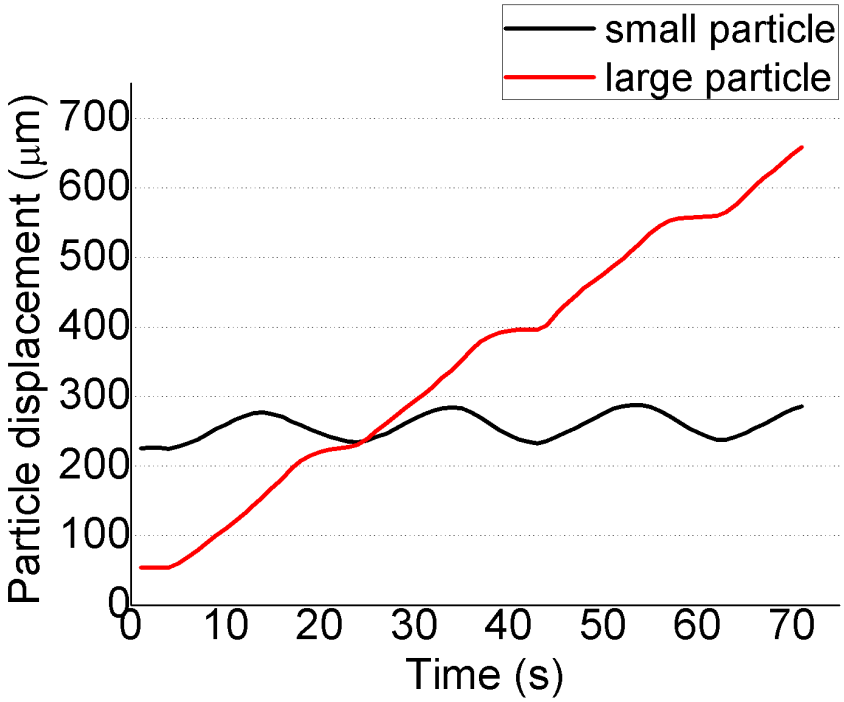

Figure 5.11 Graph showing the particle displacement for a 6μm particle (red colour line) and a 5μm particle (black colour line).

For this experiment the efficiency was calculated at 90.5 % while the purity was 50 % which concludes to a total final grade of 70.25 %. The achieved final grade of this set of experiments was sufficient in order to prove the concept of the DAF method for sorting particles such close in diameter as 1 μm. Consequently, for this set of experiments no further amount of experiments was taken in order to cover all the region of possible experimental results.

The summarised results for all the sorting set of experiments regarding the particle's size are displayed in Table 5.2, which shows the best values acquired from the experiments for efficiency, purity and final grade.

Table 5.2 Results of efficiency, purity and final grade for all the sets of the size sorting experiments

Set of particles to be separated	Efficiency (%)	Purity (%)	Final grade (%)
45 μm from 10 μm	100	100	100
10 μm from 6 μm	97.2	97	97.1
10 μm from 8 μm	96	64	80
6 μm from 5 μm	90.5	50	70.25

5.3 Sorting particles by density

In this section, a description of the ability of the DAF method using the BAW device for sorting particles of different density but of the same particle size is given. The acoustic forces are not solely based on particle size but also depend on density (mass per volume), that hypothesis can be derived from the equation of the contrast factor φ, equation (3.18) that is included in the primary acoustic radiation force equation (3.18). Hence, if the particles have the same size in diameter and their only different property is their density, then they can be sorted according to the theory and the simulations that have been carried out, demonstrated in section 4.2.2 accompanied with the simulation results of Figures 4.5 and 4.6. The separation performance has been examined against particle density by using polystyrene particles of 10 μm diameter and iron-oxide filled particles with a density of ρ = 1.05 g/cm^3 and ρ = 1.41 g/cm^3, respectively. The ratio of the concentration of iron-oxide filled and polystyrene particles was 1:2.

The experimental setup of the input signal and frequency was set to V= 9Vp-p and f = 4.2 MHz, respectively for this experiment. The time of t_1 was chosen to be 1.55 sec using 9 sequential steps of 40 degrees increment between each step until reaching the 360 degrees of one total phase shift, which gives the final time of t_{ramp} equal to 13.95 sec. The time of t_{rest} was chosen to be equal to 14.05 sec, concluding to a total time of 28 sec for each cycle. The image illustrated in Figure 5.12 shows the particle traces as a function of time of 10 μm diameter iron-oxide filled and polystyrene particles in a mixture using the DAF method (140 frames covering 140 s). From this Figure, the effect of the phase shift on the denser particles (iron-oxide filled) is observed, which are moving along with the transportation of the nodes from left to right. However, less dense particles (polystyrene) can only move until a point from which they retreat back to their starting nodal positions. The objective lens used for this experiment was the x10 Hamamatsu lens which corresponds to 100 μm per 290 pixels, the time between each frame was 1 s. The average velocity of the less dense polystyrene particles and the denser iron-oxide filled particles during t_{ramp} has been measured at 3 ± 1 μm/s and 15 ± 1 μm/s, respectively. The distance between each standing wave measured from this experiment was found to be 177μm which is almost equal to the $\lambda/2$=176 μm of the theoretical value.

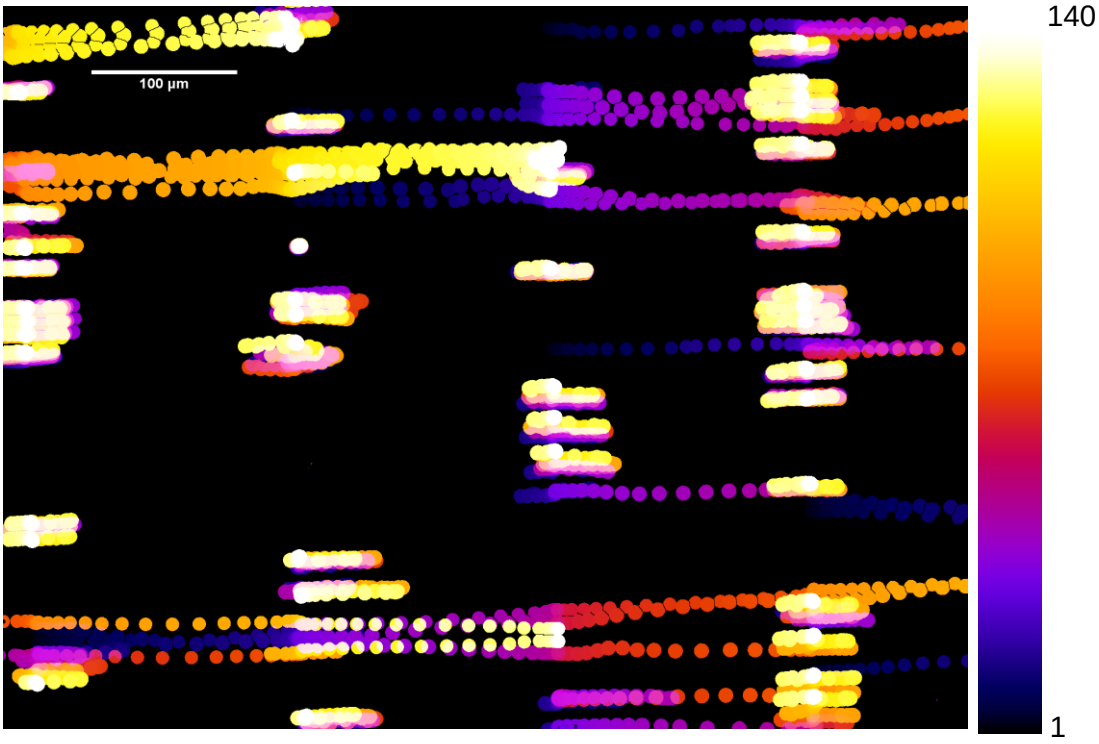

Figure 5.12 Hyperstack of images of experimental results for sorting particles by density.

Figure 5.13 presents the displacement of a polystyrene particle of density ρ = 1.05 g/cm^3 and an iron-oxide filled particle of density ρ = 1.41 g/cm^3 versus time on the same graph depicted from the experiment above. As can be seen the denser particle follows the continuously shifting acoustic field and thus transport along to the next node each time the phase shift is applied. Unlike the less dense particle which cannot follow this phase shift, since it is experiencing lower acoustic forces acting on it during the applied phase shift. During the time of t_{ramp} the effect of the phase shift on the denser particle is readily obtained by the slope on the graph with red coloured line. While, during the period of t_{rest} that can be observed as a horizontal line the particle settles at the next node equal to half the wavelength.

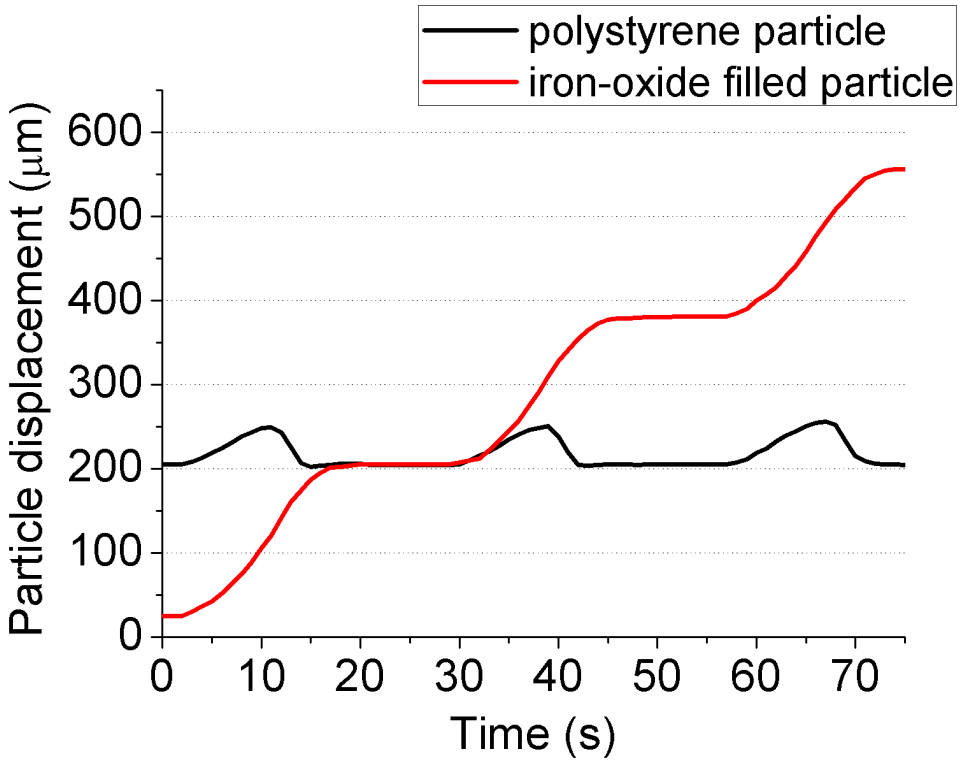

Figure 5.13 Graph showing the particle displacement of an iron-oxide filled particle (red colour line) and a polystyrene particle (black colour line).

For the experiment analysed above the efficiency was found to be 98 % while the purity was 94 % which concludes to a total final grade of 96 %. The achieved final grade of this set of experiments can prove the concept of the sorting capability of the DAF method of particles of the same size in terms of diameter but of different density.

5.4 Sorting cells by size

The second stage of experiments is introduced in this section, after the completion of the first stage of the experiments, which involved the characterisation of the device in terms of its capabilities and limitations for sorting particles of different size. The second stage involves the expansion of the particle sorting experiments by using cells of different size in diameter but of the same density, keeping the same format of experiments as the ones that have been used for the particles. The fact that the acoustic force is proportional to the particle volume of the polystyrene particles as described in section 3.5.1, allows the logical assumption to be made that particles experience forces of the same order of magnitude as cells.

In order to consider a potential practical application, the DAF method was used to separate porcine dorsal root ganglion (DRG) neurons from a freshly isolated mixture containing myelin

debris and other non-neuronal cells. The most common procedure for isolating the neurons would normally be based on their hydrodynamic state using centrifugation across a Ficoll gradient [184]. The porcine DRG neurons have an average size of 17 to 145 μm [171], with a 66% of the populations belonging to the small diameter perikarya with less than 30 μm diameter, 22.6% belonging to medium size meaning between 30-80 μm of diameter and 11.5% fitting in the large diameter >80 μm [185], whereas the myelin debris have a size of a range from 10 to 15 μm.

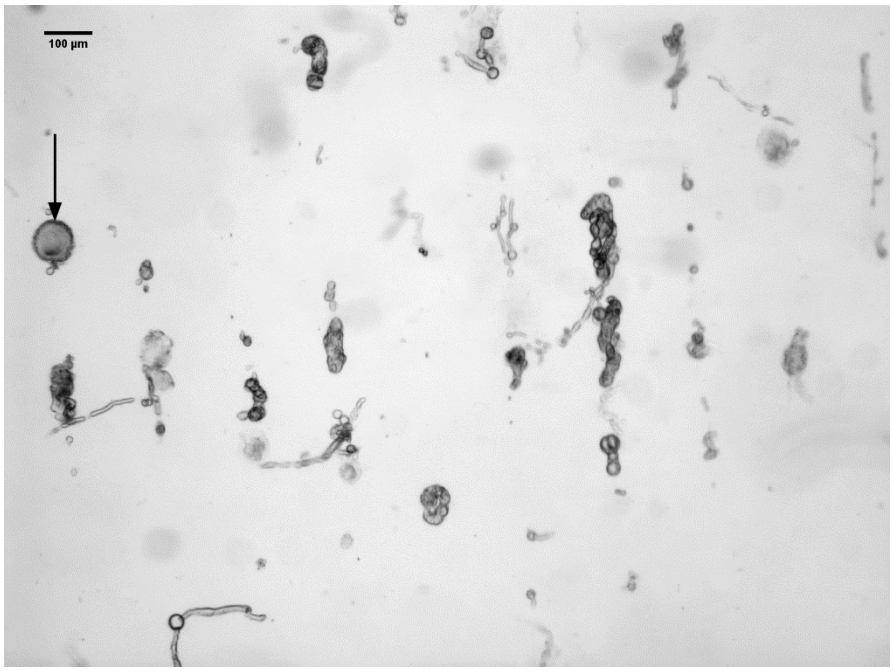

Figure 5.14 Aligned DRG neuron cells and myelin debris at the formed nodes with the arrow pointing to a DRG neuron cell.

The image in Figure 5.14 shows a single DRG neuron of a diameter of (~ 85 μm) and myelin debris (~ 14-35 μm) which stays in the mixture after the extraction of DRG neurons under the effect of the excitation of both of the transducers, which are forming a field of acoustic standing waves. These myelin debris are agglomerating at the nodes of the acoustic field [67] aligning themselves in vertical lines. The scale bar indicates a distance of 100 μm and the arrow points at the DRG neuron cell.

The experimental setup for this experiment was set to V= 8Vp-p and the frequency of the input signal was set to f = 4.2MHz. The time of t_1 for this experiment was chosen to be equal to 0.355 sec using 9 sequential steps of 40 degrees increment between each step until reaching the 360 degrees of one total phase shift, which gives the final time of t_{ramp} equal to 3.2 sec. The time of

t_{rest} has been chosen equal to 4.8 sec. By using these settings, the dynamic acoustic field was applied and the results are illustrated in Figure 5.15. The hyperstack of images shows the overlay of the collected depictions over time (73 frames covering 36 seconds). The colour time scale bar shows the change from frame 1 darker black to frame 73 brighter white. The distance between each standing wave measured from this experiment was found 185 μm.

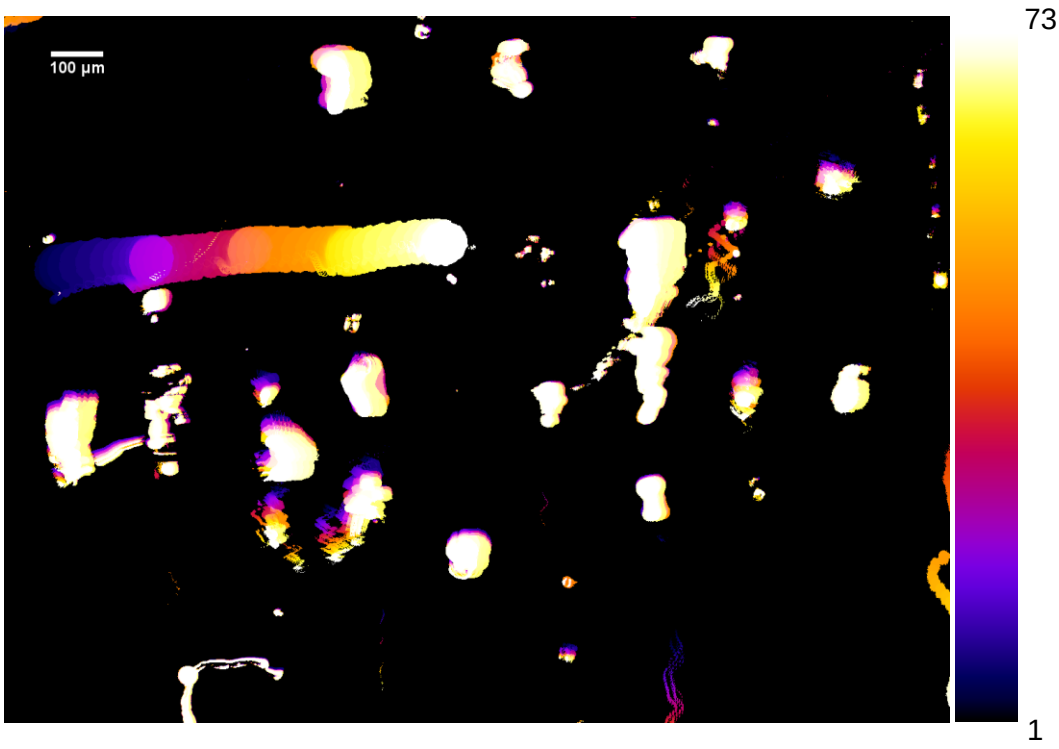

Figure 5.15 Hyperstack of images of experimental results for sorting DRG cells from myelin debris in a heterogeneous medium.

As it is readily observed from Figure 5.15, the porcine DRG cell is moving from its initial position to the right-hand side, leaving a trail with each different colour defining the frame in which the image was taken. On the other hand, the myelin debris are experiencing lower acoustic force, therefore they are not able to transport to the next node leaving no trace in the overlay picture meaning they were static for the duration of the experiment. The time between the frames was 0.5 sec, during t_{ramp} the average movement of the DRG cell was calculated to be 40 ± 1 μm/s. Figure 5.16 shows the displacement of the DRG neuron over time in comparison with the debris trace for this particular experiment.

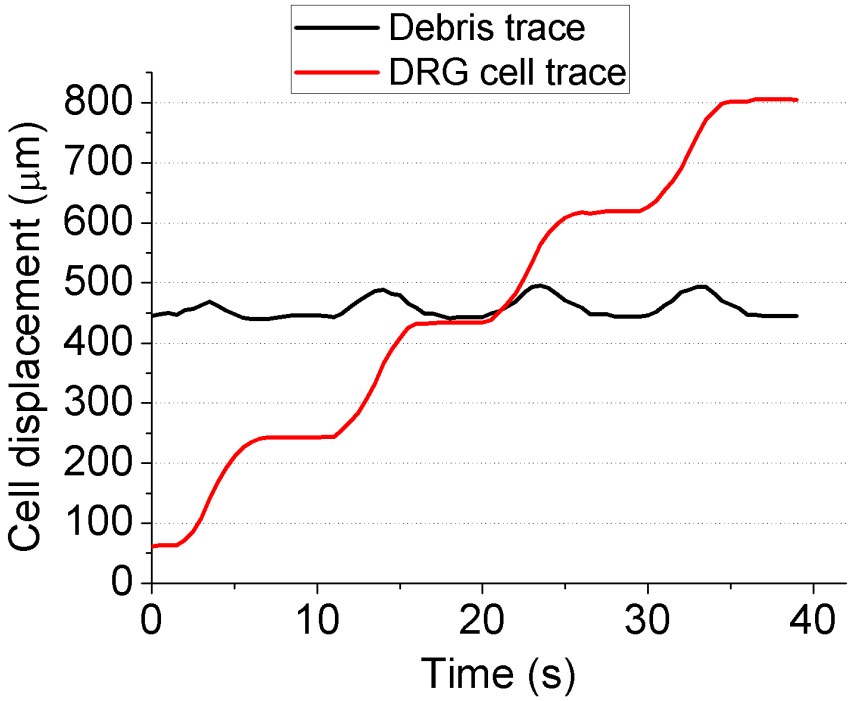

Figure 5.16 Graph showing the displacement of a DRG cell (red colour line) and a myelin debris (black colour line).

From Figure 5.16 it can be seen that the DRG cell is moving during the time t_{ramp} shown by the slope of the red line and then is settled during the t_{rest} time observed when the red line becomes parallel to the time axis.

In order to evaluate the experimental results, the efficiency, the purity and the final grade were calculated. For the experiment analysed above the efficiency was found to be 100 % since there is only one DRG cell which transports along with the phase shift of the field. While the purity was 100 %, since all the debris stayed at their original place after the completion of the DAF, which concludes to a total final grade of 100 %. The achieved final grade of this set of experiments proved the concept of the sorting capability of the DAF method on cells depending on their size, which provides a good starting point for future applications.

5.5 Sorting cells by stiffness

In this section, it is described how the separation ability of the DAF method regarding the density of particles can be used for real life sciences applications. After the successful experiments of sorting particles depending on their density, this work was taken to the next step by conducting experiments on cells with the goal to sort them regarding their mechanical properties and more specifically regarding their stiffness.

Firstly, the concept is supported by the contrast factor equation (3.18) which is included on the primary acoustic radiation force which is mainly used by the dynamic acoustic field. Secondly, for the implementation of this idea two populations of cells were required, which would have the same size but would have a difference between their stiffness properties. For this purpose, the first step of setting up the experiment was to mix two populations of live and dead cells, which would have the required similar size but would have a difference between their stiffness. The live cells were taken out of the flask on the day of the experiment, while the dead cells were prepared a few hours earlier by fixing the live cells. The fixation procedure made possible the change of the mechanical properties of the newly dead cells regarding their stiffness by keeping the same size in diameter as the live ones, which was the required property.

The cells used were Htert human tissue foreskin cells and the way to kill them was by fixation, the protocol for fixation is presented in Appendix A. The fixation was achieved by using a formaldehyde fixative solution, which allows the cells to remain in that state for almost a week. In order to determine the size of the two populations every time a new flask was prepared due to the growth of the cells that have covered more than 90 % of the available area on the flask, which is called passage, several images were taken and then the average cell size was measured using Fiji/imageJ software. The technique that was followed in order to measure the size of the cells is described. After the image was taken using the Zeiss Axiophot microscope, it was inserted into the ImageJ software and then it was converted into a binary image. Afterwards the option “fill holes” under the section “binary” was activated and the option “watershed” was activated if needed when two cells were touching each other so as to separate them, as shown in Figure 5.17 with the scale bar indicating 100μm. The next step for extracting the required measurements was to select the “analyse results” option and activate the “area measurement”, which provided the file containing all the information for each cell and also an image of the outline of the cells, an example is given in Figure 5.18. The results are summarised and displayed in the graph, produced in Excel (Figure 5.19), which shows the average cell size on each passage of live cells (solid fill) and dead cells (patterned fill).

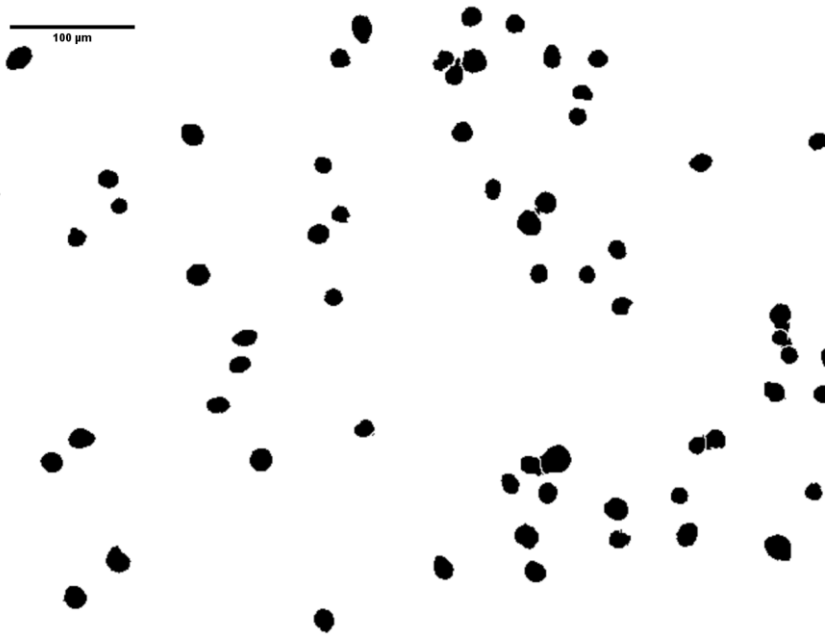

Figure 5.17 Binary processed image of cells.

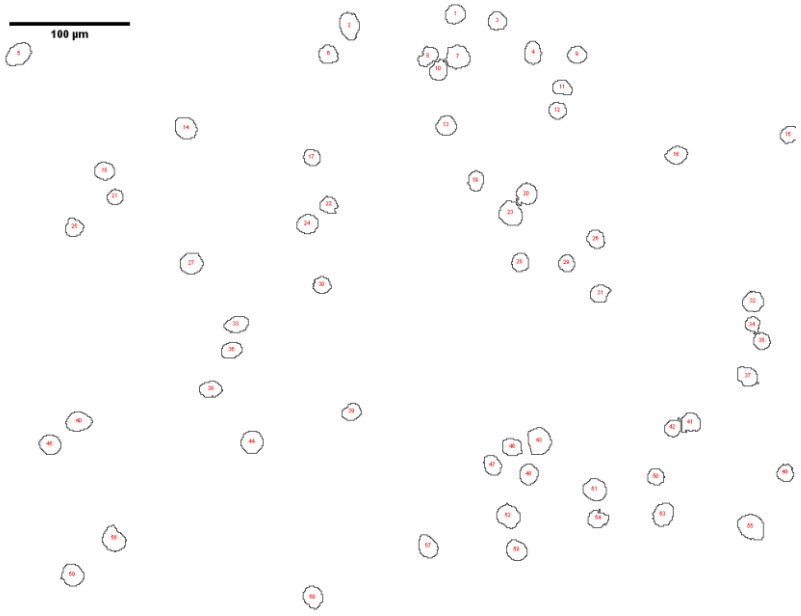

Figure 5.18 Processed image of cells outlined.

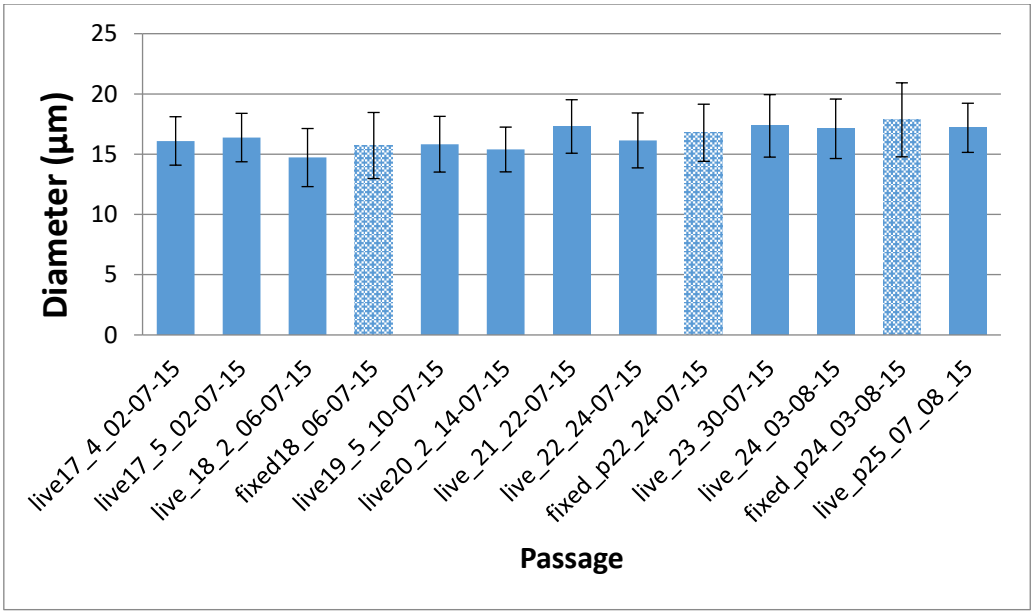

Figure 5.19 Cell size of live and dead cells in each passage.

From the graph in Figure 5.19, it is readily obtained that the fixed cells become slightly larger in diameter than the unfixed cells of the same passage, simply by comparing the fixed labelled population to the previous live labelled population since they are in chronological order.

Once the fixation of the cells was completed, it was necessary to determine the stiffness and density of the live-unfixed and the dead-fixed cells. Thus, a set of Atomic Force Microscopy (AFM) measurements was scheduled to take place, in order to determine the difference of the stiffness between the two different populations of cells. The AFM microscope used was the JPK Nanowizard 3. The technique that had to be followed in order to make new cantilevers for the purpose of this experiment, was to mount a round bead on a tip-less cantilever so as the cell would not get attached on the tip, allowing a set of measurements of the stiffness of the cells to happen [186]. The graph in Figure 5.20 shows a set of 64 measurements performed on a fixed cell providing a measurement of the Young's Modulus of that particular cell. The tool for analysing the results is the "JPKSPM data Processing", which used a round bead approximation for calculating the Young's modulus of the cell and provided a fitted curve of the distribution of the collected data (blue colour line in the graph). The mean value of Young's Modulus for the specific cell was found to be equal to $\overline{E} = 2.021$ kPa with a standard deviation equal to *sd* = 294.8 Pa. The same measurements were performed for the unfixed cells.

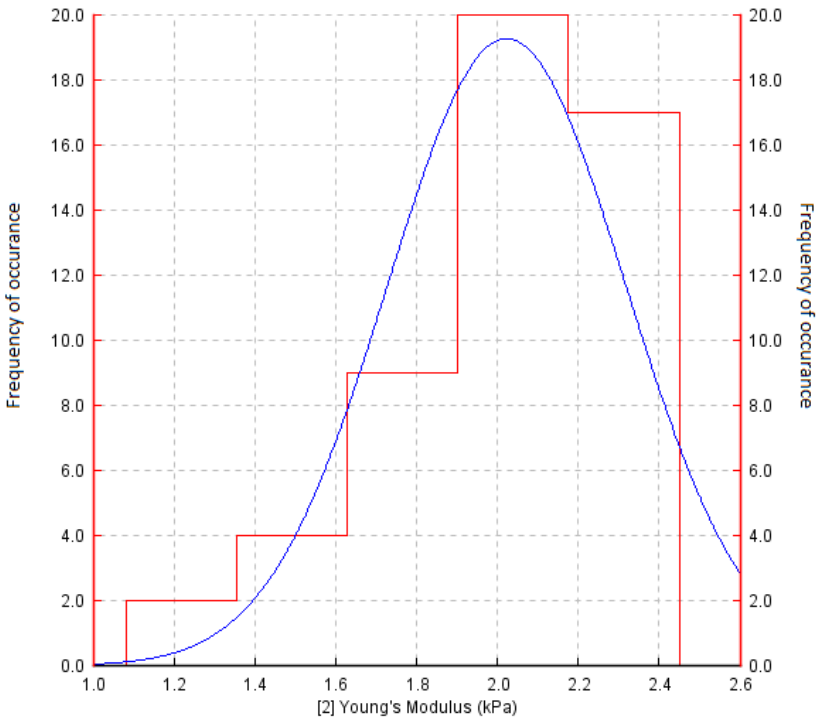

Figure 5.20 Young's Modulus for 64 measurements of one fixed cell.

The size of both populations live and dead cells was measured on the day of the experiment using ImageJ software as described earlier and their diameter found equal to 17.9 μm ± 3.2 μm for the fixed cells, while the unfixed-live cells found of diameter equal to 17.05 μm ± 2.08 μm.

In order to evaluate those results, more measurements are required, consequently for each type of cells fixed and unfixed, the measurements were repeated for 10 cells. The summarised results of the AFM measurements of the Young's Modulus for live and dead cells are displayed in the graph of Figure 5.21, which shows the distributed young's modulus of each population compared to the other. The medium on which the cells were inside during the AFM measurements was the CO_2 independent medium, which is the same as the medium used for the sorting experiments.

As it is easily obtained from the Figure 5.21, the unfixed cells (red bars) have been measured of smaller Young's Modulus in comparison with the fixed cells (blue bars). This means that the dead cells are stiffer (higher Young's Modulus) than the live cells. This verifies the capability of the concept for sorting such cells and shows the desired difference between the cell's stiffness. The average value of Young's Modulus of each population was, 1.89 ± 0.51

kPa for the set of the fixed cells, while for the unfixed cells was found to be 0.67 ± 0.18 kPa.

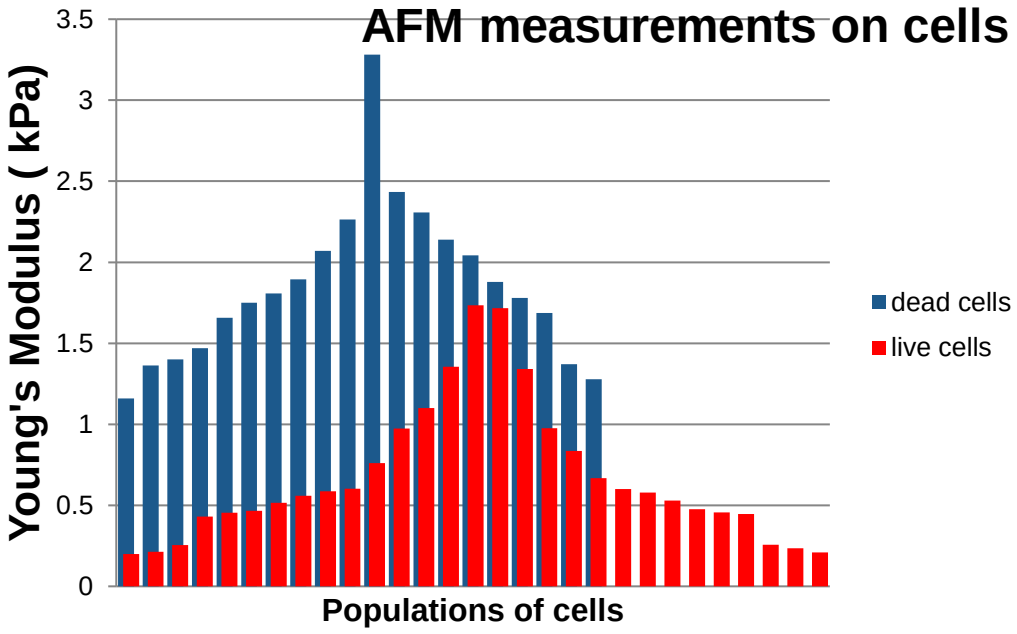

Figure 5.21 Compared results of Young's Modulus of fixed and unfixed cells.

As a next step, by performing an in depth examination of the equation of the contrast factor, equation (3.18), the density of the cells before and after the fixation was taken into consideration. The density measurements took place in the Centre for Cell Engineering (CCE). The technique used is called Percoll gradient density centrifugation; the whole technique relied on introducing liquids of different densities in a universal tube, in this work by inserting different percentage of Percoll into a NaCl solution, it would make layers of different densities close to the density of the cells. Afterwards the cells were added right on top of the layer with the lowest density. The highest density used which would go on the bottom of the tube was 1060 kg/m^3 and the lowest was set at 1020 kg/m^3. Figure 5.22 illustrates the experimental setup. The next step was the centrifugation of the aforementioned tube, during which the cells were centrifuged and travelled through the density layers until they would reach the layer of their own density. If the cells sank down to the bottom of the tube it meant that they were denser than the Percoll densities used. If they have stayed on top of the solution that meant that the cells were lighter than the Percoll densities used in the experiment. The results of the density of the unfixed cells found to be lighter than 32.5% of Percoll which gives a density of 1048 kg/m^3 and heavier than the 26% of Percoll which gives 1040 kg/m^3. That means the unfixed-

live Htert cells have a density between 1040 kg/m^3 and 1048 kg/m^3. Whereas, the results of the fixed cells density found the majority of the population inside the 32.5% Percoll solution which means that the density of the fixed cells lies around 1048 kg/m^3. The density experiments were repeated 5 times to verify the initial results. The Table 5.3 summarises the results of the size, the density and the stiffness measurements of the fixed and the unfixed cells.

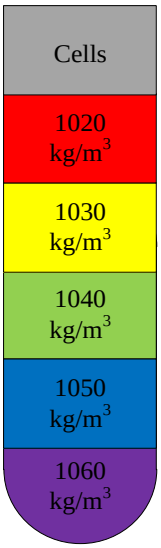

Figure 5.22 Experimental setup for density experiment.

Table 5.3 Results of the size the density and the stiffness of the fixed and unfixed cells

	Size (μm)	Density (kg/m^3)	Young's Modulus (kPa)
Fixed/dead cells in CO_2 independent medium	17.9 ± 3.2	1048 ± 4	1.89 ± 0.51
Unfixed/live cells in CO_2	17.05 ± 2.08	$1040 \leq \rho_c \leq 1048$	0.67 ± 0.18

The experimental setup for this experiment was set to V= 8Vp-p and the frequency of the input signal was set to f = 4.2MHz. The time of t_1 for this experiment was chosen to be 0.5 sec using 9 sequential steps of 40 degrees increment between each step until reaching the 360 degrees of one total phase shift, which gives the final time of t_{ramp} equal to 4.5 sec. The time of t_{rest} was chosen equal to 2.5 sec. By using these settings, the dynamic acoustic field was applied and

the results are demonstrated in the graph of Figure 5.23, showing the displacement of the dead Htert cell over time in comparison with live Htert cell for this particular experiment.

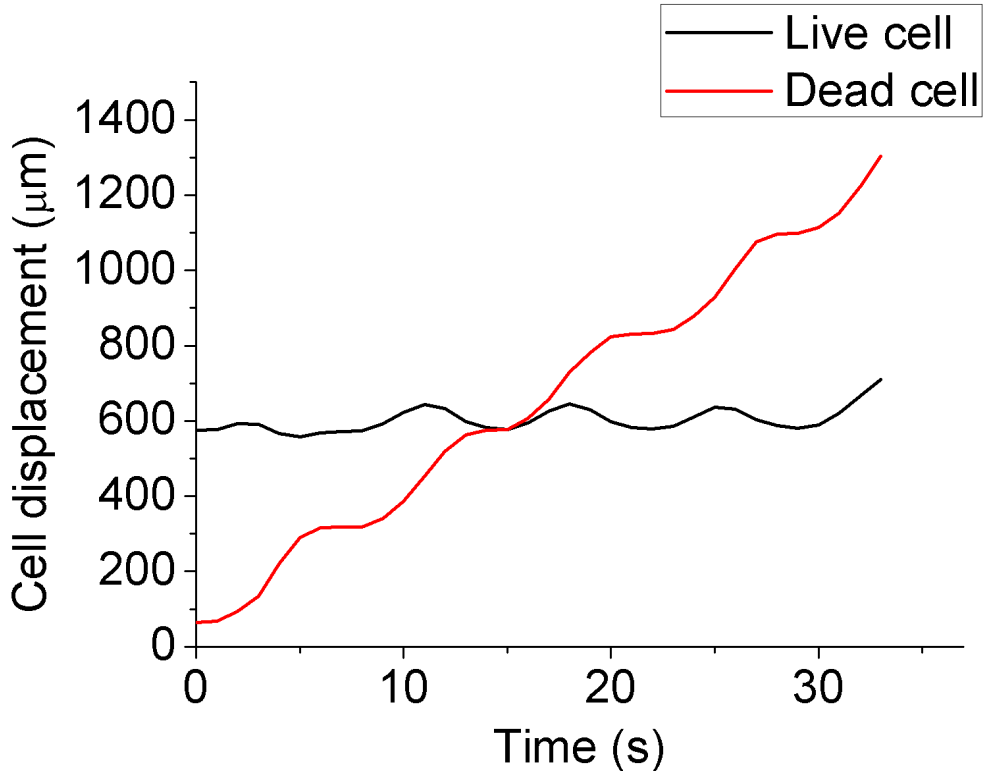

Figure 5.23 Graph showing the displacement of a dead Htert cell (red colour line) and a live Htert cell (black colour line).

From the graph above it can be seen that the dead cell is moving during the time of t_{ramp} shown by the slope of the red line and then settling during the t_{rest} time observed when the red line becomes parallel to the time axis. On the other hand, the live cell cannot transport to the next node and returns back to the original position. The figures of merit of the efficiency, purity and the final grade were measured at 72%, 63% and 67.5, respectively.

5.6 Summary and conclusions

In this chapter the experimental setup using the BAW device for sorting particles and cells by implementing the DAF method was presented. Experimental results of sorting particles depending on their size were demonstrated. More specifically, sorting 45 μm from 10 μm polystyrene particles was achieved with purity and efficiency figures of merit reaching 100 %, sorting 10 μm from 6 μm polystyrene particles was achieved with efficiency and purity reaching 97.3 % and 85.1 %, respectively, sorting 10 μm from 8 μm polystyrene particles was achieved with efficiency and purity reaching 96 % and 64 %, respectively, sorting 6 μm from

5 μm polystyrene particles was achieved with efficiency and purity reaching 90.5 % and 50 %, respectively. Furthermore, the capability of the proposed method for sorting particles depending on their density was verified by the demonstrated experimental results. In addition, experimental results were presented for translating the proposed method to real life applications, by achieving sorting of porcine DRG neuron cells in a heterogeneous mixture containing myelin debris and other non-neuronal cells. Measurements of dead and live cells stiffness were demonstrated. Experimental results for sorting cells depending on their stiffness by using the DAF method were presented.

As a conclusion it can be outlined that the proposed method's capability of sorting particles and cells over long distances has been verified. A perfect sorting can be achieved if the difference of the size of the particles is large enough, as presented in the case of the 45 μm and 10 μm particle sorting experiment. However, when the difference between the particles' diameter was getting smaller, the efficiency and the purity of the sorting capability was getting lower as well. That was concluded by the experimental results, highlighted by the fact that sorting of only 1μm difference between the diameter of the two populations was achieved, but the purity of the targeted sample was only 50 %. Moreover, the demonstrated results of the cell sorting capability of the DAF method establishes the groundwork for future applications that would take this work a step further. Last but not least, the proposed method can achieve sorting of particles and cells depending on their density using the same device of the size sorting experiments, which demonstrates an advantage of a versatile technique that can be applied without changing to a different device.

6. Experimental results using microfluidic SAW device

6.1 Introduction

This chapter presents the experimental results of sorting particles and cells using microfluidic Surface Acoustic Wave (SAW) devices. Initially, the experimental setup is presented, which was used throughout the entire process of the experiments. As a second step, the alignment of particles was implemented with a range of diameter from 1 to 10 μm, providing also the primary acoustic forces acting on them. Subsequently, two sets of experiments are presented showing the sorting capability of the device. The first one describes the sorting of particles of different diameter in a constant flow. The second set of experiments presents the sorting capability of cells of different stiffness in a constant flow, by sorting live from dead cells using the DAF method on a SAW device.

6.2 Experimental setup

The arbitrary waveform generator that was used for this experiment was a (TGA12104, Thurlby Thandar Instruments, UK), which drove the signal to each transducer and synchronised them, allowing independent control of the amplitude, phase and frequency of each channel. The signal then was amplified and driven through high-speed buffers, before being fed to the transducers via length matched coax cables. That step was important so that the signal would have the maximum amplification with the minimum distortion when arriving at each transducer. Thus, advantage of the maximum energy that the generator can provide was exploited. In order to control the signal generator a Labview code has been generated as described in section 4.3, by communicating through a general purpose interface bus (GPIB). Then the signal was driven in each transducer initially in phase in order to have the particles aligned under the effect of the standing waves that were formed. The microfluidic device was connected with tubes which were attached to syringes in its inlets in order to insert the volume of the particles/cells into the channel. The syringes were then attached on a syringe pump which allowed a steady continuous flow of particles or cells within the appropriate medium for each case. The device was then placed under an inverted microscope, providing the capability of taking images of the particles or cells in real time while conducting the experiment. Figure 6.1 illustrates what was described above.

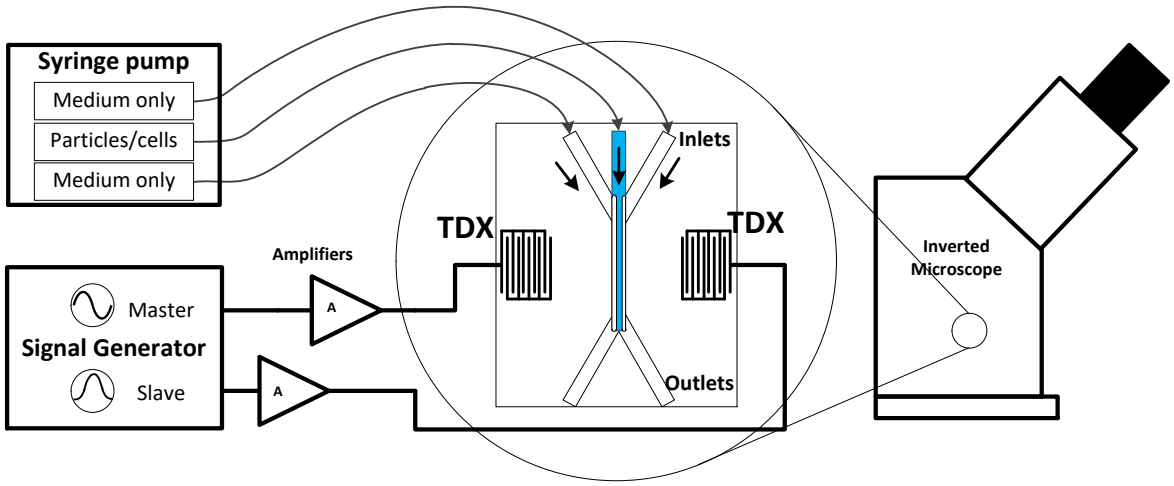

Figure 6.1 Experimental setup of sorting experiments using the SAW device.

In order to fit the tubes in the inlets and outlets of the PDMS microfluidic channel, 2 mm holes have been made by using a PDMS puncher, the inlet holes were through holes from top to the bottom, while the outlet holes were forming a 90-degree angle from the bottom so the tubes could be easily driven in the horizontal direction. Figure 6.2 illustrates the microfluidic channel with the inlets and outlets before it was bonded on the substrate.

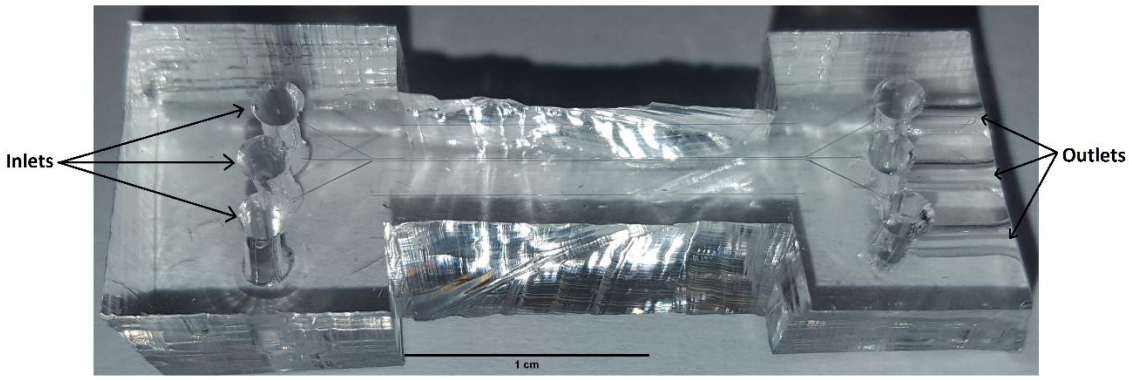

Figure 6.2 Microfluidic channel of PDMS with inlets and outlets.

During the design and fabrication of the microfluidic channels a lot of different designs have been tested. Initially only one inlet was in use for the injection of the particles and cells inside the channel and two outlets for the collection of the two populations. By using this combination of inlets and outlets a variety of the channel width has been tested; 200 μm, 400 μm and 600 μm width channels. For a 20 MHz SAW device the SAW wavelength (λ) is equal to λ=199.5 μm, due to the fact that the SAW velocity of the chosen direction of the transmission on the

substrate is equal to 3990 m/s. Since each standing wave is away from the next one by a distance of $\lambda/2$ = 99.75 μm, those channels would fit 2, 4 and 6 standing waves, respectively. Although, a very good alignment and sorting has been achieved using these channels, the need to collect the particles and cells at the outputs imposed the fabrication of a channel of width equal to 100 μm that would fit only one standing wave inside [187]. Figure 6.3 shows the particles getting stuck on the side walls, which drove the need of designing the microfluidic channel with two extra inlets, for having a sheath flow which eliminates the effect of particles getting close to the edges of the channel. The optimised inlets would have 30° angle between each other [116], [188], as shown in Figure 6.4. Despite the fact that the problem of the particles going on the edges was solved, another problem was encountered. The majority of both populations were concentrated in the middle of the channel. Thus, while approaching the two outlets the particles were equally flowing through both of the outlets, which compromised the purity results. Consequently, the design of the channel changed to three outputs instead of two, providing the solution of the smaller particles going through the middle and bottom outlet, while the large particles were following the phase shift and released through the top outlet. The bonding of the channel on top of the substrate was performed by hand, and the distance between each standing wave is of the order of micrometres. Thus, a small change to the initial phase of one of the transducers to the appropriate amount for each case was needed in order to achieve the position of the standing wave to be on the centre of the channel.

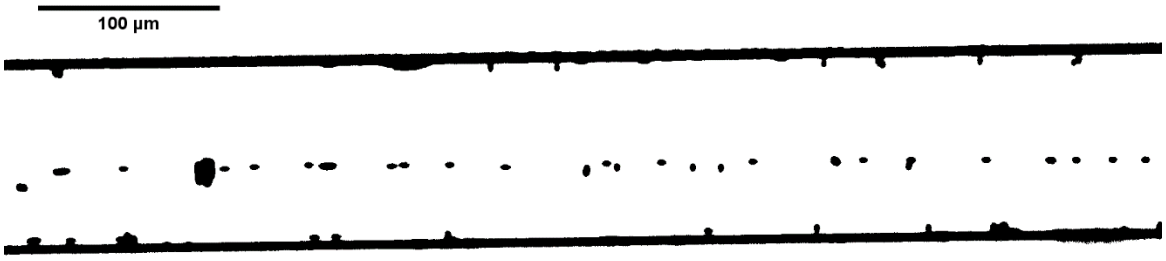

Figure 6.3 100 μm microfluidic channel with no sheath flow.

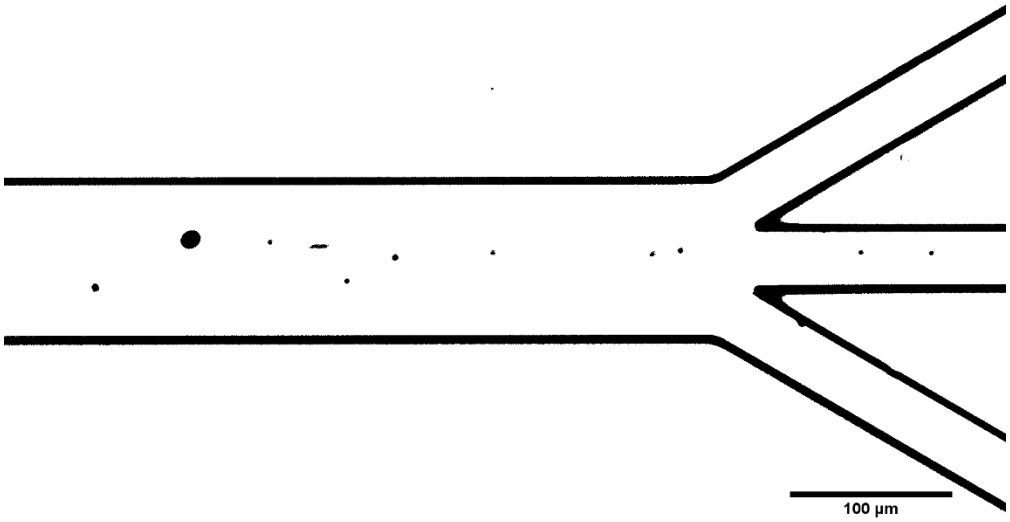

Figure 6.4 Image of microfluidic channel using sheath flow.

6.3 Alignment of 1, 3, 6 and 10 µm particles

The initial designed experiment was the alignment of particles of different diameter inside the microfluidic channel during the excitation of both of the transducers in phase. The particles tested were of 1, 3, 6 and10 µm in diameter and the results are demonstrated in the following images. For the alignment of 1 µm particles, a 600 µm channel was used, the voltage driven to each transducer through the amplifiers was set to 40Vp-p. The flow rate of the particles inside the channel was set at 2 µl/min. All the particle details are given in Apendix A. The purpose of this experiment was to verify the correct operation of the device and determine the limits of the device regarding how small diameter particles it can acoustically trap at the nodes.

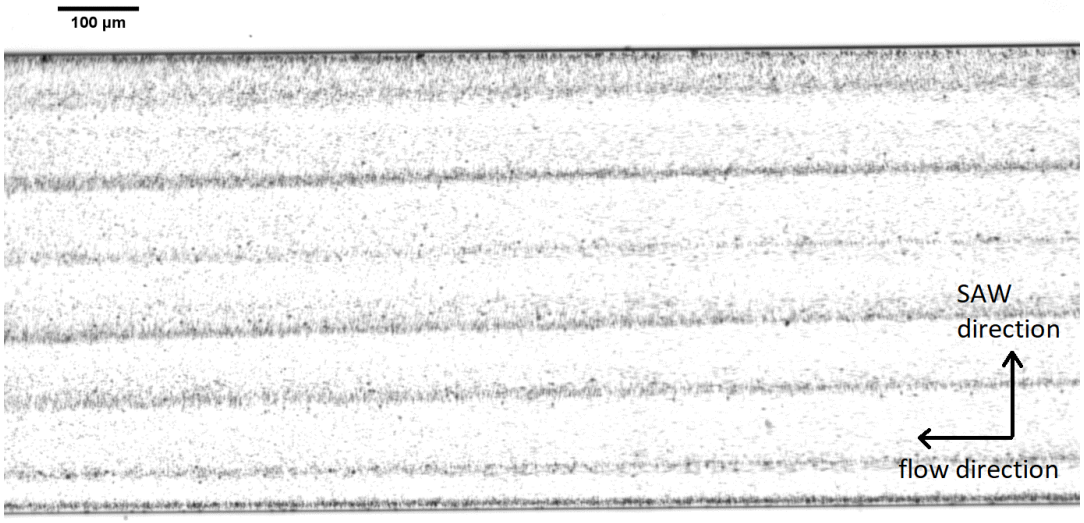

Figure 6.5 Alignment of 1 µm particles in a 600 µm microfluidic channel.

The image in Figure 6.5 was captured using the x5 Hamamatsu lens at 100 μm per 145 pixels. As it is readily obtained, the 1 μm particles are mostly concentrated at the nodes but there are still many of them flowing around the nodal positions, providing the essential information of the capabilities of this device in terms of how small diameter particles can align.

The purpose of the alignment of the rest of the particles of 3, 6 and 10 μm in diameter was concentrated on finding the applied forces of the field on the particles regarding their diameter. In order to estimate the magnitude of the acoustic pressure applied to the different diameter of particles, the time taken for the particles to agglomerate at the nodes was measured, starting from a randomly distributed state of motion. These experiments were repeated five times at five different locations within the device using time-lapse microscopy. The drag force, F_d, derived from the dimensions and density of the particles as well as the viscosity of the medium, equation (3.20) (see section 3.6), allows the acoustic pressure amplitude acting on the particles to be calculated. Those values were found to be $(6.33\pm0.67)\times10^5$ Pa, $(2.47\pm0.64)\times10^5$ Pa, $(1.84\pm0.41)\times10^5$ Pa and $(0.88\pm0.23)\times10^5$ Pa for 1 μm, 3 μm, 6 μm and 10 μm diameter polystyrene particles, respectively.

6.4 Sorting particles by size

This section describes the ability of the proposed method using the SAW device of sorting particles of different diameter. As a starting point for the proof of concept sorting experiments 10 μm particles from 3 μm particles in a homogeneous medium inside a microfluidic channel were conducted. The followed procedure and the results are summarised in section 6.4.1.

During the experiments the frequency of the transducers used was set to 20.00 MHz with the amplitude of the signal set to a range of 30 to 36 Vp-p. At this frequency, the wavelength of the sound waves on the substrate was λ = 199.5 μm (the velocity of sound on $LiNbO_3$ at the direction of emission is 3990 m/s) [189]. Each standing wave is formed at a distance of $\lambda/2$ = 99.75 μm from the previous one, where the particles agglomerate at the nodes under the acoustic pressure acting on them. In order to eliminate the problem of the particles sinking to the bottom of the syringe, a percentage of 30% histodenz density gradient solution was introduced to the particle mixture so as to levitate the particles at the appropriate height in the middle of the syringe, so that the particles could exit from the syringe while the flow pump was working. Before the insertion of the particles inside the microfluidic channel, the channel was treated with 1% bovine serum albumin (BSA) coating [190] for 30 minutes which made the

surface of the substrate hydrophobic and also the sidewalls of the PDMS microfluidic channel, thus avoiding the particles getting stuck on the edges of the channel or the substrate.

6.4.1 Sorting 10 and 3 μm particles in a flow

For the separation experiments that were performed, a mixture of particles of the two populations was used. The particle density of the 10 μm and 3 μm polystyrene particles was 9.1 x 10^6 particles/ml and 1.68 x 10^8 particles/ml, respectively. The ratio of the mixture of the 10 μm and 3 μm particles was 1:18. There was no aggregation of particles observed at this concentration. The time variant acoustic field was able to transport, and at the same time, separate particles according to their size inside a microfluidic channel using a constant flow as shown in Figure 6.6 from the right-hand side to the left. For this experiment, a ratio of 40% of the 30% histodenz density gradient and 60% of the medium with particles has been used. Hence, avoiding the particles sinking to the bottom of the syringe before they were even introduced inside the tubes. In order to keep the same density of the mixture, the syringes that feed the sheath flow inlets were diluted with 40% of the 30% histodenz density gradient and 60% of the medium as well.

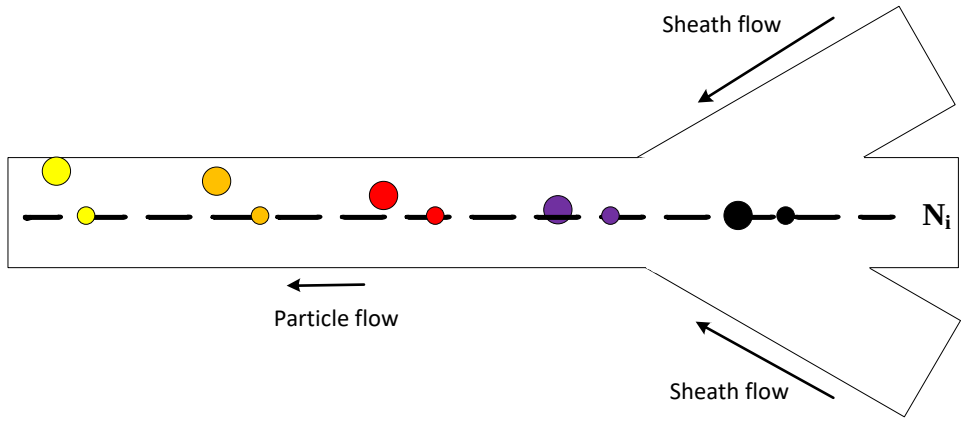

Figure 6.6 Expected position of the particles as a function of time (represented by colour).

Figure 6.6 shows the expected behaviour of the large and small particles over time, with the different colours representing a time interval in relation with the initial position of the node indicated by Ni of the acoustic landscape, (black is equal to t_0, purple t_1, red t_2, orange t_3 and yellow t_4). Larger particles are moving at the direction of the phase shift, thus getting separated from the initial mixture while aligned at the nodal line. Whereas, the smaller particles in size experience less force and consequently they cannot travel past the nodal position.

The image in Figure 6.7 shows particle traces as function of time (110 frames covering 25.7 s) in a hyperstack of images as they have been collected out of an experiment with the parameters of t_{ramp} set at 5.8 sec and t_{rest} equal to 1.6 sec. The colour time scale bar shows the change from frame 1 darker black to frame 110 brighter white. As it is readily observed the 10 μm diameter polystyrene particles follow the shifted acoustic field meaning they are moving from the nodal line to the top side of the channel and exiting from the top outlet. While the 3 μm diameter polystyrene particles stay close to the position of the original node, by experiencing less forces than the larger particles, thus exiting form the middle and bottom outlets of the microfluidic channel. The flow rate used for this experiment was set at 1μl/min, with the direction of the particles shown from the right-hand side to the left. The program that was used in order to capture all the images is the HCImage live of Hamamatsu, the objective lens used for this experiment was the x10 Hamamatsu lens at 100 μm per 290 pixels and the frames taken per second were 4.27 fps.

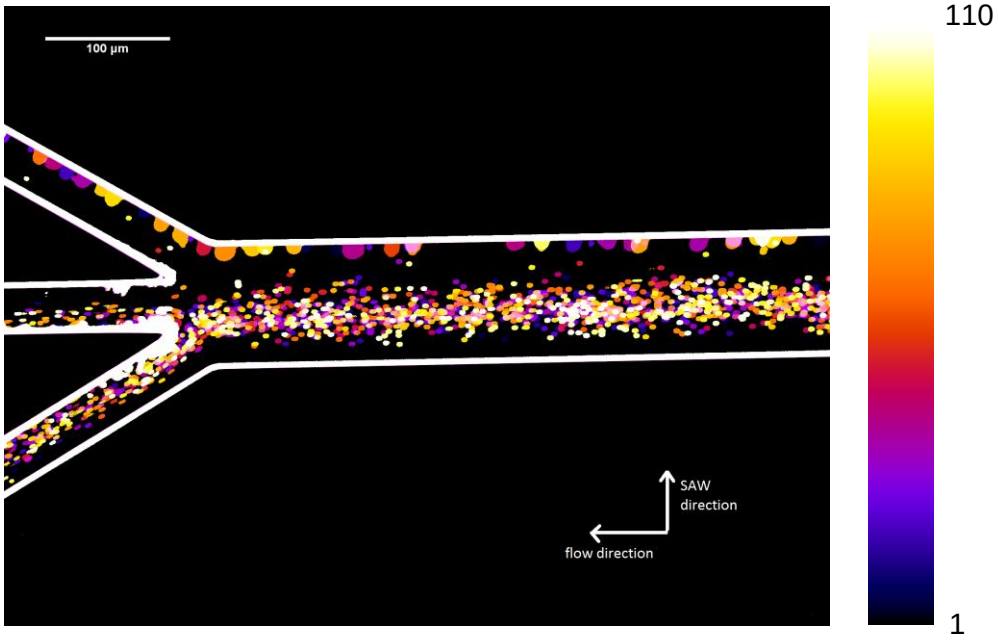

Figure 6.7 Experimental results for sorting 10 and 3 μm particles in a flow using a SAW device.

The efficiency of this experiment was calculated equal to 100 %, since all the large particles are getting separated from the smaller ones and leave the channel from the top outlet. While, the purity was calculated at 71.7 %, providing a final grade of 85.85 %.

6.5 Sorting live from dead cells in a flow

In this section, it is described how the ability of the DAF method for sorting cells regarding their stiffness can be used for real life sciences applications, by using the SAW device introduced earlier. After the successful experiments of sorting particles depending on their size, the next step was to conduct experiments on cells with the goal to sort them regarding their mechanical properties and more specifically regarding their stiffness.

The cells used were the Htert human tissue foreskin that have already been used for the experiments in section 5.5, thus all the appropriate size, stiffness and density measurements of each population taken, apply for this set of experiments as well. The fixation procedure remained the same as described in section 5.5. For the separation experiments that were performed, a mixture of the two populations of cells (live and dead) was used. The cell concentration of the dead/fixed cells and of the live/unfixed cells was 3.5 x 10^4 cells/ml and 6.2 x 10^4 cells/ml, respectively. The ratio of the mixture of the dead and live cells was 1:1.77. There was no aggregation of cells observed at this concentration. The time variant acoustic field was able to transport, and at the same time, separate cells according to their stiffness in a microfluidic channel using a SAW device as shown in Figure 6.8. Live cells are represented with green colour while the stiffer dead cells are represented with red colour.

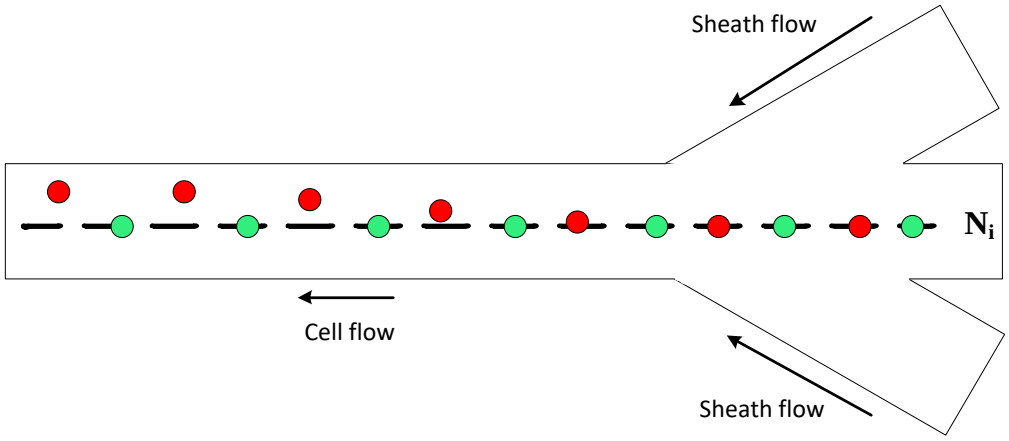

Figure 6.8 Expected position of live and dead cells as a function of time in a microfluidic channel using a SAW device.

The experimental setup for the specific experiment displayed here is described as follows. The frequency of operation of the transducers used was set to 19.77 MHz. At this frequency the wavelength of the sound waves on the substrate is equal to λ = 201.8 μm, thus, each standing

wave is formed at a distance of $\lambda/2$ = 100.9 μm achieving the desired one standing wave inside the channel. The input amplitude used for this experiment for both transducers, before it was fed to the amplifiers was set to V_{in}= 0.4 Vp-p and after the application of the amplifiers output signal had a value equal to V_{out}= 31 Vp-p. Subsequently, each signal was fed to the transducers as the input signal. In order to achieve the position of the standing wave to be at the centre of the channel the initial phase of the slave channel was set at φ_{slv} = 50º. The parameters of the phase shift were set at t_{ramp} = 2.7 sec and t_{rest} = 0.7 sec. The flow rate was set at 0.2 μl/min. The channel was treated with BSA as described in the previous section. The medium that the cells were suspended in for this experiment was the CO_2 independent medium. The usage of 60% CO_2 medium and 40% of 30% Histodenz has been applied in both the sheath flow inlets and the main cell flow inlet. The image in Figure 6.9 shows a stack of images of the experimental results of sorting cells depending on their stiffness properties. The traces of the dead/fixed cells are displayed with a red colour, while the traces of the live/unfixed cells are represented with a green colour. The direction of the flow is from the right to the left-hand side.

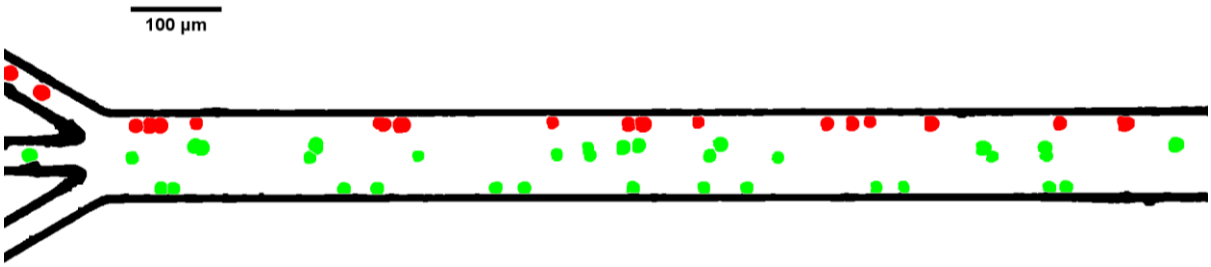

Figure 6.9 Experimental results of sorting cells depending on their stiffness properties, in a constant flow using the DAF method with a SAW device, the green and red colour indicate the live/unfixed cells and dead/fixed cells, respectively.

The objective lens used for this experiment was the x5 Hamamatsu lens which corresponds to 100 μm per 145 pixels. The time between each frame was 4.77 s. During this experiment it was not possible to image both populations at the same time, because different filters had to be used in order to image the two different populations. Figure 6.9 was constructed by imaging first the live cells using the filter for detecting the green fluorescent (shown in green colour) which were stained using the live/dead stain kit. It can be concluded that the live cells were exiting only from the bottom and middle outputs but never from the top one. The second stage of the construction of Figure 6.9, was to use the normal filter of the microscope for detection of any object, observing cells going out of all the outlets top, middle and bottom. Therefore, the assumption was made that only dead cells are exiting from the top outlet.

6.6 Summary and conclusions

In this chapter the experimental setup using the DAF method with the SAW device for sorting particles and cells was presented. Experimental results of focusing and sorting particles depending on their size were demonstrated. More specifically for the focusing experiments alignment of particles of 1 μm, 3 μm, 6 μm and 10 μm diameter was achieved in a constant flow. Experimental results were demonstrated of the DAF method using the SAW device of sorting 10 μm from 3 μm polystyrene particles in a constant flow inside a microfluidic channel. Sorting experiments were conducted of dead from live cells in a constant flow.

The conclusions of this set of experiments are that the DAF method can be applied also in a SAW device and successfully sort particles depending on their size. For the cell sorting experiments relating to cell stiffness, the experiments showed that the acoustic manipulation technique could demonstrate that this cell sorting was possible, providing encouraging initial results for future work. If simultaneous imaging of both populations could be achieved, then a better understanding of the DAF method on this type of sorting would be available for examination.

7. Dynamic Acoustic Rotating Field

7.1 Principle of operation

A new idea for sorting particles different than the already proposed DAF method is the Dynamic Acoustic Rotating Field (DARF). The name came from the acoustic field that is newly formed every time when a pair of transducers is excited alternately one after the other. Due to their position the acoustic field appears to be rotating. The principle of operation is very similar to the one that was described in section 4.1. Consequently, every time two opposing transducers are excited, particles and cells are aligned under the acoustic pressure field acting on them due to the formed standing waves. The basic concept of this idea is to place two pairs of opposing transducers in such way so they form a cross and then excite each pair alternately as shown in Figure 7.1. This would lead to sorting larger particles in diameter from smaller. Larger particles would experience much higher forces and they would follow the acoustic field faster than the smaller, thus if not allowing enough time for the small ones to follow, by changing to the next pair of transducers, the smaller particles would stay in place and the larger would move again closer to the nodes.

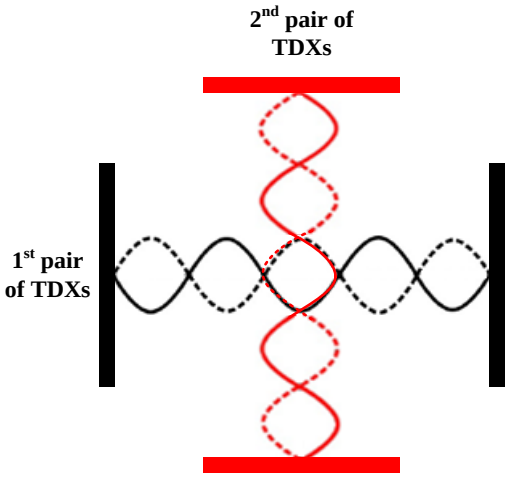

Figure 7.1 Schematic illustration of two pairs of opposing transducers and their wave excitation forming standing waves.

This technique is based on the time between the change from the first pair of transducers to the next pair and on how many repeats are following. By selecting these two factors, particle sorting depending on size can be achieved. The same effect can be achieved with three pairs of transducers with the third pair finding its place in the diagonal in between the two other pairs.

7.2 Acoustic separation simulations

What was described above has been simulated with the WaveDyn program. Figure 7.2 shows the result from the simulation under the effect of two switching pairs of transducers. Two different types of particles were simulated, 10 μm and 3 μm, for 0.5 sec for every repeat, for several repeats. All the particle details are given in Apendix A.

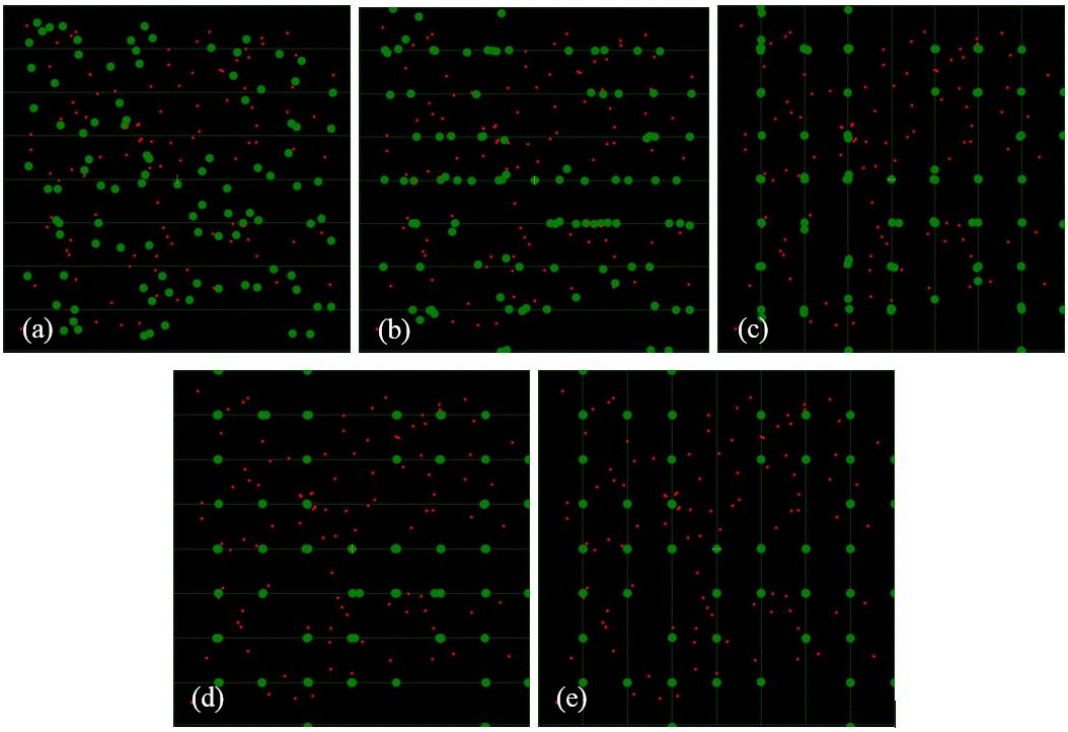

Figure 7.2 Simulation results for the behaviour of the rotating field over time (a) Initial position (b) effect of first pair (c) effect of the second pair (d) effect of the first pair again (e) end of run with the effect of the second pair again.

As it is shown in Figure 7.2(a), at the initial point the particles are randomly distributed. Although, as the time passes and the pairs of the TDXs are alternately excited, the large particles are getting trapped in the nodes, while the small ones cannot follow because the time is too short for them to get under the effect of the acoustic field as shown in Figures 7.2(b), 7.2(c), 7.2(d) and 7.2(e). The reason for this is because the acoustic forces acting on a smaller particle are weaker than on a larger one, which influence the velocity of the particle, thus if the time between the switching is fast enough it does not allow the small particles to move. The most important parameters in this case are the voltage applied and the duration of excitation of each pair of transducers before the next switching to the next pair.

Similar results can be obtained under the effect of three pairs of transducers. Figure 7.3 demonstrates the result of the simulation of three pairs of transducers under the application of the DARF method, at the initial point shown in Figure 7.3(a) and at the end of the run Figure 7.3(b). The difference between using two or three pairs of transducers is the acquired pattern on the active region of operation. In the case of the 2 pairs of TDXs square patterns can be observed, while in the case of the three pairs of TDXs hexagon patterns are detected.

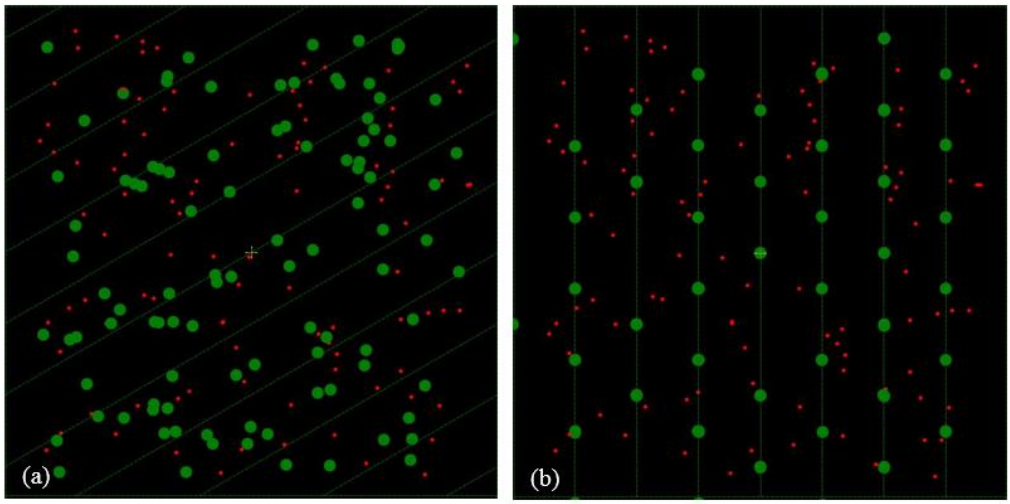

Figure 7.3 Simulation results for the behaviour of the rotating field using 3 pairs of transducers over time (a) Initial position (b) end of run.

7.3 Experimental results of the DARF method using two pairs of transducers

For the purposes of this set of experiments, the experimental setup used was the same as the one described in section 5.1. The differences on the execution of the experiment were, by using the same octagon shaped device, two pairs of TDXs were used instead of utilising only one pair. In order to achieve this, a splitter was attached to each channel of the generator, providing the exact same signal properties in each TDX of the pair. Figure 7.4 illustrates the experimental setup that was used. The Labview code used to control the signal generator has been modified in order to be able to switch off and on the channels on demand at the required time.

During the experiments the frequency of the transducers used was set to f = 4.00 MHz with the amplitude of the signal set at V_{in} = 1.2 Vp-p, which after the amplification was V_{out} = 8 Vp-p on each transducer. At this frequency, the wavelength of the sound waves in water is λ = 370 μm (the velocity of sound in water is 1480 m/s). Each standing wave is formed at a

distance of λ/2 = 185 μm, from the previous one, where the particles agglomerate at the nodes under the acoustic pressure acting on them.

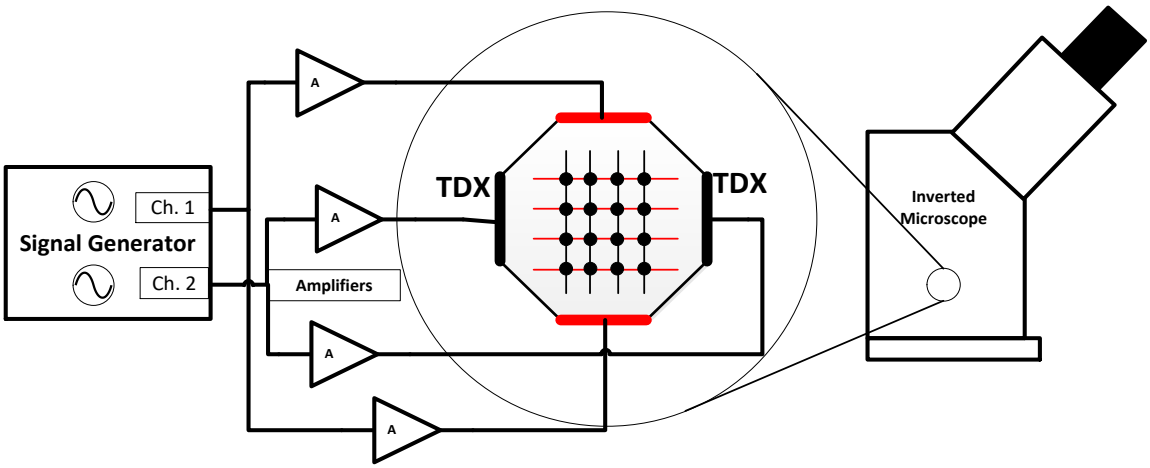

Figure 7.4 Experimental setup using the BAW device for applying the DARF method using 2 pairs of transducers.

Figure 7.5 demonstrates the results of the effect of the rotating field with the use of two pairs of opposing transducers. A hyperstack of images analysed from the free software Fiji (Image J) is displayed. The polystyrene particles that were used in this experiment had diameter of 10 μm and 3 μm and for this particular experiment. The duration of the excitation of each pair was set to 0.5 seconds and the repeats were 30 for each pair, which concludes to 60 repeats in total.

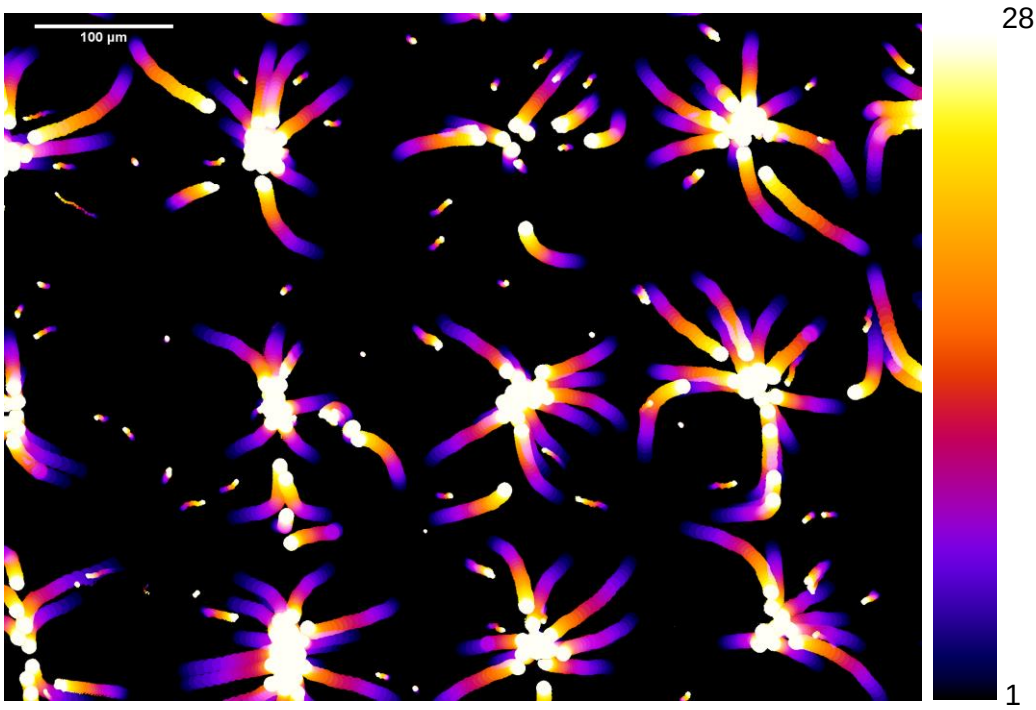

Figure 7.5 Experimental results of the DARF using two pairs of transducers for sorting particles of diameter 10 µm and 3 µm.

As it can be observed, the larger particles 10 µm follow the rotating acoustic field, while the 3 µm diameter particles stay close to their initial position. The objective lens used for this experiment was the x10 Hamamatsu lens which corresponds to 100 µm per 290 pixels, the time between each frame was 1 s. The experimental results of the particle sorting using the DARF method follow exactly the behaviour of the simulation results which described earlier in section 7.2. The efficiency of this experiment was calculated at 92.2 % and the purity was calculated at 93 %, providing a final grade of 92.6 %.

7.4 Experimental results of the DARF method using three pairs of transducers

For the purposes of this set of experiments, the experimental setup used was the same as the one described in section 7.3. The differences on the execution of the experiment were, by using the same octagon shaped device, three pairs of TDXs were used instead of utilising two pairs. Figure 7.6 illustrates the experimental setup that was used.

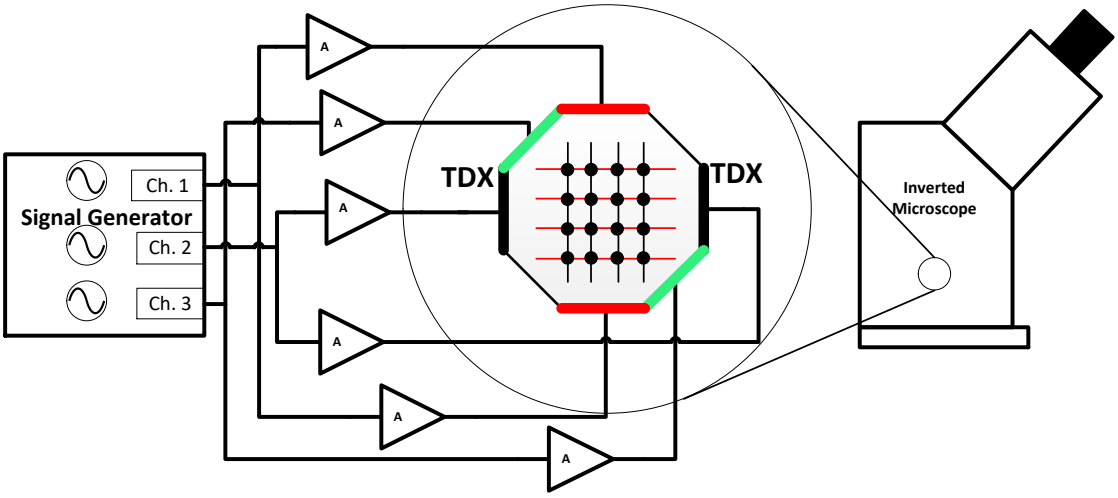

Figure 7.6 Experimental setup using the BAW device for applying the DARF method utilising 3 pairs of transducers.

Figure 7.7 demonstrates the results of the effect of the rotating field with the usage of three pairs of opposing transducers. A hyperstack of images analysed from the free software Fiji (Image J) is displayed. The polystyrene particles that were used in this experiment had diameter of 10 μm and 3 μm. For this particular experiment the duration of the excitation of each pair was set to 0.75 seconds and the repeats were 49 for each pair, which concludes to 98 repeats in total.

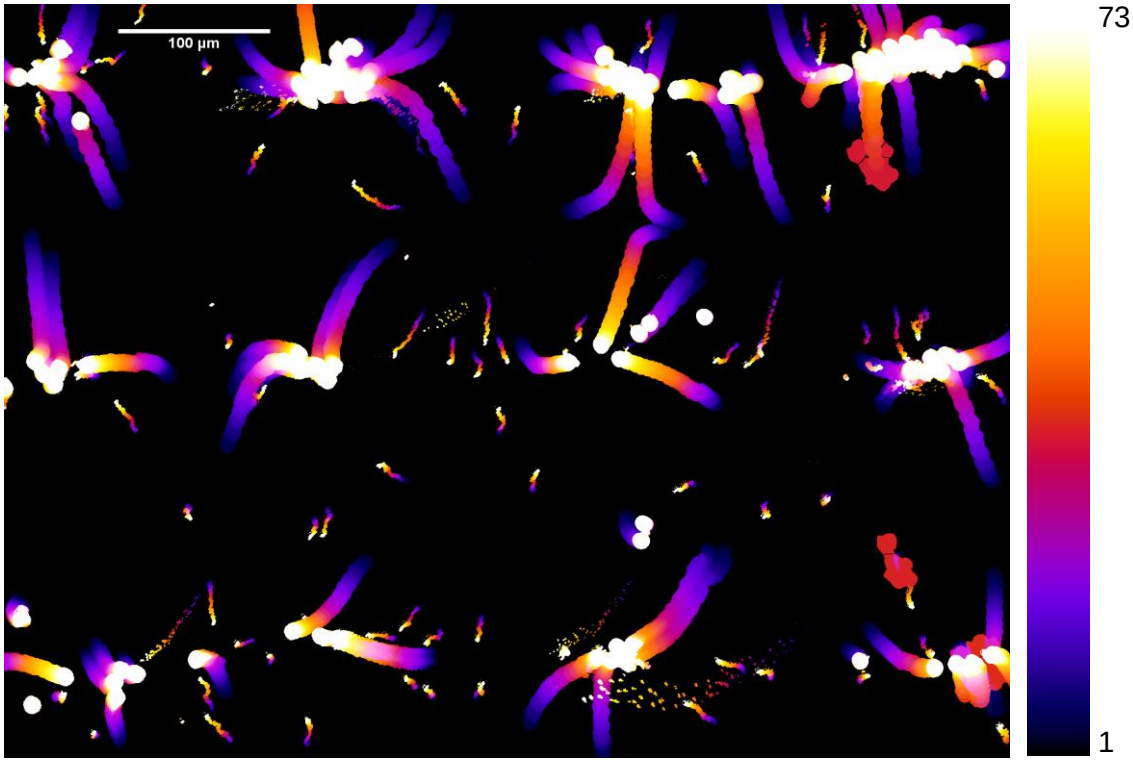

Figure 7.7 Experimental results of the DARF using three pairs of transducers for sorting particles of diameter 10 µm from 3 µm.

The objective lens used for this experiment was the x10 Hamamatsu lens which corresponds to 100 µm per 290 pixels, the time between each frame was 1 s. The experimental results show a good similarity compared to the simulation results described in section 7.2. The efficiency of this experiment was calculated at 87 % and the purity was calculated at 81.2 %, providing a final grade of 84.1 %.

7.5 Summary and conclusions

In this chapter a novel acoustic manipulation method of particles and cells was presented. The principle of operation of the dynamic acoustic rotating field by continuously change the excited pair of the opposing transducers was demonstrated. Acoustic separation simulations were presented in order to demonstrate the ability of the proposed method to sort particles and cells depending on their size. The experimental setup using the BAW device for sorting particles and cells by applying the DARF method was presented. Experimental results of sorting polystyrene particles of diameter 10 µm from 3 µm were demonstrated by using the DARF method with two different setups. The first setup demonstrated was by using two pairs of opposing transducers and the second setup was by using three pairs of transducers for applying the DARF method.

As a conclusion the DARF method was tested under the simulations and then verified by experiments. The comparison between the experimental results and the simulations was outstanding. Finally the proof of concept was established. Both setups worked really well but the setup using two pairs of TDXs was the most promising for future work since it can provide the sorting result faster than the 3 pair setup. An application for this technique could be used in cell cultures were the growth of the cells of interest should be in a specific pattern. Alternatively, the growth of the targeted cells or bacteria would need to be isolated from other smaller cells.

8. Conclusions and future work

In this final chapter of this thesis a conclusion of the undertaken research of this work is demonstrated. This thesis was focused on the development of ultrasonic manipulation methods of particles and cells. By using two devices for acoustophoretic manipulation, BAW and SAW devices, the sorting of particles and cells was achieved. The performance of the novel method proposed in this work is discussed and compared to other particle manipulation approaches. The outcomes are concluded here.

The ultrasonic manipulation technology as described in Chapter 2, compared to other technologies used for particle and cell manipulation has demonstrated great capabilities and flexibility in analytical chemistry and biological applications. Advantages of this technology include versatility, low cost and easy microfluidic system integration. Furthermore, the advantage of preservation of cell viability and the generation of appropriate forces to handle cells of sizes up to tens of microns was described.

A novel acoustic manipulation method of particles and cells was presented in Chapter 4. The principle of operation of the DAF method was to continuously change the phase of one of the opposing transducers in order to translate the acoustic field that was formed. The acoustic simulations produced to demonstrate the sorting capability of the proposed method were presented. There were two types of performed simulations, one for sorting particles due to their size difference and one for sorting depending on their density difference. The results of both simulations were very promising. The advantages of using the DAF method are summarised by the shearless, label-free and low damage characteristics that make this method of manipulation particularly suited for biological applications. Including its inherent safety and biocompatibility and the opportunity to operate over large distances at the scale of 1-2 cm.

The design and fabrication of the BAW device was based on the preliminary work completed by A.L Bernassau, where a PZT transducer was placed in each side of an octagon shaped cavity. Thus, any problems or difficulties that may have occurred through the fabrication process of the materials or the methods were already solved. A new device with the same expected properties was fabricated to demonstrate the repeatability of the method through the device. The characterisation of the opposing IDTs to be used for this type of device showed a very good match and a good frequency response. As a conclusion a robust device that could apply the DAF method was ready to be used.

The experimental setup using the BAW device was demonstrated and the DAF method has been put under test by conducting sorting experiments of particles of different diameter. Experimental results of sorting 45 μm from 10 μm polystyrene particles were demonstrated to achieve efficiency and purity of 100 %, sorting 10 μm from 6 μm polystyrene particles was achieved with efficiency and purity reaching 97.2 % and 97 %, respectively, sorting 10 μm from 8 μm polystyrene particles was achieved with efficiency and purity reaching 96 % and 64 %, respectively, sorting 6 μm from 5 μm polystyrene particles was achieved with efficiency and purity reaching 90.5 % and 50 %, respectively. The proposed method's capability of sorting particles and cells over long distances has been verified. Leading to the conclusion of a perfect sorting presented in the case of the 45 μm and 10 μm particle sorting experiment. Sorting particles of lower size difference has been achieved, although, when the difference between the particles' diameter was getting lower, the efficiency and the purity of the sorting capability was getting reduced as well. The lowest difference of particle diameter sorting achieved was of 1μm difference. By translating the capability of the DAF method to biological applications, successful experiments were conducted for sorting cells of different size. The conclusions made were that cells can be sorted regarding their size with the maximum of efficiency and purity using the DAF method. Dead cells have different stiffness from live cells which was verified by experiments and cells of different stiffness can by sorted by using the DAF method.

The design and fabrication of the SAW device was based on conventional techniques described in the literature, using a $LiNbO_3$ substrate. Two different fabricating techniques were followed for the construction of the IDTs. Using the electron beam lithography tools for testing the pattern of the written IDTs and once it was concluded a chrome mask containing the desired patterns was produced for using the photolithography technique. Both techniques were successful with the photolithography technique being slightly easier, less complicated and faster, though the electron beam lithography technique was more accurate in terms of alignment.

The methods of the fabricated microfluidic channels were presented accompanied with the bonding technique of the channel on top of the substrate in order to fabricate a throughput SAW device. The first step towards the fabrication of the microfluidic channel was to produce an SU8 mould that could host the PDMS for making the channel. The challenges of making the SU8 mould were mostly dependant on the behaviour of the material. Thus, in order to achieve the desired thickness of the channel, the spinning and baking times of SU8 were thoroughly

investigated. Also a challenging factor of this fabrication, was to achieve steep slopes of the sidewalls, which were mostly dependant on the exposure time under the UV light during the photolithography process for writing the pattern on the SU8. A challenge was encountered regarding the bonding of the PDMS channel on the substrate, as bonding was performed by hand and there was a small time window for the bond to be made after the O_2 plasma procedure. The alignment of the microfluidic channel was an issue, misaligned devices needed to be cleaned and bonded again. The identified solution was to put a drop of methanol on top of the substrate right before the bond was made, allowing enough time for the alignment to happen without preventing the bond to happen. The initial design of the microfluidic channel had one inlet and two outlets. Although, driven by the experimental results a sheath flow had to be added to stop particles from getting stuck on the sidewalls, while an extra outlet was added for achieving better efficiency and purity ratios.

The experimental setup using the SAW device was demonstrated and the DAF method has been put under test by conducting sorting experiments of particles of different diameter in a constant flow. Experimental results of focusing depending on the particle size were demonstrated, by aligning particles of 1 μm, 3 μm, 6 μm and 10 μm diameter in a constant flow. Moreover, experimental results of sorting 10 μm from 3 μm polystyrene particles in a throughput utilising the DAF method on the SAW device were demonstrated. The experimental results were successful, reaching an efficiency of 100% and purity of 71.7% and verified the correct function of the proposed method by collecting the sorted populations from different outlets. Experimental results for sorting cells in a constant flow depending on their stiffness properties were demonstrated. The conclusion made was that the dead (stiffer) cells were following the translated acoustic field. Also, it was concluded that the live cells were behaving as expected, meaning they could not follow the translation of the acoustic field but it was not possible to determine if there was any contamination of the purity of the results. For further/future work, it is suggested to solve these imaging problems and verify the proof of the concept of sorting cells of different stiffness by using the DAF method.

Lastly, a novel approach of sorting particles and cells depending on their size properties was proposed. The principle of operation of the dynamic acoustic rotating field was demonstrated by continuously switching between the excited pairs of the opposing transducers. Acoustic separation simulations were presented, with the use of two and three pairs of opposing transducers in order to demonstrate the ability of the proposed DARF method to sort particles

and cells depending on their size. The simulation results concluded that the proposed method could be used in order to sort particles and cells regarding their size.

Experimental results of sorting polystyrene particles of diameter 10 μm from 3 μm were demonstrated by using the DARF method with two different setups. The first setup demonstrated used two pairs of opposing transducers and the second setup was by using three pairs of transducers. The experimental results were successful, verifying the concept of the DARF method, concluding to a remarkably good correlation to the simulations, with efficiency and purity reaching 92.2 % and 93 %, respectively. Considering that the proof of concept has been established, for future research more experiments are recommended to be taken using different sets of particles in diameters, translate the concept to biological cells and examine further the time and repetitions of the switching of the pairs in order to map the parameter landscape and determine the limitations of the device and method. Moreover, a way of collecting the sorted particles and cells should be further explored to demonstrate the ability of translating this method to real life applications.

Appendix A

The details of the polystyrene particle, used for the experiments of Chapters 5, 6 and 7 are demonstrated here, as given by the supplier:

Density = 1.05g/cm3

Hazards: Harmless-use normal precautions

1) Nominal Reference Values:
45.0µm mean diameter
2.5% solids (w/v) aqueous suspension Coefficient of Variance (CV): 10% Crosslinked with divinylbenzene
4.99 x 105 particles/ml

2) Nominal Reference Values
25um particles
1.1 x 107 particles/ml

3) Nominal Reference Values:
10.0µm mean diameter
2.5% solids (w/v) aqueous suspension Coefficient of Variance (CV): 10% Crosslinked with divinylbenzene
4.55 x 107 particles/ml

4) Monodisperse Polystyrene
8.13um SD=0.12um
10% w/v aqueous suspension, CV 1.4%
3.4x108 particles/ml

5) Nominal Reference Values:
6.00µm mean diameter
2.5% solids (w/v) aqueous suspension Coefficient of Variance (CV): 10%
2.10 x 108 particles/ml

6) Nominal Reference Values:

3.00µm mean diameter

2.5% solids (w/v) aqueous suspension Coefficient of Variance (CV): 5%

1.68 x 109 particles/ml

Cell culture protocol of H-tert that was followed:

1. Switch on the sterile cabinet and swab down with 70% ethanol.

2. Warm up the DMEM media, hepes saline and trypsin/versene in 37 ºC water bath.

3. Remove the media from the flask and gently rinse once with 5ml of Hepes Saline and discard.

4. Add 5 ml of trypsin/versene (20ml versene + 0.5 ml trypsin) to flask.

5. Check periodically under the microscope to ensure cells are getting detached. While cells are detaching syringe filter DMEM media.

6. Add 5 ml filtered DMEM media to flask and gently shake.

7. Remove cell suspension into a sterile plastic universal tube and pipette a few times.

8. Centrifuge at 1400 rpm for 4 min.

9. Once centrifuge has stopped, pour off media from cell pellet and resuspend cells in 5 ml of media to give a single cell suspension.

10. Perform cell count using haemocytometer.

11. Add 0.25 ml -0.5 ml cells to flask depending on how confluent the cells need to be for the next passage.

Fixation protocol of the cells that was followed:

1. Trypsinise cells as normal until there is a cell pellet.

2. Suspend in media (with FBS).

3. Leave for 30 min to recover (with gentle agitation).

4. Centrifuge cells using 1000rpm for 3 min and suspend in PBS.

5 Mix 1:1 with 8% formaldehyde fixation solution (a stock was made in advance of 40ml PBS, 2g sucrose and 10ml of 37% formaldehyde).

6. Leave for 15 min.

7. Centrifuge fixed cells using 1000rpm for 3 min

8. Suspend in PBS with 1mM Tris.

9. Shake for 30 min.

10. Centrifuge and suspend in PBS.

11 Centrifuge and suspend in PBS.

12. These cells are ready as fixed cells. They can be kept for a week in the fridge.

Matlab source code for simulation graphs for applied acoustic forces based on size and density of the particles.

```
Array_j = zeros(1,10);
Array_i = zeros(1,10);
Array_ij = zeros(10,10);

i = 10;
for j=1:1:10
   Array_j(j) = i^2 + 5*j + 3;
end
j = 10;
for i=1:1:10
   Array_i(i) = i^2 + 5*j + 3;
end
for j=1:1:10
   for i=1:1:10
      Array_ij(j,i) = i^2 + 5*j + 3;
   end
end
v=253.15065e-6;      %% change this value (velosity)

viscwater=1e-3;
denswater=1000;

speedbead=1962;
densbead=1055;

Fa_d= zeros(1,18);
Fa_pc= zeros(1,26);
Fa_d_pc=zeros(1,10);

speedwater=1480;   %speed of sound in water

freq=4e6;   %operating frequency

lambda=speedwater/freq;     %wavelength of the sound

constg=9.81;   %gravity

po=22274; % max pressure amplitude


%speedbead=1962;

for d= 3:1:40 ; % diameter of particles in um % this will change from 3 to 20 with step 1
   for pc= 1:1:3000;
test_beadradius=(d*10^(-6))/2;
```

```
beadvol= (4/3)*pi*test_beadradius^3;

Vc = beadvol;



k=2*pi/lambda;
compbead=1/(densbead*speedbead^2);   % compressability
compwater=1/(denswater*speedwater^2);

bc = compbead;  %compressibility of the particle

bw =  compwater; %compressibility of the medium

pw = 1000;  % dencity of the surrounding medium in this case water

cfactor= (5*pc-2*pw)/(2*pc+pw)-(bc/bw);%The accoustic contrast factor

%  Calculate the acoustic forces
Fa_d_pc(d,pc)=((pi*po^2*Vc*bw)/lambda)*cfactor;
end;


end;
```

References

[1] D.-H. Kim *et al.*, “High-throughput cell manipulation using ultrasound fields,” in *Annual International Conference of the IEEE Engineering in Medicine and Biology Society*, 2004, vol. 4, pp. 2571–2574.

[2] E. S. Douglas, R. a Chandra, C. R. Bertozzi, R. a Mathies, and M. B. Francis, “Self-assembled cellular microarrays patterned using DNA barcodes,” *Lab Chip*, vol. 7, no. 11, pp. 1442–8, Nov. 2007.

[3] J. M. Dziedzic and T. Yamane A. Ashkin, “Optical trapping and manipulation of single cells using infrared laser beams,” *Nature*, vol. 330, pp. 769–771, 1987.

[4] P. Y. Chiou, A. T. Ohta, and M. C. Wu, “Massively parallel manipulation of single cells and microparticles using optical images,” *Nature*, vol. 436, no. 7049, pp. 370–372, Jul. 2005.

[5] H. Lee, Y. Liu, D. Ham, and R. M. Westervelt, “Integrated cell manipulation system-CMOS/microfluidic hybrid,” *Lab Chip*, vol. 7, no. 3, pp. 331–337, Mar. 2007.

[6] T.-H. Wang, Y. Peng, C. Zhang, P. K. Wong, and C.-M. Ho, “Single-molecule tracing on a fluidic microchip for quantitative detection of low-abundance nucleic acids,” *J. Am. Chem. Soc.*, vol. 127, no. 15, pp. 5354–5359, Apr. 2005.

[7] S. Kawata and T. Sugiura, “Movement of micrometer-sized particles in the evanescent field of a laser beam,” *Opt. Lett.*, vol. 17, no. 11, pp. 772–774, 1992.

[8] A. Azioune, M. Storch, M. Bornens, M. Théry, and M. Piel, “Simple and rapid process for single cell micro-patterning,” *Lab Chip*, vol. 9, no. 11, pp. 1640–1642, Jun. 2009.

[9] W. T. Coakley, D. W. Bardsley, M. A. Grundy, F. Zamani, and D. J. Clarke, “Cell manipulation in ultrasonic standing wave fields,” *J. Chem. Technol. Biotechnol.*, vol. 44, no. 1, pp. 43–62, 1989.

[10] Y. Liu and K.-M. Lim, “Particle separation in microfluidics using a switching ultrasonic field,” *Lab Chip*, vol. 11, no. 18, pp. 3167–3173, Oct. 2011.

[11] M. Eisenstein, “Cell sorting: Divide and conquer,” *Nature*, vol. 441, pp. 1179–1185, 2006.

[12] A. Haake, A. Neild, G. Radziwill, and J. Dual, “Positioning, displacement, and localization of cells using ultrasonic forces,” *Biotechnol. Bioeng.*, vol. 92, no. 1, pp. 8–14, Oct. 2005.

[13] P. R. Rogers, J. R. Friend, and L. Y. Yeo, “Exploitation of surface acoustic waves to drive size-dependent microparticle concentration within a droplet,” *Lab Chip*, vol. 10, no. 21, pp. 2979–2985, 2010.

[14] P. Li *et al.*, “Acoustic separation of circulating tumor cells,” *Proc. Natl. Acad. Sci.*, vol.

112, no. 16, pp. 4970–4975, Apr. 2015.

[15] K. W. Kwon *et al.*, “Label-free, microfluidic separation and enrichment of human breast cancer cells by adhesion difference,” *Lab Chip*, vol. 7, no. 11, pp. 1461–8, Nov. 2007.

[16] T. Franke, S. Braunmüller, T. Frommelt, and A. Wixforth, “Sorting of solid and soft objects in vortices driven by surface acoustic waves,” in *Proc. of SPIE*, 2009, vol. 7365, p. 73650O1-9.

[17] T. Laurell, F. Petersson, and A. Nilsson, “Chip integrated strategies for acoustic separation and manipulation of cells and particles,” *Chem. Soc. Rev.*, vol. 36, no. 3, pp. 492–506, Mar. 2007.

[18] F. Petersson, A. Nilsson, C. Holm, H. Jonsson, and T. Laurell, “Separation of lipids from blood utilizing ultrasonic standing waves in microfluidic channels,” *Analyst*, vol. 129, no. 10, pp. 938–43, Oct. 2004.

[19] J. J. Hawkes, R. W. Barber, R. Emerson, and W. T. Coakley, “Continuous cell washing and mixing driven by an ultrasound standing wave within a microfluidic channel,” *Lab Chip*, vol. 4, pp. 446–452, 2004.

[20] P. Augustsson, L. B. Åberg, A.-M. K. Swärd-Nilsson, and T. Laurell, “Buffer medium exchange in continuous cell and particle streams using ultrasonic standing wave focusing,” *Microchim. Acta*, vol. 164, no. 3, pp. 269–277, 2009.

[21] A. L. Bernassau, F. Gesellchen, P. G. A. Macpherson, M. Riehle, and D. R. S. Cumming, “Direct patterning of mammalian cells in an ultrasonic heptagon stencil,” *Biomed. Microdevices*, vol. 14, no. 3, pp. 559–64, Jun. 2012.

[22] J. Lee *et al.*, “Targeted cell immobilization by ultrasound microbeam,” *Biotechnol. Bioeng.*, vol. 108, no. 7, pp. 1643–1650, 2011.

[23] P. Glynne-Jones *et al.*, “Multi-modal particle manipulator to enhance bead-based bioassays,” *Ultrasonics*, vol. 50, no. 2, pp. 235–239, 2010.

[24] M. Wiklund and H. M. Hertz, “Ultrasonic enhancement of bead-based bioaffinity assays,” *Lab Chip*, vol. 6, no. 10, pp. 1279–1292, 2006.

[25] D. Bazou, W. T. Coakley, A. J. Hayes, and S. K. Jackson, “Long-term viability and proliferation of alginate-encapsulated 3-D HepG2 aggregates formed in an ultrasound trap,” *Toxicol. Vitr.*, vol. 22, no. 5, pp. 1321–1331, 2008.

[26] H. Jönsson, C. Holm, A. Nilsson, F. Petersson, P. Johnsson, and T. Laurell, “Particle separation using ultrasound can radically reduce embolic load to brain after cardiac surgery,” *Ann. Thorac. Surg.*, vol. 78, no. 5, pp. 1572–1577, 2004.

[27] A. L. Bernassau, C. R. P. Courtney, J. Beeley, B. W. Drinkwater, and D. R. S. Cumming, “Interactive manipulation of microparticles in an octagonal sonotweezer,” *Appl. Phys. Lett.*, vol. 102, no. 16, p. 164101, 2013.

[28] M. Dziubinski, “Hydrodynamic Focusing in Microfluidic Devices,” in *Advances in Microfluidics*, 2012, pp. 29–54.

[29] M. Yang, C. Li, and J. Yang, “Cell Docking and On-Chip Monitoring of Cellular Reactions with a Controlled Concentration Gradient on a Microfluidic Device,” vol. 74, no. 16, pp. 3991–4001, 2002.

[30] Y. Zhou *et al.*, “Sensors and Actuators B : Chemical A microfluidic platform for trapping , releasing and super-resolution imaging of single cells,” *Sensors Actuators B. Chem.*, vol. 232, pp. 680–691, 2016.

[31] K. Kim and O. A. Saleh, “A high-resolution magnetic tweezer for single-molecule measurements,” *Nucleic Acids Res.*, vol. 37, no. 20, pp. 1–7, 2009.

[32] S. Martel, C. C. Tremblay, S. Ngakeng, and G. Langlois, “Controlled manipulation and actuation of micro-objects with magnetotactic bacteria,” *Appl. Phys. Lett.*, vol. 89, no. 23, p. 233904, 2006.

[33] K. Ino, A. Ito, and H. Honda, “Cell Patterning Using Magnetite Nanoparticles and Magnetic Force,” vol. 97, no. 5, pp. 1309–1317, 2007.

[34] S. Grimnes and Ø. G. Martinsen, “Chapter 7 – Electrodes,” in *Bioimpedance and Bioelectricity Basics*, 2015, pp. 179–254.

[35] H. Morgan, M. P. Hughes, and N. G. Green, “Separation of submicron bioparticles by dielectrophoresis,” *Biophys. J.*, vol. 77, no. 1, pp. 516–525, 1999.

[36] G. R. Pesch, F. Du, M. Baune, and J. Thöming, “Influence of geometry and material of insulating posts on particle trapping using positive dielectrophoresis,” *J. Chromatogr. A*, vol. 1483, pp. 127–137, 2017.

[37] W.B.Kim, S.J.Lee, Y.J.Kim, E.S.Lee, “The electromechanical principle of electrorheological fluid-assisted polishing,” *Int. J. Mach. Tools Manuf.*, vol. 43, no. 1, pp. 81–88, Jan. 2003.

[38] J. Cebricos, R. Hoptowit, S. Jun, “Separation of Escherichia coli K12 from contaminated tap water using a single-stage, continuous flow dielectrophoresis (DEP) device,” *LWT - Food Sci. Technol.*, vol. 80, pp. 185–192, Jul. 2017.

[39] J. Tröndle, A. Ernst, W. Streule, R. Zengerle, P. Koltay, “Non-contact optical sensor to detect free flying droplets in the nanolitre range,” *Sensors Actuators A Phys.*, vol. 158, no. 2, pp. 254–262, Mar. 2010.

[40] T. N. G. Adams, A. Y. L. Jiang, P. D. Vyas, and L. A. Flanagan, “Separation of Neural Stem Cells by Whole Cell Membrane Capacitance using Dielectrophoresis,” *Methods*, 2017.

[41] H. Ralph, “Single particle characterization and manipulation by opposite field dielectrophoresis,” *J. Electrostat.*, vol. 56, pp. 435–447, 2002.

[42] A. Ashkin, “Acceleration and Trapping of Particles by Radiation Pressure,” *Phys. Rev. Lett.*, vol. 24, no. 4, pp. 156–159, Jan. 1970.

[43] A. Ashkin and J. M. Dziedzic, “Optical trapping and manipulation of viruses and bacteria,” *Science (80-.).*, vol. 235, no. 4795, pp. 1517–1520, Mar. 1987.

[44] C. Lin, A. Chen, and C. Lin, “Microfluidic cell counter / sorter utilizing multiple particle tracing technique and optically switching approach,” *Biomed. Microdevices*, vol. 10, no. 1, pp. 55–63, 2008.

[45] E. McLeod and A. Ozcan, “Nanofabrication using near-field optical probes,” *J Lab Autom.*, vol. 17, no. 4, pp. 248–254, 2012.

[46] A. D. Mehta, M. Rief, J. A. Spudich, D. A. Smith, and R. M. Simmons, “Single-Molecule biomechanics with optical methods,” *Science (80-.).*, vol. 283, no. 5408, pp. 1689–1695, 1999.

[47] D. S. Johnson, L. Bai, B. Y. Smith, S. S. Patel, and M. D. Wang, “Single-Molecule Studies Reveal Dynamics of DNA Unwinding by the Ring-Shaped T7 Helicase,” *Cell*, vol. 129, no. 7, pp. 1299–1309, 2007.

[48] J. K. Valley, A. T. Ohta, H.-Y. Hsu, S. L. Neale, A. Jamshidi, and M. C. Wu, “Optoelectronic Tweezers as a Tool for Parallel Single-Cell Manipulation and Stimulation,” *IEEE Trans Biomed Circuits Syst*, vol. 3, no. 6, pp. 424–431, 2009.

[49] A. Kundt, “Acoustic experiments,” *London, Edinburgh Dublin Philos. Mag. J. Sci.*, vol. 35, no. 4, pp. 41–48, 1868.

[50] Lord Rayleigh, “XLII. On the momentum and pressure of gaseous vibrations, and on the connexion with the virial theorem,” *Philos. Mag.*, vol. 10, no. 57, pp. 364–374, 1905.

[51] W. Altberg, “Uber die Druckkrafte der Schallwellen und die absolute Mes- sung der Schallintensitat (On the force due to sound waves and the absolute measurement of sound intensity),” *Ann. Phys.*, vol. 11, pp. 405–420, 1903.

[52] V. F. K. Bjerknes, “Fields of Force,” *Columbia Univ. Press.*, 1906.

[53] L. V. King, “On the acoustic radiation pressure on spheres.,” *Proc. R. Soc. Lond. A*, vol. 147, no. 861, pp. 212–240, 1934.

[54] K. Yosioka and Y. Kawasima, “Acoustic radiation pressure on a compressible sphere,” *Acta Acust. united with Acust.*, vol. 5, no. 3, pp. 167–173, 1955.

[55] L. Gor’kov, “On the forces acting on a small particle in an acoustical field in an ideal fluid,” *Sov. Physics-Doklady*, vol. 6, pp. 773–775, 1962.

[56] A. a. Doinikov, “On the radiation pressure on small spheres,” *J. Acoust. Soc. Am.*, vol. 100, no. 2, p. 1231, 1996.

[57] R. W. Wood and A. L. Loomis, “XXXVIII . The physical and biological effects of high-

frequency sound-waves of great intensity," *London, Edinburgh, Dublin Philos. Mag. J. Sci.*, vol. 4, pp. 417–436, 1927.

[58] A. P. Sarvazyan, O. V. Rudenko, and W. L. Nyborg, "Biomedical applications of radiation force of ultrasound: Historical roots and physical basis," *Ultrasound Med. Biol.*, vol. 36, no. 9, pp. 1379–1394, 2010.

[59] W. T. Richards, "An Intensity Gauge for 'Supersonic' Radiation in Liquids," *Proc. Natl. Acad. Sc.*, vol. 15, no. 4, pp. 310–314, 1929.

[60] J. Wu and G. Du, "Acoustic radiation force on a small compressible sphere in a focused beam," *J. Acoust. Soc. Am.*, vol. 87, no. 3, pp. 997–1003, Mar. 1990.

[61] R. M. Moroney, R. M. White, and R. T. Howe, "Fluid motion produced by ultrasonic Lamb waves," in *Ultrasonics Symposium*, 1990, pp. 355–358.

[62] M. Saito, S. Izumida, and J. Hirota, "Ultrasonic trapping of paramecia and estimation of their locomotive force," *Appl. Phys. Lett.*, vol. 71, no. 14, pp. 1909–1911, 1997.

[63] J. Hultström, O. Manneberg, K. Dopf, H. M. Hertz, H. Brismar, and M. Wiklund, "Proliferation and viability of adherent cells manipulated by standing-wave ultrasound in a microfluidic chip," *Ultrasound Med. Biol.*, vol. 33, no. 1, pp. 145–151, 2007.

[64] F. Beyeler *et al.*, "Monolithically Fabricated Microgripper With Integrated Force Sensor for Manipulating Microobjects and Biological Cells Aligned in an Ultrasonic Field," *Journal of Microelectromechanical Systems*, vol. 16, no. 1. pp. 7–15, 2007.

[65] S. K. and V. K. and V. Steinberg, "Continuous particle size separation and size sorting using ultrasound in a microchannel," *J. Stat. Mech. Theory Exp.*, vol. 2006, no. 1, p. P01012, 2006.

[66] L. Gherardini *et al.*, "A new immobilisation method to arrange particles in a gel matrix by ultrasound standing waves," *Ultrasound Med. Biol.*, vol. 31, no. 2, pp. 261–272, 2005.

[67] F. Gesellchen, A. L. Bernassau, T. Déjardin, D. R. S. Cumming, and M. O. Riehle, "Cell patterning with a heptagon acoustic tweezer – application in neurite guidance," *Lab Chip*, vol. 14, no. 13, pp. 2266–2275, 2014.

[68] P. Augustsson and J. Malm, "Acoustophoretic microfluidic chip for sequential elution of surface bound molecules from beads or cells," *Biomicrofluidics*, vol. 6, no. 3, pp. 34115–10, 2012.

[69] J. J. Hawkes, R. W. Barber, D. R. Emerson, and W. T. Coakley, "Continuous cell washing and mixing driven by an ultrasound standing wave within a microfluidic channel," *Lab Chip*, vol. 4, no. 5, pp. 446–452, 2004.

[70] Z. Yang, S. Matsumoto, H. Goto, M. Matsumoto, and R. Maeda, "Ultrasonic micromixer for microfluidic systems," *Sensors Actuators A Phys.*, vol. 93, no. 3, pp. 266–272, 2001.

[71] L. A. Kuznetsova, D. Bazou, G. O. Edwards, and W. T. Coakley, “Multiple three-dimensional mammalian cell aggregates formed away from solid substrata in ultrasound standing waves,” *Biotechnol. Prog.*, vol. 25, no. 3, pp. 834–841, 2009.

[72] A. F. H. Lum, M. A. Borden, P. A. Dayton, D. E. Kruse, S. I. Simon, and K. W. Ferrara, “Ultrasound radiation force enables targeted deposition of model drug carriers loaded on microbubbles,” *J. Control. Release*, vol. 111, no. 1, pp. 128–134, 2006.

[73] M. A. Sobanski *et al.*, “Ultrasound enhanced detection of individual meningococcal serogroups by latex immunoassay,” *J. Clin. Pathol.*, vol. 55, no. 1, pp. 37–40, 2002.

[74] X. Ding *et al.*, “Cell separation using tilted-angle standing surface acoustic waves,” *Proc. Natl. Acad. Sci.*, vol. 111, no. 36, pp. 12992–12997, 2014.

[75] Z. Wang and J. Zhe, “Recent advances in particle and droplet manipulation for lab-on-a-chip devices based on surface acoustic waves,” *Lab Chip*, vol. 11, no. 7, pp. 1280–1285, 2011.

[76] G. G. Fattinger, J. Kaitila, R. Aigner, and W. Nessler, “Thin film bulk acoustic wave devices for applications at 5.2 GHz,” *IEEE Symposium on Ultrasonics*, vol. 1. pp. 174–177, 2003.

[77] I. Leibacher, P. Reichert, and J. Dual, “Microfluidic droplet handling by bulk acoustic wave (BAW) acoustophoresis,” *Lab Chip*, vol. 15, no. 13, pp. 2896–2905, 2015.

[78] F. G. Mitri, “Acoustic radiation force on a rigid elliptical cylinder in plane (quasi)standing waves,” *J. Appl. Phys.*, vol. 118, no. 21, p. 214903, Dec. 2015.

[79] B. Raiton, J. R. McLaughlan, S. Harput, P. R. Smith, D. M. J. Cowell, and S. Freear, “The capture of flowing microbubbles with an ultrasonic tap using acoustic radiation force,” *Appl. Phys. Lett.*, vol. 101, no. 4, p. 44102, Jul. 2012.

[80] P. Glynne-Jones, C. E. M. Démoré, C. Ye, Y. Qiu, S. Cochran, and M. Hill, “Array-controlled ultrasonic manipulation of particles in planar acoustic resonator.,” *IEEE Trans. Ultrason. Ferroelectr. Freq. Control*, vol. 59, no. 6, pp. 1258–66, Jun. 2012.

[81] S. H. Cho, C. H. Chen, F. S. Tsai, J. M. Godin, and Y.-H. Lo, “Human mammalian cell sorting using a highly integrated micro-fabricated fluorescence-activated cell sorter (microFACS).,” *Lab Chip*, vol. 10, no. 12, pp. 1567–73, Jun. 2010.

[82] C. R. P. Courtney, C.-K. Ong, B. W. Drinkwater, A. L. Bernassau, P. D. Wilcox, and D. R. S. Cumming, “Manipulation of particles in two dimensions using phase controllable ultrasonic standing waves,” *Proc. R. Soc. A Math. Phys. Eng. Sci.*, vol. 468, no. 2138, pp. 337–360, Sep. 2011.

[83] X. Ding, J. Shi, S.-C. S. Lin, S. Yazdi, B. Kiraly, and T. J. Huang, “Tunable patterning of microparticles and cells using standing surface acoustic waves,” *Lab Chip*, vol. 12, no. 14, pp. 2491–2497, 2012.

[84] M. Evander *et al.*, “Noninvasive Acoustic Cell Trapping in a Microfluidic Perfusion

System for Online Bioassays," *Anal. Chem.*, vol. 79, no. 7, pp. 2984–2991, Apr. 2007.

[85] G. Goddard and G. Kaduchak, "Ultrasonic particle concentration in a line-driven cylindrical tube," *J. Acoust. Soc. Am.*, vol. 117, no. 6, pp. 3440–3447, 2017.

[86] G.-B. L. and C.-H. L. and S.-C. Chang, "Micromachine-based multi-channel flow cytometers for cell/particle counting and sorting," *J. Micromechanics Microengineering*, vol. 15, no. 3, p. 447, 2005.

[87] S. Peterson, G. Perkins, and C. Baker, "Development of an ultrasonic blood cell separator," in *Proceedings of the 8th Annual International Conference of the IEEE Engineering in Medicine and Biology Society*, 1986, pp. 154–156.

[88] P. W. S. Pui, F. Trampler, S. A. Sonderhoff, M. Groeschl, D. G. Kilburn, and J. M. Piret, "Batch and semicontinuous aggregation and sedimentation of hybridoma cells by acoustic resonance fields," *Biotechnol. Prog.*, vol. 11, no. 2, pp. 146–152, 1995.

[89] A. Nilsson, F. Petersson, H. Jonsson, and T. Laurell, "Acoustic control of suspended particles in micro fluidic chips," *Lab Chip*, vol. 4, no. 2, pp. 131–135, 2004.

[90] A. Lenshof, M. Evander, T. Laurell, and J. Nilsson, "Acoustofluidics 5: Building microfluidic acoustic resonators," *Lab Chip*, vol. 12, no. 4, pp. 684–695, 2012.

[91] C. Grenvall, P. Augustsson, J. R. Folkenberg, and T. Laurell, "Harmonic Microchip Acoustophoresis : A Route to Online Raw Milk Sample Precondition in Protein and Lipid Content Quality Control," *Anal. Chem.*, vol. 81, no. 15, pp. 6195–6200, 2009.

[92] F. Petersson, L. Åberg, A.-M. Swärd-Nilsson, and T. Laurell, "Free Flow Acoustophoresis: Microfluidic-Based Mode of Particle and Cell Separation," *Anal. Chem.*, vol. 79, no. 14, pp. 5117–5123, Jul. 2007.

[93] O. Jakobsson, C. Grenvall, M. Nordin, M. Evander, and T. Laurell, "Acoustic actuated fluorescence activated sorting of microparticles," *Lab Chip*, vol. 14, no. 11, pp. 1943–1950, 2014.

[94] A. A. Nawaz *et al.*, "Acoustofluidic Fluorescence Activated Cell Sorter," *Anal. Chem.*, vol. 87, no. 24, pp. 12051–12058, Dec. 2015.

[95] E. K. Sackmann, A. L. Fulton, and D. J. Beebe, "The present and future role of microfluidics in biomedical research," *Nature*, vol. 507, no. 7491, pp. 181–189, Mar. 2014.

[96] C. D. Chin *et al.*, "Microfluidics-based diagnostics of infectious diseases in the developing world," *Nat Med*, vol. 17, no. 8, pp. 1015–1019, Aug. 2011.

[97] A. A. Adams *et al.*, "Highly Efficient Circulating Tumor Cell Isolation from Whole Blood and Label-Free Enumeration Using Polymer-Based Microfluidics with an Integrated Conductivity Sensor," *J. Am. Chem. Soc.*, vol. 130, no. 27, pp. 8633–8641, Jul. 2008.

[98] D. C. Duffy, J. C. McDonald, O. J. A. Schueller, and G. M. Whitesides, “Rapid Prototyping of Microfluidic Systems in Poly(dimethylsiloxane),” *Anal. Chem.*, vol. 70, no. 23, pp. 4974–4984, Dec. 1998.

[99] J. Shi, X. Mao, D. Ahmed, A. Colletti, and T. J. Huang, “Focusing microparticles in a microfluidic channel with standing surface acoustic waves (SSAW),” *Lab Chip*, vol. 8, no. 2, pp. 221–3, Feb. 2008.

[100] L. Y. Yeo and J. R. Friend, “Ultrafast microfluidics using surface acoustic waves,” *Biomicrofluidics*, vol. 3, no. 1, p. 12002, Jan. 2009.

[101] L. Y. Yeo, H.-C. Chang, P. P. Y. Chan, and J. R. Friend, “Microfluidic Devices for Bioapplications,” *Small*, vol. 7, no. 1, pp. 12–48, 2011.

[102] B. Hammarstrom, M. Evander, H. Barbeau, M. Bruzelius, T. Laurell, and J. Nilsson, “Non-contact acoustic cell trapping in disposable glass capillaries,” *Lab Chip*, vol. 10, pp. 2251–2257, 2010.

[103] O. Manneberg, J. Svennebring, H. M. Hertz, and M. Wiklund, “Wedge transducer design for two-dimensional ultrasonic manipulation in a microfluidic chip,” *J. Micromechanics Microengineering*, vol. 18, p. 95025, 2008.

[104] M. Evander, A. Lenshof, T. Laurell, and J. Nilsson, “Acoustophoresis in Wet-Etched Glass Chips,” *Anal. Chem.*, vol. 80, no. 13, pp. 5178–5185, Jul. 2008.

[105] P. Glynne-Jones, R. J. Boltryk, and M. Hill, “Acoustofluidics 9: Modelling and applications of planar resonant devices for acoustic particle manipulation,” *Lab Chip*, vol. 12, no. 8, pp. 1417–26, Apr. 2012.

[106] M. B. Dentry, L. Y. Yeo, and J. R. Friend, “Frequency effects on the scale and behavior of acoustic streaming,” *Phys. Rev. E*, vol. 89, no. 1, p. 13203, Jan. 2014.

[107] L. Schmid, A. Wixforth, D. a. Weitz, and T. Franke, “Novel surface acoustic wave (SAW)-driven closed PDMS flow chamber,” *Microfluid. Nanofluidics*, vol. 12, no. 1–4, pp. 229–235, Aug. 2011.

[108] R. J. Shilton, M. Travagliati, F. Beltram, and M. Cecchini, “Nanoliter-Droplet Acoustic Streaming via Ultra High Frequency Surface Acoustic Waves,” *Adv. Mater.*, vol. 26, no. 29, pp. 4941–4946, 2014.

[109] S. Cular, D. W. Branch, V. R. Bhethanabotla, G. D. Meyer, and H. G. Craighead, “Removal of Nonspecifically Bound Proteins on Microarrays Using Surface Acoustic Waves,” *IEEE Sens. J.*, vol. 8, no. 3, pp. 314–320, 2008.

[110] C.-H. Tsai, H.-H. Hou, and L.-M. Fu, “An optimal three-dimensional focusing technique for micro-flow cytometers,” *Microfluid. Nanofluidics*, vol. 5, no. 6, pp. 827–836, 2008.

[111] R. Aoki, M. Yamada, M. Yasuda, and M. Seki, “In-channel focusing of flowing microparticles utilizing hydrodynamic filtration,” *Microfluid. Nanofluidics*, vol. 6, no. 4, p. 571, 2008.

[112] T. Stiles *et al.*, “Hydrodynamic focusing for vacuum-pumped microfluidics,” *Microfluid. Nanofluidics*, vol. 1, no. 3, pp. 280–283, 2005.

[113] R. Rodriguez-Trujillo, C. A. Mills, J. Samitier, and G. Gomila, “Low cost micro-Coulter counter with hydrodynamic focusing,” *Microfluid. Nanofluidics*, vol. 3, no. 2, pp. 171–176, 2007.

[114] D. Kohlheyer, J. C. T. Eijkel, A. van den Berg, and R. B. M. Schasfoort, “Miniaturizing free-flow electrophoresis – a critical review,” *Electrophoresis*, vol. 29, no. 5, pp. 977–993, 2008.

[115] P. B. Howell Jr, J. P. Golden, L. R. Hilliard, J. S. Erickson, D. R. Mott, and F. S. Ligler, “Two simple and rugged designs for creating microfluidic sheath flow,” *Lab Chip*, vol. 8, no. 7, pp. 1097–1103, 2008.

[116] J. P. Golden *et al.*, “Multi-wavelength microflow cytometer using groove-generated sheath flow,” *Lab Chip*, vol. 9, no. 13, pp. 1942–1950, 2009.

[117] K.-J. Kim *et al.*, “Antifungal activity and mode of action of silver nano-particles on Candida albicans,” *BioMetals*, vol. 22, no. 2, pp. 235–242, 2009.

[118] L.-M. Fu, C.-H. Tsai, and C.-H. Lin, “A high-discernment microflow cytometer with microweir structure,” *Electrophoresis*, vol. 29, no. 9, pp. 1874–1880, 2008.

[119] H.-H. Hou, C.-H. Tsai, L. Fu, and R. Yang, “Experimental and numerical investigation into micro-flow cytometer with 3-D hydrodynamic focusing effect and micro-weir structure,” *Electrophoresis*, vol. 30, pp. 2507–2515, 2009.

[120] R. Scott, P. Sethu, and C. K. Harnett, “Three-dimensional hydrodynamic focusing in a microfluidic Coulter counter,” *Rev. Sci. Instrum.*, vol. 79, no. 4, p. 46104, Apr. 2008.

[121] N. Watkins, B. M. Venkatesan, M. Toner, W. Rodriguez, and R. Bashir, “A robust electrical microcytometer with 3-dimensional hydrofocusing,” *Lab Chip*, vol. 9, no. 22, pp. 3177–3184, 2009.

[122] T. F. Didar and M. Tabrizian, “Adhesion based detection, sorting and enrichment of cells in microfluidic Lab-on-Chip devices,” *Lab Chip*, vol. 10, no. 22, pp. 3043–53, Nov. 2010.

[123] T. Franke, S. Braunmüller, L. Schmid, A. Wixforth, and D. a Weitz, “Surface acoustic wave actuated cell sorting (SAWACS),” *Lab Chip*, vol. 10, no. 6, pp. 789–794, 2010.

[124] J. C. Giddings, “A System Based on Split-Flow Lateral-Transport Thin (SPLITT) Separation Cells for Rapid and Continuous Particle Fractionation,” *Sep. Sci. Technol.*, vol. 20, no. 9–10, pp. 749–768, Nov. 1985.

[125] A. Lenshof, C. Magnusson, and T. Laurell, “Acoustofluidics 8: Applications of acoustophoresis in continuous flow microsystems,” *Lab Chip*, vol. 12, pp. 1210–1223, 2012.

[126] J. Shi, H. Huang, Z. Stratton, Y. Huang, and T. J. Huang, “Continuous particle separation in a microfluidic channel via standing surface acoustic waves (SSAW),” *Lab Chip*, vol. 9, no. 23, pp. 3354–3359, 2009.

[127] J. Nam, H. Lim, D. Kim, and S. Shin, “Separation of platelets from whole blood using standing surface acoustic waves in a microchannel,” *Lab Chip*, vol. 11, no. 19, pp. 3361–3364, 2011.

[128] S. Kapishnikov, V. Kantsler, and V. Steinberg, “Continuous particle size separation and size sorting using ultrasound in a microchannel,” *J. Stat. Mech. Theory Exp.*, vol. 2006, no. 1, p. P01012, Jan. 2006.

[129] F. K. Szabo and G. E. Hoffman, “High-frequency piezopolymer transducers with a copper-clad polyimide backing layer,” *IEEE Trans Ultrason Ferroelectr Freq Control.*, vol. 53, no. 7, pp. 1376–1380, 2006.

[130] Q. Zhou, S. Lau, D. Wu, and K. Kirk Shung, “Piezoelectric films for high frequency ultrasonic transducers in biomedical applications,” *Prog. Mater. Sci.*, vol. 56, no. 2, pp. 139–174, 2014.

[131] X. Geng and Q. M. Zhang, “Resonance modes and losses in 1-3 piezocomposites for ultrasonic transducer applications,” *J. Appl. Phys.*, vol. 85, no. 3, pp. 1342–1350, 1999.

[132] N. Sharifi Olyaei, M. M. Mohebi, and R. Kaveh, “Directional properties of ordered 3-3 piezocomposites fabricated by sacrificial template,” *J. Am. Ceram. Soc.*, vol. 100, no. 4, pp. 1432–1439, 2017.

[133] R. G. S. Rao and N. Kanagathara, “Lead Zirconate Titanate : A Piezo electric material,” *Chem. Pharm. Res.*, vol. 7, no. 5, pp. 921–923, 2015.

[134] D. Ballantine and S. Knovel, *Acoustic wave sensors : theory, design, and physico-chemical applications*. San Diego: Academic Press, 1997.

[135] E. E. Aktakka, R. L. Peterson, and K. Najafi, “High Stroke and High Deflection Bulk-PZT Diaphragm and Cantilever Micro Actuators and Effect of Pre-Stress on Device Performance,” vol. 23, no. 2, pp. 438–451, 2014.

[136] E. Aksel and J. L. Jones, “Advances in Lead-Free Piezoelectric Materials for Sensors and Actuators,” *Sensors*, vol. 10, pp. 1935–1954, 2010.

[137] H. Takahashi, H. Nagata, and T. Takenaka, “Mechanical bending strength of (Bi0.5Na0.5) TiO3-based lead-Free piezoelectric ceramics,” *Integr. Med. Res.*, pp. 0–4, 2017.

[138] N. A. Chrysochoidis and E. Gutiérrez, “Evaluation of the sensitivity and fatigue performance of embedded piezopolymer sensor systems in sandwich composite laminates,” *Smart Mater. Struct.*, vol. 24, no. 2, p. 25032, 2015.

[139] C. Li, P. Wu, S. Lee, A. Gorton, M. J. Schulz, and C. H. Ahn, “Flexible Dome and Bump Shape Piezoelectric Tactile Sensors Using PVDF-TrFE Copolymer,” vol. 17, no. 2, pp.

334–341, 2008.

[140] E. Sun and W. Cao, “Relaxor-based ferroelectric single crystals: Growth, domain engineering, characterization and applications,” *Prog. Mater. Sci.*, vol. 65, pp. 124–210, 2014.

[141] D. V. Tošic and M. F. Hribšek, “Modelling and wave velocity calculation of multilayer structure SAW sensors,” *Microelectron. Int.*, vol. 28, no. 2, pp. 3–7, 2011.

[142] L. Johansson, J. Enlund, S. Johansson, I. Katardjiev, M. Wiklund, and V. Yantchev, “Surface acoustic wave-induced precise particle manipulation in a trapezoidal glass microfluidic channel,” *J. Micromechanics Microengineering*, vol. 22, no. 2, p. 25018, 2012.

[143] H.-S. Yoon and G. Washington, “Piezoceramic actuated aperture antennae,” *Smart Mater. Struct.*, vol. 7, no. 4, p. 537, 1998.

[144] J. I. A. N. Z. Hang *et al.*, “Development of a multi-band photoacoustic tomography imaging system based on a capacitive micromachined ultrasonic transducer array,” vol. 56, no. 14, pp. 4012–4018, 2017.

[145] A. Tobias, “Acoustic-emission source location in two dimensions by an array of three sensors,” *Non-Destructive Test.*, vol. 9, no. 1, pp. 9–12, Feb. 1976.

[146] J. Li and J. L. Rose, “Implementing Guided Wave Mode Control by Use of a Phased Transducer Array,” vol. 48, no. 3, 2001.

[147] A. Synnevag, Johan-Fredrik Austeng and S. Holm, “Benefits of Minimum-Variance Beamforming in Medical Ultrasound Imaging,” *IEEE Trans. Ultrason. Ferroelectr. Freq. Control*, vol. 56, no. 9, pp. 1868–1879, 2009.

[148] C. D. Thomson, J. D. Palmer, R. N. Andersen, and K. B. Riding, “Ultrasonic testing phased array inspection fixture and related methods.” Google Patents, 2016.

[149] H. Gao, M. J. Guers, J. L. Rose, G. X. Zhao, and C. Kwan, “Ultrasonic guided wave annular array transducers for structural health monitoring.,” *AIP Conf. Proc.*, vol. 820, no. 1, pp. 1680–1686, 2006.

[150] P. G. Barthe and M. H. Slayton, “1.5-d ultrasound transducer array charlacterization,” pp. 895–897, 1996.

[151] I. O. Wygant *et al.*, “Integration of 2D CMUT Arrays with Front-End Electronics for Volumetric Ultrasound Imaging,” vol. 55, no. 2, 2008.

[152] J. D. N. Cheeke, *Fundamentals and Applications of Ultrasonic Waves, Second Edition*. Taylor & Francis, 2012.

[153] K. Yosioka and Y. Kawasima, “Acoustic radiation pressure on a compressible sphere,” *Acta Acust. united with Acust.*, vol. 5, no. 3, pp. 167–173, 1955.

[154] A. A. Doinikov, “Acoustic radiation pressure on a rigid sphere in a viscous fluid,” *Proc. R. Soc. A Math. Phys. Eng. Sci.*, vol. 447, pp. 447–466, Dec. 1994.

[155] F. G. Mitri, “Erratum to ‘Acoustic radiation force of high-order Bessel beam standing wave tweezers on a rigid sphere’ [Ultrasonics 49 (2009) 794–798],” *Ultrasonics*, vol. 54, no. 1, pp. 419–420, Jan. 2014.

[156] R. Barnkob, P. Augustsson, T. Laurell, and H. Bruus, “Measuring the local pressure amplitude in microchannel acoustophoresis,” *Lab Chip*, vol. 10, no. 5, pp. 563–570, 2010.

[157] A. Doinikov, “Acoustic radiation forces : classical theory and recent advances,” *Recent Res Devel Acoust.*, vol. 661, no. 2, pp. 39–67, 2003.

[158] M. Gröschl, “Ultrasonic Separation of Suspended Particles - Part I: Fundamentals,” *Acta Acust. united with Acust.*, vol. 84, no. 3, pp. 432–447, 1998.

[159] V. F. K. Bjerknes, *Die Kraftfelder*. Braunschweig: Vieweg und Sohn, 1909.

[160] M. A. H. Weiser, R. E. Apfel, and E. A. Neppiras, “Interparticle Forces on Red Cells in a Standing Wave Field,” *Acta Acust. united with Acust.*, vol. 56, no. 2, pp. 114–119, 1984.

[161] L. A. Crum, “Bjerknes forces on bubbles in a stationary sound field,” *J. Acoust. Soc. Am.*, vol. 57, no. 6, pp. 1363–1370, 1975.

[162] N. Riley, “Acoustic Streaming,” *Theor. Comput. Fluid Dyn.*, vol. 10, pp. 349–356, 1998.

[163] T.-D. Luong, V.-N. Phan, and N.-T. Nguyen, “High-throughput micromixers based on acoustic streaming induced by surface acoustic wave,” *Microfluid Nanofluid*, vol. 10, pp. 619–625, 2011.

[164] C. Devendran, I. Gralinski, and A. Neild, “Separation of particles using acoustic streaming and radiation forces in an open microfluidic channel,” *Microfluid. Nanofluidics*, vol. 17, no. 5, 2014.

[165] M. Wiklund, R. Green, and M. Ohlin, “Acoustofluidics 14: Applications of acoustic streaming in microfluidic devices,” *Lab Chip*, vol. 12, no. 14, pp. 2438–51, Jul. 2012.

[166] Lord Rayleigh, “On Waves Propagated along the Plane Surface of an Elastic Solid,” *Proc. London Math. Soc.*, vol. s1-17, no. 1, pp. 4–11, Nov. 1885.

[167] D. S. Ballantine and H. Wohltjen, “Surface acoustic wave devices for chemical analysis,” *Anal. Chem.*, vol. 61, no. 11, p. 704A–715A, 1989.

[168] M. Gedge and M. Hill, “Acoustofluidics 17: Theory and applications of surface acoustic wave devices for particle manipulation,” *Lab Chip*, vol. 12, no. 17, pp. 2998–3007, 2012.

[169] L. Verlet, “Computer ‘Experiments’ on Classical Fluids. I. Thermodynamical Properties

of Lennard-Jones Molecules," *Phys. Rev.*, vol. 159, no. 1, pp. 98–103, Jul. 1967.

[170] L. R. Dodd and G. L. Strobel, "Three-Body Effective Interaction in Deuterium," *Phys. Rev.*, vol. 165, no. 1, pp. 1–6, Jan. 1968.

[171] G. D. Skotis, D. R. S. Cumming, J. N. Roberts, M. O. Riehle, and A. L. Bernassau, "Dynamic acoustic field activated cell separation (DAFACS)," *Lab a Chip - Miniaturisation Chem. Biol.*, vol. 15, no. 3, pp. 802–810, 2015.

[172] A. J. Slobodnik, R. T. Delmonico, and E. D. Conway, *Microwave acoustics handbook*, vol. 2. Air Force Cambridge Research Laboratories, 1973.

[173] Y. Q. Fu *et al.*, "Recent developments on ZnO films for acoustic wave based bio-sensing and microfluidic applications : a review," *Sensors Actuators B Chem.*, vol. 143, pp. 606–619, 2010.

[174] S. Bhattacharya, A. Datta, J. M. Berg, and S. Gangopadhyay, "Studies on Surface Wettability of Poly (Dimethyl) Siloxane (PDMS) and Glass Under Oxygen-Plasma Treatment and Correlation With Bond Strength," *Jou*, vol. 14, no. 3, pp. 590–597, 2005.

[175] C. Con and B. Cui, "Effect of mold treatment by solvent on PDMS molding into nanoholes," *Nanoscale Res. Lett.*, vol. 8, no. 1, p. 394, 2013.

[176] H. Trichloro, "SIGMA-ALDRICH," pp. 1–8, 2015.

[177] H. Hillborg and U. W. Gedde, "Hydrophobicity recovery of polydimethylsiloxane after exposure to corona discharges," *Polymer (Guildf).*, vol. 39, no. 10, pp. 1991–1998, 1998.

[178] J. C. McDonald *et al.*, "Fabrication of microfluidic systems in poly(dimethylsiloxane)," *Electrophoresis*, vol. 21, no. 1, pp. 27–40, 2000.

[179] A. L. Bernassau, P. Glynne-Jones, F. Gesellchen, M. Riehle, M. Hill, and D. R. S. Cumming, "Controlling acoustic streaming in an ultrasonic heptagonal tweezers with application to cell manipulation," *Ultrasonics*, vol. 54, no. 1, pp. 268–74, Jan. 2014.

[180] J. Shi, D. Ahmed, X. Mao, S.-C. S. Lin, A. Lawit, and T. J. Huang, "Acoustic tweezers: patterning cells and microparticles using standing surface acoustic waves (SSAW).," *Lab Chip*, vol. 9, no. 20, pp. 2890–5, Oct. 2009.

[181] A. M. Baumann, V. Daanen, A. Leroy and J. Troccaz, "Computer Vision Approaches to Medical Image Analysis," vol. 4241, Reinhard R. Beichel and Milan Sonka, Ed. Springer, Berlin, 2006, p. 248.

[182] T. Kozuka, T. Tuziuti, H. Mitome, and T. Fukuda, "Acoustic manipulation of micro objects using an ultrasonic standing wave," *1994 5th Int. Symp. Micro Mach. Hum. Sci. Proc.*, p. 83.

[183] M. A. B. Andrade, G. D. Skotis, S. Ritchie, D. R. S. Cumming, M. O. Riehle, and A. L. Bernassau, "Contactless Acoustic Manipulation and Sorting of Particles by Dynamic Acoustic Fields," *IEEE Trans. Ultrason. Ferroelectr. Freq. Control*, vol. 63, no. 10, pp.

1593–1600, 2016.

[184] R. Gilabert and P. McNaughton, “Enrichment of the fraction of nociceptive neurones in cultures of primary sensory neurones,” *J. Neurosci. Methods*, vol. 71, pp. 191–198, 1997.

[185] M. Chyczewski *et al.*, “Sources of porcine longissimus dorsi muscle (LDM) innervation as revealed by retrograde neuronal tract-tracing,” vol. 44, no. 3, pp. 189–194, 2006.

[186] R. Vargas-Pinto, H. Gong, A. Vahabikashi, and M. Johnson, “The effect of the endothelial cell cortex on atomic force microscopy measurements,” *Biophys. J.*, vol. 105, no. 2, pp. 300–309, 2013.

[187] R. Guldiken, M. C. Jo, N. D. Gallant, U. Demirci, and J. Zhe, “Sheathless size-based acoustic particle separation,” *Sensors*, vol. 12, no. 1, pp. 905–922, Jan. 2012.

[188] N. D. Mehendale, “Hydrodynamic Flow Focusing for Microfluidic Cell Sorting Chip,” *2014 COMSOL Conf. Bangalore*, 2014.

[189] X. Ding *et al.*, “Surface acoustic wave microfluidics,” *Lab Chip*, vol. 13, no. 18, pp. 3626–3649, 2013.

[190] D. Wu, Y. Luo, X. Zhou, Z. Dai, and B. Lin, “Multilayer poly(vinyl alcohol)-adsorbed coating on poly(dimethylsiloxane) microfluidic chips for biopolymer separation,” *Electrophoresis*, vol. 26, no. 1, pp. 211–218, 2005.